Lehrstuhl für Technische Elektrophysik

Compact Modeling of Microsystems

Peter Voigt

Vollständiger Abdruck der von der Fakultät für Elektrotechnik und Informationstechnik der Technischen Universität München zur Erlangung des akademischen Grades eines

Doktors-Ingenieur (Dr.-Ing.)

genehmigten Dissertation.

Vorsitzende: Univ.-Prof. Dr. rer. nat. D. Schmitt-Landsiedel

Prüfer der Dissertation:

1. Univ.-Prof. Dr. rer. nat. G. Wachutka
2. Univ.-Prof. Dr.-Ing. habil. G. Gerlach, Technische Universität Dresden

Die Dissertation wurde am 05.06.2001 bei der Technischen Universität München eingereicht und durch die Fakultät für Elektrotechnik und Informationstechnik am 22.03.2002 angenommen.

Abstract

Guided by the methods of Thermodynamics, a system description by means of Generalized Kirchhoffian Networks can be found. For this purpose, a generic form of the required compact models is derived, which is consistent with the conservation laws in such networks.

Typical examples demonstrate the usefulness of this generic model form for microsystem modeling. For the presented analytical and physically based models, an adequate and efficient parameter extraction method is presented. Some typical microsystems serve as demonstrators to discuss the advantages and drawbacks of various methods for compact modeling. Guidelines for a suitable selection of modeling approaches are presented.

Kurzzusammenfassung

Ausgehend von den Prinzipien der Thermodynamik, wird mit den Methoden einer Systembeschreibung durch Generalisierte Kirchhoffsche Netze eine dazu konsistente generische Form für Kompaktmodelle abgeleitet. An typischen Beispielen wird die Eignung dieser generischen Formulierung für Anwendungen in der Mikrosystemtechnik demonstriert. Für derart entwickelte analytische, physikalisch basierte Modelle wurde eine effiziente Parameterextraktionsmethode dargestellt. Anhand einer Reihe von Beispielen aus verschiedenen Bereichen der Mikrosystemtechnik werden Vor- und Nachteile verschiedener Methoden der Kompaktmodellierung verglichen und Richtlinien für deren geeignete Auswahl je nach Anwendung herausgearbeitet.

Contents

1. Introduction

A simulation approach for microsystems should fulfill three requests: First, it should allow a detailed analysis of all system components, namely the transducing elements and the electronic circuitry. Second, it must allow the analysis of system blocks, up to a simulation of the entire system, requiring high numerical efficiency, especially if a transducer or actuator is embedded in a large system or if a huge amount of transducers or actuators is contained in the system under consideration [1].

Third, it should be consistent with the CAD-environment used in the design of integrated circuits.

To this end, a hierarchical approach has to be pursued [2, 3]. This hierarchy can be derived by distinguishing three levels of discretization of a problem, which in reality is continuous.

First level of abstraction: The discretization is quasi-continuous in time, space and physical variables. This is called the level of physical modeling and allows for a detailed analysis of small parts of a system. An example is the Finite Element Analysis.

Second level of abstraction: The discretization is quasi-continuous in time and physical variables, but discrete in space. Here the system is partitioned into blocks (devices), which are modeled by a uniform "generic" mathematical description in terms of conjugate thermodynamic state variables and the pertinent currents ("fluxes", "through quantities") and driving forces ("affinities", "across quantities") such as, e.g., mass flow and pressure gradient or electrical current and voltage drop. The internal behavior of each of the individual system components is described by a specific "tailored" version of the generic model. The full microsystem is assembled by linking the individual sub-models of the constituent parts through flux-conserving interface conditions for the respective pairs of conjugate state variables in adjacent components. The resulting "Kirchhoffian Network" model is governed by generalized mesh rules and node rules for each pair of conjugate state variables and, thus, constitutes a natural approach for analog system simulation, because the coupling between the different energy domains is governed by basic conservation laws for energy, particle numbers, mass, charge, etc. An example is the analog SPICE simulation in the electrical domain.

Third level of abstraction: The discretization is discrete in time, space and physical variables. This leads to the level of digital system simulation. An example is VHDL-modeling.

At the level of physical modeling many software tools are available which address subproblems related to a specific physical domain (thermal, mechanical, etc.). A number of direct coupling schemes between different energy and signal domains have been realized (e.g. thermo-mechanical analysis), but more often the only available solution is the (not

necessarily consistent) use of a simulator-simulator coupling. The drawbacks of this approach are the high numerical effort and instabilities, which may in particular occur in the case of strong coupling between the subsystems. Generally this approach is limited to relatively small parts of a system, typically to a single device such as, e.g. a micro valve [4].

At the level of analog network simulation and digital system simulation, compact models for all devices involved in the system function need to be developed, starting from a detailed analysis by means of physical modeling. Following the approach of tailored modeling [5] leads to a consistent description of the system in terms of a Generalized Kirchhoffian Network. VHDL-AMS [6] is a generic software representation of this modeling approach, constituting the coupling between analog and digital system simulation, and providing the required integration into the CAD environment of integrated circuit design.

Compact models have been successfully used for many years, especially in the design of electronic systems and integrated circuits. A powerful suite of methods and their corresponding software-tools has been developed for that purpose, with analog network simulation based on Kirchhoffian networks being an essential part of it. Hence, it makes a lot of sense to utilize this profound knowledge base and even this software pool for microsystem modeling. This is additionally motivated by the fact, that microsystem technology has many of its roots in silicon-based electronic technology and that a close integration of transducers and actuators with advanced control electronics is in the focus of microsystem development.

The aim of this work is to derive some guidelines for the development of compact models of microsystems in such a way, that the design methodology and design software tools from microelectronics can be made available for the growing field of microsystem technology.

In chapter 2 of this work, some basics from thermodynamics will be recalled, which are of importance for the development of physically based compact models. Starting from this point, it will be shown how the method of Kirchhoffian network models, which is well established for electronic circuits, can be generalized to other physical domains. Some guidelines for the development of compact models and a generic structure of a compact model will be derived.

In chapter 3, three different methods for compact modeling are presented. These methods are illustrated by examples which highlight advantages and disadvantages of each approach. A special focus lies on analytical, physically based models and their capabilities for design studies and statistical modeling. Some conclusions for the proper selection of a modeling approach in a given request situation will be drawn.

In chapter 4, a parameter extraction method for analytical, physically based compact models is presented, which takes into account, that most model parameters have a distinct physical meaning and that the resulting model parameter sets could contribute to a database for statistical modeling, yield/failure analysis or statistical process control.

In chapter 5, examples illustrate the power of compact modeling being applied to complex microsystems. Example 1 shows how the interaction of an electro-mechanical device with an electronic control circuit can be modeled in case of a strong non-linear, bi-directional

coupling between both. Examples 2 to 4 show, how complex devices with non-linear and discontinuous behavior (incl. hysteresis effects) can be successfully described by analytical, physically based compact models. These models will be compiled to the macromodel of a micropump, allowing to analyze the pump operation. It will be illustrated that these compact models can be used to perform design studies not only on device- but also on system-level. Example 5 shows the capability of physically based compact models to supply process control tasks by investigating the impact of process tolerances on the system performance.

2. Generalized Kirchhoffian Networks

2.1 Introduction

The description of electrical circuits as Kirchhoffian networks and their subsequent simulation in an analog network simulator has proven to be very successful. It was one prerequisite for the development of large integrated circuits. Especially for circuits built by discrete components the Kirchhoffian network model is quite intuitive: the interconnects between devices have negligibly small resistances and, therefore, can be characterized by a single potential value, usually measured as voltage with reference to the ground potential. The conservative nature of the electrical potential directly leads to the Kirchhoffian mesh rule for voltages. Charge conservation, on the other hand, yields the node rule for the currents through the interconnects. The connecting wires of the devices appear as terminal nodes in the model, and determine an intuitive partition of the full system in lumped element device models or compact models. The device model equations relate the node potentials to the electrical currents through the device between neighboring terminal nodes. Thus, each terminal node gets two variables assigned to it: the node potential and a current flowing through it.

Although this kind of modeling traditionally focuses on the electrical domain, it has successively been extended to include also other physical domains. Due to the strong dependence of device properties on temperature, the temperature was included into the device models as a parameter. But important effects such as self-heating of devices and thermal coupling between neighboring devices could not be modeled with this approach, though. So the next step was to include temperature as an internal variable in the device model equations. In this way, the self-heating of a device could be modeled, balancing the internal heat generation rate to the heat flow towards a heat sink and to the thermal capacity of the device. However, this approach is limited to simple structures, where the thermal problem can be described in terms of a lumped thermal resistivity and capacity. A systematic, general approach to the self-consistent inclusion of thermal and other non-electric effects in analog electrical network simulation is hence required.

The analog network simulation based on Kirchhoffian network models turned out to be so powerful that many successful attempts have been made to adopt it to others than electrical problems, mostly by describing non-electrical elements by an electrical analogue. Typical cases are the description of mechanical or hydraulic problems by analog RLC electrical networks. A major draw-back of this approach is the limitation to linear effects. To include nonlinear device behavior requires to setting up new device models. This next necessary step was done by introducing behavioral models and making their simulation possible in the analog network simulation tools.

The aim of this chapter is to investigate the problem how to systematically adopt Kirch-

hoffian network-based modeling to other, non-electrical problems. Moreover, we will try to establish certain guidelines for the development of the required CMs.

2.2 Thermodynamic models

Irreversible thermodynamics provides the proper framework for a unified phenomenological description of physical effects and processes in systems. Therefore it is best suited to model microsystems, which typically contain transducing devices together with electronic elements and, therefore, by their very nature involve various couplings between multiple physical disciplines. Thermodynamic methods have been successfully applied to describe transport processes in semiconductors [7] and transducing effects in microsystems [8, 5, 9, 10, 11].

In this section, some fundamentals of thermodynamics are recalled from [12, 13], as they constitute the basis for microsystem modeling.

2.2.1 Thermodynamic equilibrium

Local thermodynamic equilibrium states are governed by a potential function, which depends on the extensive state variables only and satisfies the maximum entropy principle. This potential function may be chosen as the internal energy U contained in a control volume V

$$U(\vec{r},t) = U(E_1(\vec{r},t), ..., E_k(\vec{r},t), V(\vec{r},t), S(\vec{r},t)) \tag{2.1}$$

where S denotes the entropy and $E_1, \cdots, E_k$ a set of further extensive state variables.

The total differential of the internal energy U is assumed to exist and is called *Gibbs relation*:

$$\mathrm{d}U = \sum_{i=1}^{k} I_i \mathrm{d}E_i - p\mathrm{d}V + T\mathrm{d}S \tag{2.2}$$

$$I_i \overset{def}{=} \frac{\partial U}{\partial E_i} \tag{2.3}$$

$$p \overset{def}{=} -\frac{\partial U}{\partial V} \tag{2.4}$$

$$T \overset{def}{=} \frac{\partial U}{\partial S} \tag{2.5}$$

The quantities I_i, p and T are called intensive state variables and are evidently, by their definition, functions of all extensive state variables. The intensive variables (I_i, p and T) and the corresponding extensive variables (E_i, V and S) occuring in the partial differential form (2.2) constitute pairs of conjugate variables. $U(\vec{r},t)$ acts as a thermodynamic potential, but by means of Legendre transformations other potentials can be found, which may be more appropriate to describing a given problem.

Only $N = k + 2$ of the set of intensive and extensive state variables are independent variables. With a view to a more compact notation, V, S, p and T are written as

E_{N-1}, E_N, I_{N-1} and I_N, respectively. If all intensive variables I_i are assumed to depend on all extensive variables E_i, it follows that the following matrix expresses the relations between intensive and extensive variables:

$$\begin{pmatrix} I_1 \\ \vdots \\ I_N \end{pmatrix} = \begin{pmatrix} \alpha_{11} & \cdots & \alpha_{1N} \\ & \ddots & \\ \alpha_{N1} & \cdots & \alpha_{NN} \end{pmatrix} \cdot \begin{pmatrix} E_1 \\ \vdots \\ E_N \end{pmatrix} \tag{2.6}$$

$$\alpha_{ij} \stackrel{def}{=} \frac{\partial I_i}{\partial E_j} \tag{2.7}$$

The matrix (2.6) is symmetric and expresses basic equilibrium transducer effects. Any partial or complete inversion of this matrix describes additional transducer effects, because other constraints apply, i.e. another set of independent variables is selected. It is important to note that the coefficients α_{ij} are still functions of the independent variables.

The first law of thermodynamics states that the total energy of a closed system is conserved. In the following formulation it expresses that the internal energy of a system can be increased by adding either unordered energy (heat) $\mathrm{d}Q$ or ordered energy (=physical work):

$$\mathrm{d}U = \mathrm{d}Q + \sum_{i=1}^{k} I_i \mathrm{d}E_i - p\mathrm{d}V \tag{2.8}$$

A comparison with the Gibbs relation (2.2) reveals that the heat may be represented as $\mathrm{d}Q = T\mathrm{d}S$.

2.2.2 Non-equilibrium effects

a) Affinities and fluxes

Thermodynamic non-equilibrium processes can be described by fluxes of extensive quantities, which are driven by affinities. The flux vector $\vec{J}_i$ can be intoduced as the amount of an extensive quantity E_i which passes an infinitesimal control area per unit time, while the associated affinitiy $\vec{f}_i$ is the spatial gradient of the conjugate intensive state variable E_i. The fluxes are assumed to be functionals of all affinities and of all intensive state variables. A simplifying assumption is that the fluxes depend on the instantaneous values of the $\vec{f}_i$ and I_i only:

$$\vec{J}_i = J(f_1, ..., f_N, I_1, ..., I_N) \tag{2.9}$$

$$\vec{f}_i \stackrel{def}{=} \mathrm{grad} I_i \tag{2.10}$$

$$\vec{J}_i \cdot \mathrm{d}\vec{a} \cdot \mathrm{d}t \stackrel{def}{=} \mathrm{d}E_i \tag{2.11}$$

Expanding (2.9) in a Taylor series with respect to the $\vec{f}_i$, the constant terms vanish because all fluxes are zero in the absence of any affinity. A next simplification is to neglect all second and higher order terms in the Taylor expansion, thus assuming that the fluxes depend only linearly on the affinities. This yields the following matrix relation between

fluxes and driving affinities:

$$\begin{pmatrix} \vec{J}_1 \\ \vdots \\ \vec{J}_N \end{pmatrix} = \begin{pmatrix} \mathbf{L}_{11} & \cdots & \mathbf{L}_{1N} \\ & \ddots & \\ \mathbf{L}_{N1} & \cdots & \mathbf{L}_{NN} \end{pmatrix} \cdot \begin{pmatrix} \vec{f}_1 \\ \vdots \\ \vec{f}_N \end{pmatrix} \tag{2.12}$$

$$\mathbf{L}_{ij} \stackrel{def}{=} \frac{\partial \vec{J}_j}{\partial \vec{f}_i} \tag{2.13}$$

The matrix elements $\mathbf{L}_{ij}$ are known as the kinetic coefficients or Onsager's phenomenological coefficients and depend evidently on all intensive parameters I_i. The $\mathbf{L}_{ii}$ are called the primary or principal coefficients, because they relate a flux to its conjugate affinity. The non-diagonal $\mathbf{L}_{ij}$ (for $i \neq j$) are the coupling coefficients. Some statements can be made about the coefficients $\mathbf{L}_{ij}$ of the super matrix (2.12):

$$\mathbf{L}_{ij} \geq 0 \tag{2.14}$$

$$\mathbf{L}_{ii}\mathbf{L}_{jj} - \mathbf{L}_{ij}\mathbf{L}_{ji} \geq 0 \tag{2.15}$$

$$\mathbf{L}_{ij} = \mathbf{L}_{ji}^T \tag{2.16}$$

Relations (2.14) and (2.15) follow from the second law of Thermodynamics, which states that the entropy production rate σ cannot be negative in an isolated system

$$\sigma = \sum_{i=1}^{N} \vec{J}_i \cdot \vec{f}_i \geq 0 \,, \tag{2.17}$$

which means that the matrix $\mathbf{L}$ in (2.12)is positive definite. The relations (2.16) are called the Onsager symmetry relations and hold true if the state variables are even functions of the velocity of the atomistic elements constituting the considered thermodynamic system. In case of the presence of a magnetic field $\vec{B}$, some state variables can be odd functions of the particle velocities, and (2.15) changes to

$$\mathbf{L}_{ij}(\vec{B}) = \mathbf{L}_{ji}^T(-\vec{B}) \tag{2.18}$$

The coefficients $\mathbf{L}_{ij}$ cannot be determined by means of the thermodynamic theory, but additional physical laws governing the respective physical energy domain must be invoked.

Another important assumption in the theory of irreversible thermodynamics is that the Gibbs relation, given by equation (2.2), still holds true in non-equilibrium situations, if these are not too far from (local) thermodynamic equilibrium.

b) Stationary processes

In many practical situations a system is in a stationary state. This means that all thermodynamic state variables are constant in time, though not necessarily at their equilibrium values.

If in a system with N independent state variables a number of $k < N$ affinities is externally forced to constant values $\vec{f}_i = \text{const.} \neq 0$, then the system is in a stationary state, if

the entropy production has a minimum. In that case, all fluxes which are not conjugate to any of the forced affinities must vanish. The entropy production rate is then given by

$$\sigma = \sum_{i=1}^{k} \vec{J}_i \cdot \vec{f}_i \ . \tag{2.19}$$

If we now assume that one of the not forced affinities experiences a perturbation $\delta\vec{f}_m$ from its stationary value, then this causes a flux

$$\vec{J}_m = \mathbf{L}_{mm}\delta\vec{f}_m \ . \tag{2.20}$$

Because the Onsager matrix $\mathbf{L}$ is positive definite, it can be shown that

$$\vec{J}_m \cdot \delta\vec{f}_m > 0 \tag{2.21}$$

and

$$\delta\sigma = \delta\vec{f}_m{}^T \mathbf{L}_{mm}\delta\vec{f}_m > 0 \tag{2.22}$$

This implies that any perturbation causes a flux which is directed in such a way that the perturbing excitation is reduced and the system moves towards its stationary state again. In the special case that no external affinities are forced, i.e. $k = 0$, the system returns from an excited state back into its thermodynamic equilibrium state, while the entropy production approaches zero.

c) Relaxation phenomena

So far we considered situations where the entire system can be described by assuming *local* thermodynamic equilibrium. Now this needs not to be the case, but it is assumed that the system can be divided into two subsystems, each of them being in local thermodynamic equilibrium, and both filling the same volume. A mixture of different species of particles such as electrons and ions in a plasma could serve as an example.

Both systems can be described by their respective temperatures T' and T'' and separately fulfill their Gibbs relations

$$T'\mathrm{d}S' = \mathrm{d}U' - p'\mathrm{d}V' + \sum_{i=1}^{n} I_i'\mathrm{d}E_i' \tag{2.23}$$

$$T''\mathrm{d}S'' = \mathrm{d}U'' - p''\mathrm{d}V'' + \sum_{i=1}^{n} I_i''\mathrm{d}E_i'' \ . \tag{2.24}$$

The total change in entropy is

$$\mathrm{d}S = \mathrm{d}S' + \mathrm{d}S'' \ . \tag{2.25}$$

Assuming that the total energy is conserved (adiabatic process: $0 = \mathrm{d}U' + \mathrm{d}U''$), no volume changes of the subsystems occur, and none of the other extensive parameters E_i', E_i'' change (i.e. no recombination between electrons and ions takes place in the above-mentioned example of a plasma), then follows

$$\mathrm{d}S = \mathrm{d}U'(1/T' - 1/T'') \ . \tag{2.26}$$

The entropy production rate is then

$$\sigma = \frac{\mathrm{d}S}{\mathrm{d}t} = \frac{\mathrm{d}U'}{\mathrm{d}t} \cdot \frac{T'' - T'}{T'\,T''} \; . \tag{2.27}$$

This has the form of *entropy production rate = flux · affinity*, with the flux variable being the temporal change of an extensive state variable. Therefore, a phenomenological relation between flux and affinity can be introduced:

$$\frac{\mathrm{d}U'}{\mathrm{d}t} = L \cdot \frac{T'' - T'}{T'\,T''} \; . \tag{2.28}$$

From the phenomenological state equation

$$\mathrm{d}U' = C' \cdot \mathrm{d}T' \tag{2.29}$$

with C' being the specific heat capacitance, one gets

$$\frac{\mathrm{d}T'}{\mathrm{d}t} = \frac{L}{C'\,T'\,T''}(T'' - T') \; . \tag{2.30}$$

If the temperature T denotes the equilibrium temperature which both systems would attain after they have relaxed, then, with $\Delta T' = T' - T$ and $\Delta T'' = T'' - T$, equation (2.30) can be rewritten as

$$\frac{\mathrm{d}\Delta T'}{\mathrm{d}t} = \frac{L}{C'\,T'\,T''}(\Delta T'' - \Delta T') \; . \tag{2.31}$$

In the case that the heat capacitance of one subsystem (the ions, e.g.) is much larger than the other, means $C'' \gg C'$, then it follows that $\Delta T' \gg \Delta T''$, and therefore we arrive at the familiar equation for a relaxation process:

$$\frac{\mathrm{d}\Delta T'}{\mathrm{d}t} = \frac{1}{\tau} \cdot \Delta T' \tag{2.32}$$

$$\tau \overset{def}{=} -C' \cdot T^2/L \; . \tag{2.33}$$

This equation shows that the rate of change of a quantity is proportional to its deviation from the equilibrium, which is in correspondence to equation (2.22).

The relations recalled in this chapter will be used to describe the thermodynamic basis for the frequently used generalization of the Kirchhoffian network rules to other physical domains besides the electrical one. Additionally they guide the deviation of a generic form of a compact model, which is consistent with generalized Kirchhoffian network modeling.

2.3 Compact models

Assuming that a continuous field model (CFM) has been successfully developed for a microsystem and can be described by means of irreversible thermodynamics, now the task can be performed to derive compact models (CMs). A first important step is the division of the microsystem into smaller subsystems, called devices, such that each device can be modeled by a relatively simple compact model. Sometimes this is fairly simple, because the microsystem consists of functional units, which are well separated from each other. More often such a natural separation cannot easily be found. If the devices are chosen too large, then the effects inside might be too complex and it is difficult to model them. If the devices are too small, it might not be possible to separate effects in neighboring devices properly. The following considerations try to give some guidlines how to find an appropriate partition of a system into devices.

2.3.1 Kirchhoffian network rules

If a system is separated into two subsystems, the interaction between each other is effected by the distributed flow of n thermodynamic quantities across their common interface Γ. This flow is driven by the corresponding affinities:

$$\vec{J}_i^{\,\Gamma} = \sum_{j=1}^{n} \mathbf{L}_{ij}^{\Gamma} \cdot \vec{f}_j^{\,\Gamma} \; . \tag{2.34}$$

Not necessarily all N existing thermodynamic quantities, but only $n \leq N$ quantities are exchanged across Γ. A container with metallic walls may serve as an example: only heat and electric charge can be exchanged with adjacent other systems, but no gas or liquid can flow. However, in the volume of the devices, still all N thermodynamic quantities must be considered.

Now, an essential assumption will be made about the interface: the spatial distribution of $\vec{f}_i$ and $\vec{J}_i$ along the interface Γ is not decisive for describing the device behavior. Therefore, the interaction of neighboring devices across their common interface Γ can be characterized by one simple, "lumped" variable for each thermodynamic quantity. Thus, the following lumped variables can be introduced:

$$\vec{J}_i^{\,\Gamma} \quad \rightarrow \quad \mathcal{W}_i \tag{2.35}$$

$$\mathrm{grad} I_i = \vec{f}_i^{\,\Gamma} \quad \rightarrow \quad \mathcal{E}_i \; . \tag{2.36}$$

This is illustrated in Fig. 2.1 below.

The interaction across the interface Γ is therefore described by n pairs of lumped, conjugate variables $\mathcal{W}_i$ and $\mathcal{E}_i$, which have their correspondence in the distributed field variables of thermodynamic conjugate fluxes and affinities. The interface between adjacent devices is called node.

Because extensive thermodynamic quantities satisfy balance or conservation laws, the corresponding lumped variables $\mathcal{W}_i$ must also obey these laws when expressed in integral

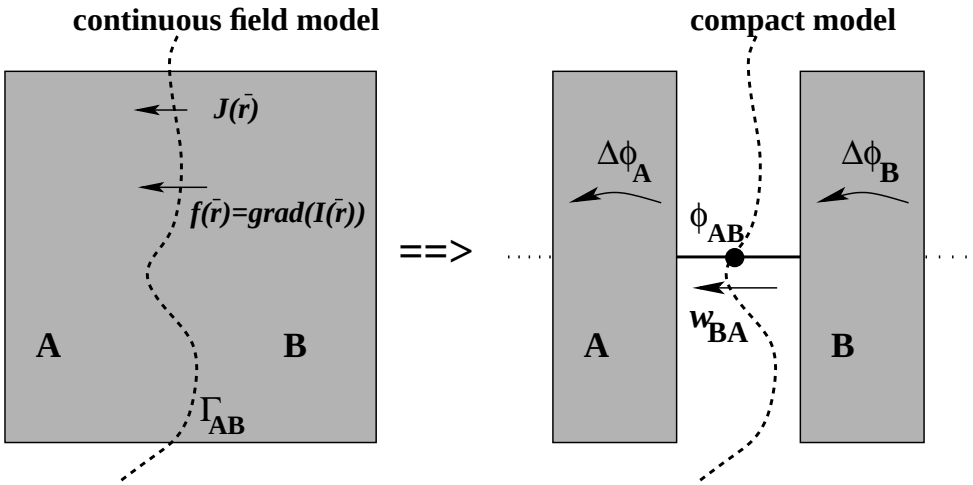

Fig. 2.1: Schematic view of a system, separated into two devices by an interface, and the schematic representation of the corresponding compact or lumped element model.

formulation. They can therefore be found to be

$$\mathcal{W}_i = \int_\Gamma \vec{J}_i^{\,\Gamma} \cdot \mathrm{d}\vec{A} \,. \tag{2.37}$$

The affinity $\vec{f}_i^{\,\Gamma} = \mathrm{grad} I_i$ depends not only on the value of the intensive thermodynamic variable I_i along the interface Γ, but also on its spatial distribution in the vanity of the interface. The description of the interface using affinities $\vec{f}_i^{\,\Gamma}$ leaves the intensive state variables I_i^Γ undetermined within an additive constant. Therefore, the interface Γ is better described as approximate iso-surface of an intensive variable I_i rather than by its affinity $\vec{f}_i = \mathrm{grad} I_i$. Hence we introduce lumped interface variables ϕ_i. The ϕ_i are representing the state of the interface and are derived from the I_i^Γ according to

$$f(\phi_i) = \frac{\int_\Gamma f(I_i^\Gamma)\,\mathrm{d}A}{\int_\Gamma \mathrm{d}A} \,, \tag{2.38}$$

whith the function f chosen in such a way that important system properties are correctly reproduced by the resulting model. An example will be shown in section 2.3.4.

Now two important consequences follow immediately:

i): Because the $\mathcal{W}_i$ still fulfill the balance law for thermodynamic extensive quantities $\mathrm{div}\,\vec{J}_i = \dot{E}_i - \pi_i$ (with π_i being the production rate of quantity E_i per infinitesimal control volume $\mathrm{d}V$), the currents at a node sum up to zero, and the sum of all currents entering a device equals the negative production rate $\Pi_i = \int_V \pi_i \mathrm{d}V$ of this quantity inside this device, as illustrated in Fig. 2.2.

$$\sum_{k=1}^{K} \mathcal{W}_i^k = \int_V (\dot{E}_i - \pi_i)\,\mathrm{d}V \; = \dot{Q}_i - \Pi_i \,. \tag{2.39}$$

ii): From $\mathrm{rot}\,\mathrm{grad} I_i = 0$, it follows that $\oint \mathrm{grad} I_i \,\mathrm{d}\mathbf{r} = 0$. Therefore, for an arbitrary

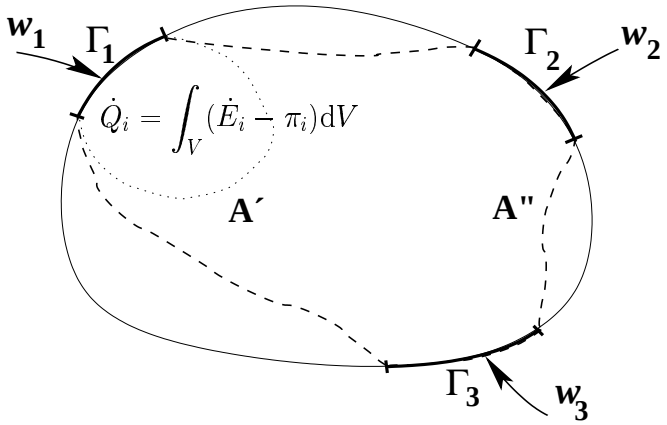

Fig. 2.2: Schematic view of a system with three interfaces. The conservation of the flux must hold true for any integration surface A' or A'', thus making the node rule for currents obvious.

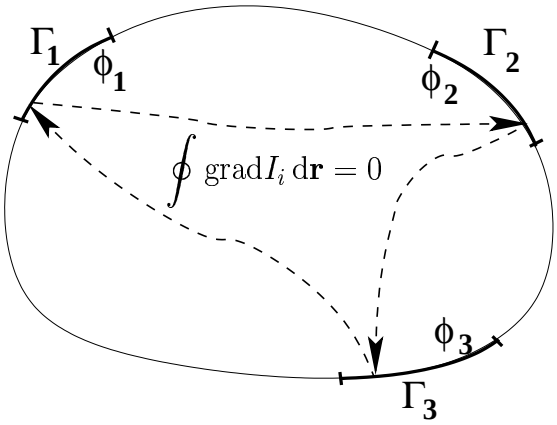

Fig. 2.3: Schematic view of a system with three interfaces. Any integration of an affinity along an arbitrary, but closed path must vanish, thus making the mesh rule for potentials obvious.

number K of interfaces connected in series by a sequence of adjacent devices, it follows

$$\sum_{k=1}^{K-1} (\phi_i^{k+1} - \phi_i^k) = \phi_i^K - \phi_i^1 \; . \tag{2.40}$$

This is sketched in Fig. 2.3 .

In the electrical domain, these are the Kirchhoffian network rules for voltage and current [14]; but now we have generalized this concept to any pair of conjugate intensive and extensive lumped node variables. This reveals, why the application of analog electrical network simulation, which is based on a Kirchhoffian network description, could be so successfully applied to other physical disciplines. In Fig. 2.4 it is sketched how different devices are switched together, thus forming a system macro-model, based on a Kirchhoffian network description.

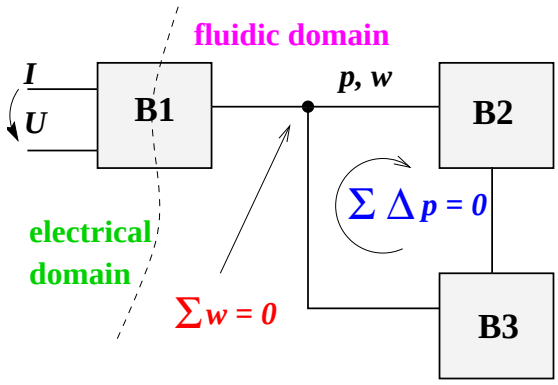

Fig. 2.4: Schematic view of a Kirchhoffian network, coupling different physical domains. The conservation laws for mass flow w and hydrostatic pressure p are reflected in sum rules on the nodes and along closed mesh loops.

2.3.2 Generic model

Now the question arises, how the currents $\mathcal{W}_i$ are related to the nodal potentials ϕ_i. Because the Onsager matrix is positive definite and symmetric, it can be inverted and equation (2.12) can be written as

$$\vec{f}_i = \sum_{j=1}^{N} \mathbf{R}_{ij} \cdot \vec{J}_j \tag{2.41}$$

$$\mathbf{R} = \mathbf{L}^{-1} . \tag{2.42}$$

Integrating this equation along an arbitrary path across the device from one interface Γ_1 to another interface Γ_2 gives

$$\int_{\Gamma_1}^{\Gamma_2} \vec{f}_i \, \mathrm{d}\mathbf{r} = \int_{\Gamma_1}^{\Gamma_2} \sum_{j=1}^{N} (\mathbf{R}_{ij} \cdot \vec{J}_j) \, \mathrm{d}\mathbf{r} . \tag{2.43}$$

Now let us assume that all interface currents of the device are kept to zero apart from those at the interfaces Γ_1 and Γ_2, where the potentials are set to ϕ_i^1 and ϕ_i^2, respectively. By changing the order of summation and integration one gets

$$\phi_i^2 - \phi_i^1 = \sum_{j=1}^{N} \int_{\Gamma_1}^{\Gamma_2} \mathbf{R}_{ij} \cdot \vec{J}_j \, \mathrm{d}\mathbf{r} . \tag{2.44}$$

Assuming now, that an additional physical analysis besides thermodynamic considerations (i.e., solving the transport equations $\vec{J}_i = \sum_{j=1}^{n} \mathbf{L}_{ij} \cdot \vec{f}_j$ in the interior of the device for the given boundary conditions) results in expressions for the matrix coefficients $\mathbf{R}_{ij}$ in terms of the nodal potentials ϕ_i^k and/or of the terminal currents $\mathcal{W}_i^k$, and additionally assuming that the integral in equation (2.44) could be expressed in the form $\mathcal{W}_j^{21} \cdot R_{ij}^{M\,21}$, then equation (2.44) could be written as

$$\phi_i^2 - \phi_i^1 = \sum_{j=1}^{N} R_{ij}^{M\,21} \cdot \mathcal{W}_j^{21} , \tag{2.45}$$

where $\mathcal{W}_j^{21} = \mathcal{W}_j^2 = -\mathcal{W}_j^1$ are the common terminal currents through Γ_1 and Γ_2. The matrix $\mathbf{R}^M$ is an averaged one, describing the device as a whole instead of a local volume element only. Inverting the matrix $\mathbf{R}^{M\,21}$ to $\mathbf{L}^{M\,21}$ allows to rewrite equation (2.45) as

$$\mathcal{W}_i^{21} = \sum_{j=1}^{N} L_{ij}^{M\,21}(\phi_j^2 - \phi_j^1) \; . \tag{2.46}$$

Adding now the current contributions from all $K-1$ interface nodes $\Gamma_1, \cdots, \Gamma_k$ and the production rate Π_i to the currents through interface Γ_1

$$-\mathcal{W}_i^1 = \sum_{k=2}^{K} \mathcal{W}_i^{k1} \; + \dot{Q}_i - \Pi_i \; , \tag{2.47}$$

one finally gets the following expression for the currents at interface Γ_1 (now lumped into a single value at the device node 1):

$$-\mathcal{W}_i^1 = \sum_{k=2}^{K} \sum_{j=1}^{N} L_{ij}^{M\,k1}(\phi_j^k - \phi_j^1) \; + \dot{Q}_i - \Pi_i \; . \tag{2.48}$$

This equation expresses a nodal current of one extensive quantity as a function of the potential differences from all other nodes to this node, not only for the conjugate potential to the current, but for all other potentials as well.

Because the matrix $\mathbf{L}$ is a function of the intensive state variables I_j, also the matrix $\mathbf{L}^M$ must be dependent on the state of the device. In a CM the state cannot be described by distributed field variables, but averaged, lumped variables must be used instead.

A next, important assumption is, that the state of the device can be uniquely described by a set of averaged, intensive state variables:

$$f(\phi_i^M) = \frac{\int_V f(I_i)\,\mathrm{d}V}{\int_V \mathrm{d}V} \; . \tag{2.49}$$

One important task of compact modeling is it to find an appropriate function f such that relations like (2.46) hold true. Their conjugate, averaged extensive state variables are

$$Q_i^M = \int_V E_i \,\mathrm{d}V \; . \tag{2.50}$$

This is the obvious way of averaging an extensive quantity which has to fulfill a conservation law.

The intensive and extensive state variables are assumed to satisfy a relation corresponding to the state equation (2.6) for the thermodynamic equilibrium

$$\phi_i^M = \sum_{j=1}^{N} \alpha_{ij}^M Q_j^M \; , \tag{2.51}$$

and with the generalized capacity matrix $\mathbf{C} = \alpha^{-1}$ one gets the following capacity relation

$$Q_i^M = \sum_{j=1}^{N} C_{ij}^M \phi_j^M \; . \tag{2.52}$$

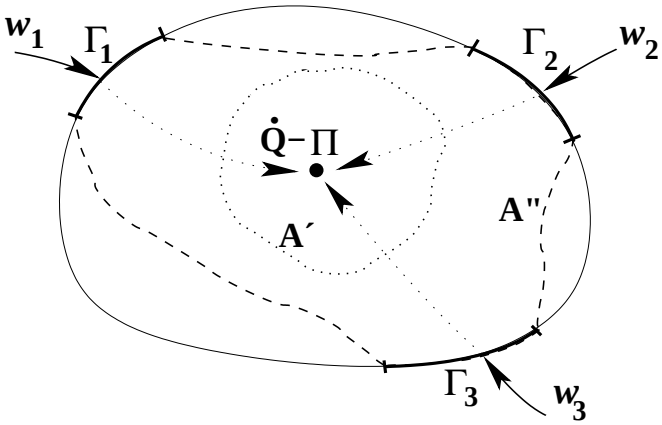

Fig. 2.5: Schematic view of a system with three interfaces and an internal node. The conservation of the flux must hold true for any integration surface A' or A'', thus making the node rule for currents obvious.

Again, the raised indices M indicate averaged values, describing the state of the entire device, not of an infinitesimally small volume element.

In the case that the coefficients of $\mathbf{L}^M$ are constant or can be explicitly expressed as functions of the node potentials ϕ_i^k and, additionally, neither $\dot{Q}_i$ nor Π_i occur, the variables ϕ_i^M and Q_i^M do not enter the CM and equation (2.48) simplifies to

$$-\mathcal{W}_i^1 = \sum_{k=1}^{K} \sum_{j=1}^{N} L_{ij}^{M\,k1}(\phi_j^k - \phi_j^1) \;, \tag{2.53}$$

and equation (2.53) becomes the generic form of a quasi-static CM.

If however such an explicit expression cannot be found, the variables ϕ_i^M and Q_i^M enter the CM as internal node variables (Fig. 2.5). To be more precisely, not Q_i^M, but $\dot{Q}_i^M$ is used, and therefore the conservation law for the quantity Q_i is written as

$$\sum_{k=1}^{K} \mathcal{W}_i^k = -\dot{Q}_i^M + \Pi_i \;, \tag{2.54}$$

with Π_i being the production rate of quantity Q_i inside the device. Equation (2.45) changes to

$$\phi_i^M - \phi_i^1 = -\sum_{j=1}^{N} R_{ij}^{M\,1} \cdot \mathcal{W}_j^1 \tag{2.55}$$

and can be inverted to

$$-\mathcal{W}_i^1 = \sum_{j=1}^{N} L_{ij}^{M\,1}(\phi_j^M - \phi_j^1) \;. \tag{2.56}$$

This means, that a current at a node is expressed as a function of the potential difference between this node and the device internal node (Fig. 2.6). Now the equation (2.56) for all nodes and all quantities, together with (2.54) and (2.52) establish the generic CM.

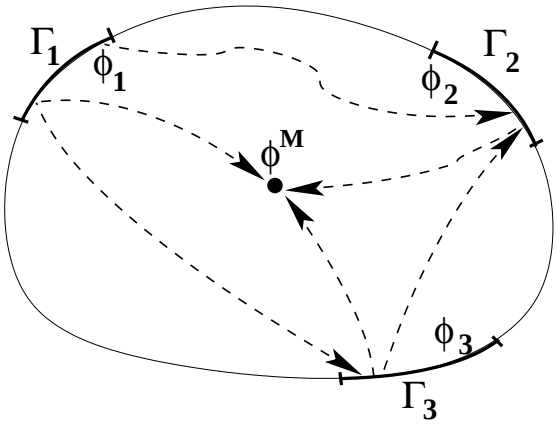

Fig. 2.6: Schematic view of a system with three interfaces and an internal node. Any integration of an affinity along an arbitrary, but closed path must vanish, thus making the mesh rule for potentials obvious.

For the change in internal energy of the device due to a change of the quantity Q_i^M one gets in analogy to equation (2.2)

$$\mathrm{d}U_i^M = \phi_i^M \cdot \mathrm{d}Q_i^M \; . \tag{2.57}$$

Replacing ϕ_i^M by using equation (2.51) yields

$$\mathrm{d}U_i^M = \sum_{j=1}^{N} (Q_j^M \cdot \alpha_{ij}^M) \; \mathrm{d}Q_i^M \; . \tag{2.58}$$

This means, that the capability of a device to store a quantity Q_i is related to the capability of storing energy.

The entropy production inside the device is corresponding to (2.17):

$$\dot{S} = -\sum_{k=1}^{K} \sum_{j=1}^{N} \mathcal{W}_j^k \cdot (\phi_j^M - \phi_j^k) \tag{2.59}$$

2.3.3 An additional affinity for inertial effects

If the change of a flux $\dot{\mathcal{W}}_i^{k1}$ in a device causes an additional affinity $f_i^k = K_i^{M\,k1} \cdot \dot{\mathcal{W}}_i^{k1}$ to occur, then equation (2.45) must be modified in the following way:

$$\phi_i^k - \phi_i^1 - K_i^{M\,k1} \cdot \dot{\mathcal{W}}_i^{k1} = \sum_{j=1}^{N} R_{ij}^{M\,k1} \cdot \mathcal{W}_j^{k1} \tag{2.60}$$

and can be inverted to

$$L_{ii}^{M\,k1} \cdot K_i^{M\,k1} \cdot \dot{\mathcal{W}}_i^{k1} + \mathcal{W}_i^{k1} = \sum_{j=1}^{N} L_{ij}^{M\,k1} \cdot (\phi_j^k - \phi_j^1) \; . \tag{2.61}$$

For device CMs with an internal node the corresponding change to equation (2.55) is

$$\phi_i^M - \phi_i^1 + K_i^{M\,1} \cdot \dot{\mathcal{W}}_i^1 = -\sum_{j=1}^{N} R_{ij}^{M\,1} \cdot \mathcal{W}_j^1 \tag{2.62}$$

and this relation can be inverted to

$$L_{ii}^{M\,1} \cdot K_i^{M\,1} \cdot \dot{\mathcal{W}}_i^1 + \mathcal{W}_i^1 = -\sum_{j=1}^{N} L_{ij}^{M\,1} \cdot (\phi_j^M - \phi_j^1)\ . \tag{2.63}$$

In another notification equation (2.62) reads:

$$\phi_i^M - \phi_i^1 = -\sum_{j=1}^{N} (R_{ij}^{M\,1} + K_{ij}^{M\,1} \frac{\partial}{\partial t})\ \mathcal{W}_j^1 \tag{2.64}$$

with $\mathbf{K}$ being a diagonal matrix, i.e. $K_{ij} = 0 \ \ \forall\ i \neq j$. This matrix operator relates the potential difference between a terminal node and the internal device node to all nodal currents. Together with the capacity relation (2.52) and the conservation law (2.54) for currents, equation (2.64) is a general, generic CM of a device, that could be derived from irreversible thermodynamics and, therefore, leads to a generalized Kirchhoffian network description of the embedding system.

Corresponding to (2.17) the contribution of the affinity $f_i^k = K_i^{M\,1} \cdot \dot{\mathcal{W}}_i^1$ to the entropy production in the device is

$$\dot{S}_i^k = \mathcal{W}_i^1 \cdot f_i^k\ . \tag{2.65}$$

Using $\mathrm{d}U = T\,\mathrm{d}S$ one gets:

$$\dot{U}_i^k = T \cdot f_i^k \cdot \mathcal{W}_i^1 \tag{2.66}$$

$$\mathrm{d}U_i^k = T \cdot f_i^k \cdot \mathcal{W}_i^1\,\mathrm{d}t \tag{2.67}$$

$$\Delta U_i^k = \int_{t_0}^{t} T \cdot K_i^{M\,1} \cdot \dot{\mathcal{W}}_i^1 \cdot \mathcal{W}_i^1\,\mathrm{d}t' \tag{2.68}$$

$$= \int_{\mathcal{W}_i^1(t_0)}^{\mathcal{W}_i^1(t)} T \cdot K_i^{M\,1} \cdot \mathcal{W}_i^1\ \mathrm{d}\mathcal{W}_i^{1\,\prime} \tag{2.69}$$

$$= \frac{K_i^{M\,1}}{2}(\mathcal{W}_i^1(t))^2 - \frac{K_i^{M\,1}}{2}(\mathcal{W}_i^1(t_0))^2 \tag{2.70}$$

This is the amount of energy ΔU_i^k stored in the current $\mathcal{W}_i^1$ and means that a current, which itself stores energy, leads to the effect that changing this current requires an additional affinity of the same type as the one, which drives the current.

2.3.4 Simple examples

In Table 2.1, intensive and extensive thermodynamic variables and the corresponding conjugate affinities (driving forces) and fluxes are listed for several physical energy domains.

domain	intensive quantity I_i	affinity $\vec{f}_i$	flux $\vec{J}_i$	extensive quantity E_i
electrical	ϕ/T	$-\nabla(\phi/T)$	$\vec{J}_{el}$	Q_{el}
mechanical	$\vec{v}/T$	$\nabla(\vec{v}/T)$	$\vec{F}$	$\vec{p}$
thermal	$1/T$	$\nabla(1/T)$	$\vec{J}_S$	S
fluidic	p/T	$\nabla p/T$	$\vec{J}_m$	m

Tab. 2.1: Intensive and extensive state variables and the corresponding conjugate affinities and fluxes for several physical disciplines.

Table 2.2 shows the across- and through-quantities in compact models which correspond to the affinities and fluxes in CFMs in Table 2.1. The quantity heat (Q_{th} in Table 2.2) is related to the entropy S in Table 2.1 by $\mathrm{d}Q_{th} = T\mathrm{d}S$.

domain	across quantity	through quantity	conserved quantity
electrical	U	I	Q_{el}
mechanical	$\Delta\vec{v}$	$\vec{F}$	$\vec{p}$
thermal	$\Delta T\,/\,T$	I_{th}	Q_{th}
fluidic	Δp	w_m	m

Tab. 2.2: Nodal quantities in a generalized Kirchhoffian network description, for several physical disciplines.

It is quite usual to chose the across- and through-quantities such that their products have the dimension of a measurable physical quantity, namely power, instead of entropy production as in equation (2.17). Therefore, the affinities in Table 2.1 are multiplied by T to yield the corresponding across-quantities in Table 2.2, motivated by the relation for the heat production

$$\Pi_Q = \frac{\mathrm{d}Q_{th}}{\mathrm{d}t} = T \cdot \frac{\mathrm{d}S}{\mathrm{d}t} \,. \tag{2.71}$$

a) A resistor with self-heating effect

As a very simple example, an electrical resistor is considered now. It is assumed to consist of a cylinder of the length l and the cross-section A, contacted at both sides thermally as well as electrically, but electrically and thermally isolated at the outer cylinder surface. Therefore, all quantities are one-dimensional in space and depend on the x-coordinate only (Fig. 2.7).

The resistor cannot store charge, and no charge is generated inside. Additionally, the conductivity of the material is assumed to be independent of the electrical state of the device, i.e. no explicit dependence on the electric field or the current density is considered. That

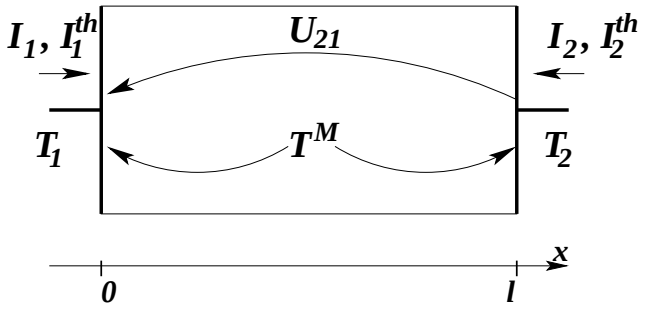

Fig. 2.7: An electrical resistor, contacted thermally and electrically at both sides.

means that no internal node is necessary to model the electrical behavior, and equation (2.53) can be used to describe the relation between electrical current and applied voltage. If we suppose that the temperature at both sides of the resistor is kept at the same value, it can be simplified to

$$-I_1 = L_{el} \cdot U_{21} \ . \tag{2.72}$$

The balance equation (2.47) for currents leads to $I_2 = -I_1$.

The coefficient L_{el} is still a function of the device temperature. Since all quantities are one-dimensional in space, the relation $\vec{j} = \sigma \cdot \vec{E}$ can easily be integrated, if additionally the temperature inside the device is assumed to be constant. This is not truly the case, but an averaged value T^M is used to describe the thermal state of the device. This results in the well-known formula for the electrical conductance of a device

$$L_{el} = \sigma(T^M) \cdot A \,/\, l \ . \tag{2.73}$$

Applying equations (2.59) and (2.71), the Joule heating inside the device calculates to $\Pi_Q = U \cdot I$. This value appears as production term in the thermal balance.

To describe the thermal behavior of the device, constant thermal conductivity and heat capacity are assumed. Equations (2.56), (2.54) and (2.52) must be applied to set up the thermal model:

$$-I_k^{th} = \lambda_k^M \cdot (T^M - T_k) \ , \qquad k = 1, 2 \tag{2.74}$$

$$I_1^{th} + I_2^{th} = -\dot{Q}_{th}^M + U \cdot I \tag{2.75}$$

$$\Delta Q_{th}^M = C_{th}^M \cdot (T^M - T_1) \ . \tag{2.76}$$

Equations (2.72) to (2.76) are the CM for the resistor. Using the device symmetry $\lambda_1^M = \lambda_2^M = \lambda^M$ and the boundary condition $T_1 = T_2$, it can be simplified to

$$I = \sigma(T^M) \cdot (A/l) \cdot U \tag{2.77}$$

$$-I_1^{th} = -I_2^{th} = \lambda^M \cdot (T^M - T_1) \tag{2.78}$$

$$C_{th}^M \cdot \frac{\mathrm{d}(T^M - T_1)}{\mathrm{d}t} + 2 \cdot \lambda^M \cdot (T^M - T_1) = \frac{2 \cdot A}{l} \cdot \sigma(T^M) \cdot U^2 \ . \tag{2.79}$$

It still remains to determine the averaged coefficients $\sigma(T^M)$, λ^M and C_{th}^M.

The governing equations for the local, distributed-field variables can be found by condensing (or tailoring, see [8]) the generic thermodynamic model, described in section 2.2:

$$\frac{\partial j}{\partial x} = 0 \tag{2.80}$$

$$j = \sigma(T(x)) \cdot E(x) \tag{2.81}$$

$$-\frac{\partial j_{th}}{\partial x} = -\dot{Q}_{th} + j \cdot E(x) \tag{2.82}$$

$$j_{th} = \lambda \cdot \frac{\partial T(x)}{\partial x} \tag{2.83}$$

$$\dot{Q}_{th} = C_{th} \cdot \dot{T}(x)\ . \tag{2.84}$$

Since the problem is assumed to be one-dimensional and, because of (2.80) one can replace j by I/A. Some manipulation finally leads to the one-dimensional, inhomogeneous heat-flow equation

$$\frac{\partial}{\partial x}\left(\lambda(T(x)) \cdot \frac{\partial T(x)}{\partial x}\right) + C_{th} \cdot \dot{T}(x) - \frac{I^2}{A^2 \cdot \sigma(T(x))} = 0\ . \tag{2.85}$$

If λ can be assumed to be constant, it further simplifies to

$$\lambda \cdot \frac{\partial^2 T(x)}{\partial x^2} + C_{th} \cdot \dot{T}(x) - \frac{I^2}{A^2 \cdot \sigma(T(x))} = 0\ . \tag{2.86}$$

Now lets consider equation (2.81). A direct integration gives

$$\int_0^l E(x)\,\mathrm{d}x = \frac{I}{A}\int_0^l \frac{\mathrm{d}x}{\sigma(T(x))}\ . \tag{2.87}$$

That leads to

$$R = \frac{U}{I} = \frac{1}{A}\int_0^l \frac{\mathrm{d}x}{\sigma(T(x))} \tag{2.88}$$

and makes the following definition for T^M obvious:

$$\frac{l}{\sigma(T^M)} = \int_0^l \frac{\mathrm{d}x}{\sigma(T(x))}\ . \tag{2.89}$$

The idea behind this definition is: the electrical properties of the resistor are the most important ones and must be modeled as accurate as possible. Therefore, the measured material property $\sigma(T)$ should be used. The detailed thermal properties are considered to be less important in this example and can be modeled by approximate parameters.

The generated power due to Joule heating inside the resistor is

$$\begin{aligned} P = U \cdot I &= \int_0^l A \cdot j \cdot E(x)\,\mathrm{d}x \\ &= \frac{I^2}{A} \cdot \int_0^l \frac{\mathrm{d}x}{\sigma(T(x))}\ . \end{aligned} \tag{2.90}$$

Comparing this to (2.89) shows, that the above definition for the averaged T^M yields the correct generated power due to Joule heating.

Integrating the stationary part of the heat-flow equation (2.85) and using (2.89) gives

$$\begin{aligned} \int_0^l \frac{\partial}{\partial x}\left(\lambda(T(x)\frac{\partial T(x)}{\partial x})\right)\mathrm{d}x &= \frac{I^2}{A^2}\cdot\int_0^l \frac{\mathrm{d}x}{\sigma(T(x))} \\ \lambda(T(x))\cdot\frac{\partial T(x)}{\partial x}\Big|_0^l &= \frac{I^2\cdot l}{A^2\cdot\sigma(T^M)}\,. \end{aligned} \tag{2.91}$$

If now the gradient $\partial T(x)/\partial x$ is replaced by the difference $(T^M - T_1)/(l/2)$, $\lambda(T(x))$ must be replaced by λ^M, and one finally gets an equation to determine λ^M:

$$4\cdot\lambda^M\cdot\frac{(T^M - T_1)}{l} = \frac{I^2\cdot l}{A^2\cdot\sigma(T^M)}\,. \tag{2.92}$$

In summary, we find: if a current through the resistor is given, the parameter λ^M in (2.92) must be adjusted such that the resulting temperature T^M, when inserted in $\sigma(T^M)$ in equation (2.77), yields the correct value for the voltage U, compared to measurements or FEM-simulations. A similar fit-procedure must be applied to the parameter C_{th}^M to match the measured or simulated dynamic behavior of the resistor. The material properties λ and C_{th} can be used as initial guess for the fit-procedure.

b) A capacitor

The electrical capacitor is assumed to be a two-terminal device with each terminal being connected to one of the two parallel plates. At each plate, electrical charge can be stored, but the device itself does not store any net charge. To model this device corresponding to the method outlined in section 2.3, it is useful to consider it as two sub-devices one and two, as sketched in Fig. 2.8. The resistors R_1 and R_2, connecting the plates to the terminal

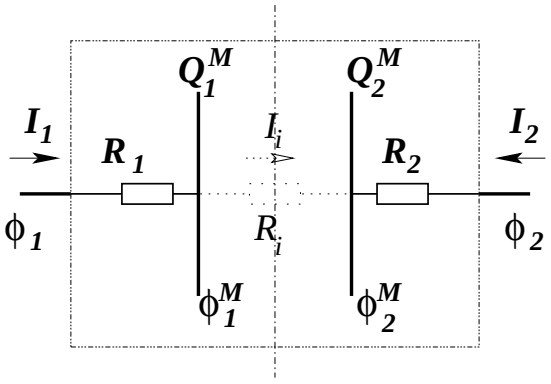

Fig. 2.8: An electrical capacitor, modeled as two sub-devices (indices 1 and 2).

nodes, are assumed to be zero, thus leading to $\phi_1 = \phi_1^M$ and $\phi_2 = \phi_2^M$. The resistor R_i is infinitely large, making I_i to vanish. The CM, derived from the generic CM, described in section 2.3, equation (2.56), (2.54) and (2.52), is therefore fairly simple:

$$I_k = \dot{Q}_k^M = C_k^M\cdot\dot{\phi}_k\,, \qquad k = 1, 2\,. \tag{2.93}$$

Because the device itself must remain neutral, it must always be $Q_1^M = -Q_2^M$, and therefore also $I_1 = -I_2$. By eliminating I_2, equation (2.8) can be simplified to

$$2 \cdot I_1 = C^M \cdot (\dot{\phi}_1 - \dot{\phi}_2) \,, \tag{2.94}$$

which indeed is the correct formula for an capacitor, if $I = I_1$, $U = \phi_1 - \phi_2$ and $C^M/2 = C$ is used:

$$I = C \cdot \dot{U} \,. \tag{2.95}$$

The stored energy can be calculated corresponding to equation (2.58) to be

$$\mathrm{d}W_{el} \;=\; 2 \cdot Q \cdot \frac{1}{C^M} \cdot \mathrm{d}Q \;=\; \frac{Q}{C} \cdot \mathrm{d}Q \,. \tag{2.96}$$

2.4 VHDL-AMS modeling language

In the past, many attempts have been made to simulate non-standard electrical devices and non-electrical components in analog electrical network simulators like SPICE and its numerous successors.

One approach was to build a network of standard components to resemble the behavior of the device to be modeled. This method is well known as *macro-modeling* [15]. One draw-back of this method is its lack of flexibility, because the standard components do not provide all the required functional dependencies between currents and voltages. The parameterization is tricky, because the standard component models are abused, far away from their usual application. The resulting model is difficult to interprete with respect to the physical meaning of the used building components and their parameters. Model documentation and maintenance are therefore full of problems as well. Because the implementation of components is different in various simulators not only for diodes and transistors, but even for simple elements like resistors, the resulting models cannot be re-used in other simulation environments.

Another approach is called *behavioral modeling*. Here, into the simulator a set of components is implemented with certain parameterized functional dependencies between voltages and currents [16, 17]. That gives the model developer the possibility to build models in nearly the fashion of the original model equations. The resulting simulation model of a device is a (usually small) network of components with the required functions. Therefore it should better be called *behavioral macro-model*. If the provided set of functions is sufficiently large, this approach is well suited for compact modeling. Some draw-backs remain though. The set of functions and their syntactical representation is not standardized. Because no new quantities can be defined, the different natures all appear as being electrical ones, thus making the simulation results difficult to interprete and the models difficult to debug and maintain. Additionally, all quantities must be scaled to the same order of magnitude as currents and voltages typically have. Otherwise the convergence properties and the accuracy of the results suffer. Electromechanical examples can be found in [18, 19], electrothermal ones in [20, 21].

VHDL-AMS [6] is quite comparable to behavioral modeling, but overcomes some of its limitations. Some important advantages are:

- Standardization: IEEE standard 1076.1 assures the portability of all VHDL-AMS model code with only minor work required (mostly related to differences in numerical algorithms)

- Self-documenting: The high-level hardware-description language supports hierarchical designs as well as named entities (devices) and quantities and human-readable keywords.

- A comprehensive set of pre-defined functions is available, including time-derivatives and time-integrals. Internal nodes are supported.

- Conditional statements and many other control statements are available.

– It is a superset of VHDL [22]. Therefore, mixed digital and analog modeling is fully supported, making it possible to model large systems efficiently.

Various examples of microsystem modeling by means of VHDL-AMS can be found in [23].

No detailed introduction to VHDL-AMS will be given here, but instead a fairly simple example is presented, which demonstrates some important features of the modeling language VHDL-AMS. The example is the electrical resistor with thermal self-heating as described in section 2.3.4, and is structured as follows:

First, the required quantities are defined, and tolerance attributes are given to them. These tolerance attributes are usually simulator-dependent and must be adjusted, if the model is ported to another simulation environment.

Next, an entity is defined, describing the external structure of the device, namely the number of its terminal nodes and their nature and the parameters, which can be transferred to the model during instantiation.

Finally, the architecture of the model is described. That includes the definition of internal nodes and the formulation of the model equations. The model equations relate the across- and through–quantities of the nodes to each other. The model compiler checks, that only one of the conjugate pair of quantities at each node is set in the model. The other one is determined by applying the Kirchhoffian rules in the network, the device is connected to.

```
PACKAGE pvo IS

CONSTANT temp_tol :     STRING := "ABSTOL=1.0e-9;
CONSTANT heatflow_tol : STRING := "ABSTOL=1.0e-12;

SUBTYPE T       IS REAL TOLERANCE temp_tol;
SUBTYPE W       IS REAL TOLERANCE heatflow_tol;

NATURE thermal IS
    T       ACROSS
    W       THROUGH

NATURE electrical IS
    voltage ACROSS
    current THROUGH

END PACKAGE pvo;

ENTITY heater IS
GENERIC(R     : REAL :=   1.0;
tk    : REAL :=  -3.0e-3;
                c_th  : REAL;
                r_th  : REAL;
```

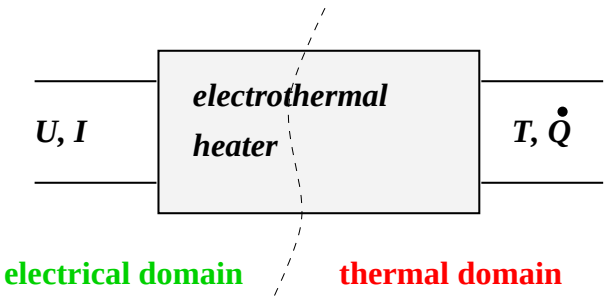

```
);
PORT(TERMINAL v_in, v_out : electrical;
     TERMINAL T_in, T_out : thermal);
END heater;

ARCHITECTURE basic OF heater IS
    QUANTITY T_M: REAL TOLERANCE temp_tol;

    QUANTITY U  ACROSS
             I  THROUGH  v_in TO v_out;
BEGIN

    U == R * (1.0 + tk * T_MReference) * I;

    T_inContribution  == (T_MReference - T_inReference)/r_th;
    T_outContribution == (T_MReference - T_outReference)/r_th;
    (T_MReference - T_inReference)/r_th
    + (T_MReference - T_outReference)/r_th
                      == U*I - c_th*T_MReferencedot;

END basic;
```

There exist other hardware description languages with more or less the same functionality. Non-standard proprietry languages are SpectreHDL [24], Mast [25], HDL-A [26], Analog Insydes [27] and others, whereas Verilog-A, the analog extension to Verilog, aims towards standardization. For a first overview and some historical background see [28]. In this work, mostly SpectreHDL and, to a certain extend, HDL-A have been used. Some models (the valve, section 5.2, and the complete gyroscope model, section 5.5, e.g.) have been ported to VHDL-AMS and could be successfully tested. It turned out that, due to the comparable functionality, a transfer between different hardware description languages is simple but time-consuming.

2.5 Conclusions

In this chapter we described a methodological approach of developing CMs, starting from a thermodynamic description of the system under consideration. A set of equations was derived, which establish a generic CM. Besides the assumption, that the device can be described by means of thermodynamics, the following four fundamental assumptions had to be made:

1. The complete system model can be divided into devices. The interaction of those devices can be described as an exchange of thermodynamic extensive quantities across interfaces.

2. An interface between adjacent devices can be described by a pair of lumped, averaged variables (node potential and node current), being averaged values of the thermodynamic intensive parameter and the flux of the conjugate extensive parameter. Their local distribution along the interface can be neglected.

3. An averaged matrix can be found, that relates the difference of the intensive nodal parameters to the nodal currents. This averaged matrix is still symmetric and positive definite, as the corresponding Onsager matrix is.

4. The state of the device can be described by a set of averaged, lumped intensive state variables. These lumped intensive parameters can be related to the integrated extensive parameters in state equations. The matrix, which relates the intensive to the extensive lumped parameters, is positive definite and symmetric.

It seems worth spending more research work to answering the question, what conditions must be fulfilled, that the above assumptions are valid. An answer on how to find the averaged matrix, mentioned in item 3, would be most desirable. Up to now, it is left to the 'physical intuition' of the model developer to find a solution.

3. Compact modeling approaches

3.1 Introduction

In a product development cycle quite different requests have to be satisfied by CMs used for system-level simulation.

During the conceptual work, the feasibility of the projected system design needs to be verified. Different system concepts are to be compared to find the optimal approach. So, system-level simulations, based on CMs of the used devices are strongly needed. It is very likely, however, that device CMs are not available yet, because the development of the devices themselves or the technology for their manufacturing is not finalized yet. Measurement data might be rarely available either.

One possibility for CM development is then a rough analytical description of the operational principles, based on simple physical models, ignoring many second-order effects, cross couplings etc.

A second consists in characterizing the device behavior by FEM-simulations and the subsequent generation of CMs by means of curve fitting procedures. This approach is especially useful, if CAD- and FEM-models of the device are already available. A change in the device design, however, requires to rerun the FEM-simulation and the curve fitting for the CM.

When the concept of the system is found, it needs to be designed. Here, a detailed quantitative analysis of the system performance and its robustness against process fluctuations has to be carried out. Issues like reliability, design centering, manufacturability etc. must be addressed [29]. This means that many system simulations with systematically varied CM input parameters must be run. It is obvious that analytical, physically based CMs are required here, explicitly expressing the dependencies of the device behavior on design parameters, technological and material parameters etc.

During production the manufacturing process needs to be monitored. If besides process parameters also device CM parameters are measured routinely, correlations between process and geometry parameters, device CM parameters and system parameters can be analyzed [30, 31]. This allows to perform statistical modeling, to build yield models, to perform failure analysis, statistical process control etc [32, 33]. This requires, besides analytical, physically based CMs, a very efficient parameter measurement and extraction strategy, which allows to build up a statistical database.

In this chapter, three different modeling approaches are presented, namely the finite network modeling (FNM), the compact modeling by means of basis functions, and physically based compact modeling, using analytical equations.

FN modeling and basis function modeling can, to a certain extend, be automated, but are not very powerful with respect to changing device parameters like geometries, e.g. Analytical, physically based modeling, on the other hand, is very powerful with respect to parameter studies and has good extrapolation capabilities. However, it requires a lot of experience and time during model development and can hardly be automated.

3.2 Finite network models

The simulation of sensor systems which contain non-electrical components is a non-trivial task. Frequently, the sensing elements of such systems are controlled in a feedback-loop, thus making a coupled simulation necessary. One approach is the coupling of FEM-simulation tools for the non-electrical part with a circuit simulation tool for the electrical part of the system [34, 35]. Since the control unit of the system is realized electronically, the electrical simulation is indispensable. The corresponding software is an analog or mixed analog-digital system simulation tool.An alternative is the Finite Network modeling.

The method of Finite Network modeling reproduces the FEM approach. The governing partial differential equations are discretized, using appropriate ansatz functions in the discretization grid elements. This leads to a large system of linear or nonlinear ordinary differential equations (ODEs). Powerful software tools are available to solve such large systems of nonlinear ODEs. If analog network simulators like Spectre, Eldo, Saber or Hspice are used, linear element ODEs can be represented as RLC equivalent circuits, whereas nonlinear elements must be written as behavioral models, using VHDL-AMS, e.g.. These elements are then compiled into a netlist, thus establishing the simulation model.

The finite network modeling has some advantages, making it very attractive for microsystem modeling. First, the finite network simulation model can be generated automatically from a FEM-mesh. To this end, a software tool called ANTOS has been developed. It converts FEM models from ANSYS, based on brick elements, into a SPICE netlist of a finite network model (FNM). Second, the element formulation is fully flexible, allowing the user to include nearly arbitrary coupling effects, which might not be included in the usual FEM-tools. Finally, the combination of a FN model with CMs is possible and allows the simultaneous solution of the complete system model. Especially in the case of strong bidirectional coupling between the parts of the system modeled by means of FNMs and CMs, that leads to much better convergence properties than a successive coupling between FEM solver and system simulator [36, 37, 38]. Since analog system simulators are used to solve the resulting coupled problems, one benefits from the fact that those simulators are well tuned towards a robust, efficient solution of stiff transient problems, and additionally gets access to all their built-in analysis methods (quasistatic operating point, DC sweep, transient, small signal AC ...).

To make simulations on system level possible, FNMs can be combined with CMs. This means, that the parts of the system modeled by CMs and those modeled by FNMs interface to each other. The interaction at such interfaces must be described by a single pair of conjugate variables. Basically the same considerations as in section 2.3 for lumping an in-

terface into a single node can be applied to the interface nodes of FNMs. Two possibilities are found to be useful:

- The across variables at the FNM interface nodes are forced to be constant, equal to the corresponding nodal value of the CM. The nodal through variable of the CM is the interface-integral of the corresponding flow density of the FN model. This possibility is recommended if a generalized potential is forced from the CM to the interface (the CM acts as a generalized voltage source).
- The nodal through variable of the CM is used to force a constant flow density at the interface to the FNM. The nodal across variable of the CM is then an averaged value of the corresponding nodal values at the interface to the FNM. Instead of averaging over the interface, it is also possible to intentionally select a node as the typical one to describe the interface, therefore using its FNM across variable also as the nodal CM across variable. This possibility is recommended if the CM drives a flow into the interface to the FNM (the CM acts as a generalized current source).

One major disadvantage of this modeling approach is the large amount of degree of freedom in the FN model, usually a multiple of the network node count. This makes simulations very time- and memory-consuming, compared to such simulations which use only CMs. Additionally, geometry variations usually require to rebuild the FN model, starting from a modified FEM model. These two points are the reason, why FN modeling is not well suited for design studies.

Examples for FN modeling of thermal problems can be found in [39], mechanical problems are solved by means of FN in [40, 41, 42, 43, 44], and a complicated, coupled problem can be found in [45]. The application to self-heating effects on chip-level, including a semi-automatic generation of the FN model from layout data is shown in [46].

Since the manual setup of the large system of ODEs is impractical, it is helpful to utilize CAD-tools for solid modeling and mesh generation. All required information like grid node coordinates, cell volumes, element attributes, surface flags, neighboring nodes etc. can be exported from the CAD-tool. A software tool is then required, that builds the required netlist file from these exported data.

For the example presented next in this work, the interface program ANTOS was used to build the Spice netlist of a thermal FN model, based on a brick element mesh, generated in ANSYS. This FN model allows to specify various boundary conditions like clamped temperature, heat convection or radiation. Body loads (heat generation rate, e.g.) can be applied as well. Two alternative approaches were used: First, the relations between the quantities temperature and heat flow-rate between neighboring nodes are expressed using the simulator-built-in linear electrical R and C elements. Second, those relations are written in VHDL-AMS, thus featuring a more general approach, which allows for more complex relations like nonlinearities in material properties etc.

3.2.1 The demonstrator: a thermo-electro-mechanical microsystem

An essential functional feature of microsystems is the ability to verify their functionality, i.e. the possibility to perform self-tests. In the case of an acceleration sensor, one pos-

sibility of a self-test is the controlled excitation of oscillations of the seismic mass and the evaluation of the resulting sensor output signal. One excitation method, which can relatively easily be implemented in the sensor system is a thermal actuation. This method is used in an acceleration sensor, which was developed at the IFT in the publicly founded project ASIS-III [47].

The ASIS acceleration sensor is manufactured in bulk silicon micro-machining technology. A seismic mass as thick as the silicon wafer which it is made from, is attached to the silicon frame by four suspension beams (Fig. 3.1). The beams have integrated resistors, which explore the piezo-resistive effect of crystalline silicon to detect a beam bending due to accelerations of the sensor. The geometry of the beams as well as the placement of the resistors was optimized to get maximum sensitivity to accelerations in the sense direction and minimum sensitivity in the other spatial directions. Additionally, the piezo-resistors are switched together in a bridge circuit in such a way, that other than the desired signals cancel each other out. The beams also contain resistors for heating purposes. A heating of the beams causes a thermal expansion and subsequently a deflection of the seismic mass, given that the frame stays at ambient temperature. The resulting deflection of the seismic mass can be detected, so that finally the functionality of the sensor can be verified. Although the piezo-resistors could serve as heaters as well, the usage of separate heating resistors turned out to be better than to reuse the ppiezo-resistors

To develop a complete self-test regime, simulations on device level as well as on system level had to be performed. A coupled thermo-electro-mechanical system simulation had to clarify, if the electrical response to a heating pulse would provide enough information about the device to serve as self-test. To this end, CMs for all functional parts of the sensor had to be developed. For the mechanical and electrical behavior, the CM development was more or less straight forward and will be described in section 3.2.3. For the thermal behavior, in the given case it would have been possible to build CMs, because the thermal time constants of the constituent parts (beams, frame, seismic mass) are fairly well separated from each other, making it possible to model them separately as lumped elements. Frequently, in thermal problems, the opposite is the case: heat sources and heat sinks are not well localized, but spatially distributed, making it difficult to lump them into CMs. A Finite Network model is an attractive alternative in such situations.

In order to demonstrate that a FNM works well and efficiently in combination with CMs, deliberately a FN description was chosen for the thermal model of the acceleration sensor.

3.2.2 The finite network model

In section 3.2, a method for the FN modeling was described. This method was applied to the thermal simulation of the ASIS acceleration sensor. To this end, a FEM mesh was generated in ANSYS (Fig. 3.1). The ANSYS input deck is fully parameterized, thus allowing for parameter studies like design modifications, e.g. The resulting ANSYS FEM mesh, consisting of brick elements only, is then exported to the software package ANTOS, which generates the desired FNM for thermal modeling. The FNM has 2450 nodes, which leads to 2440 capacitive elements and 7860 resistive elements in the final netlist. The FNM takes into account the thermal conductivity, the thermal capacitance and heat transfer across the surface due to convection and radiation. The convection is

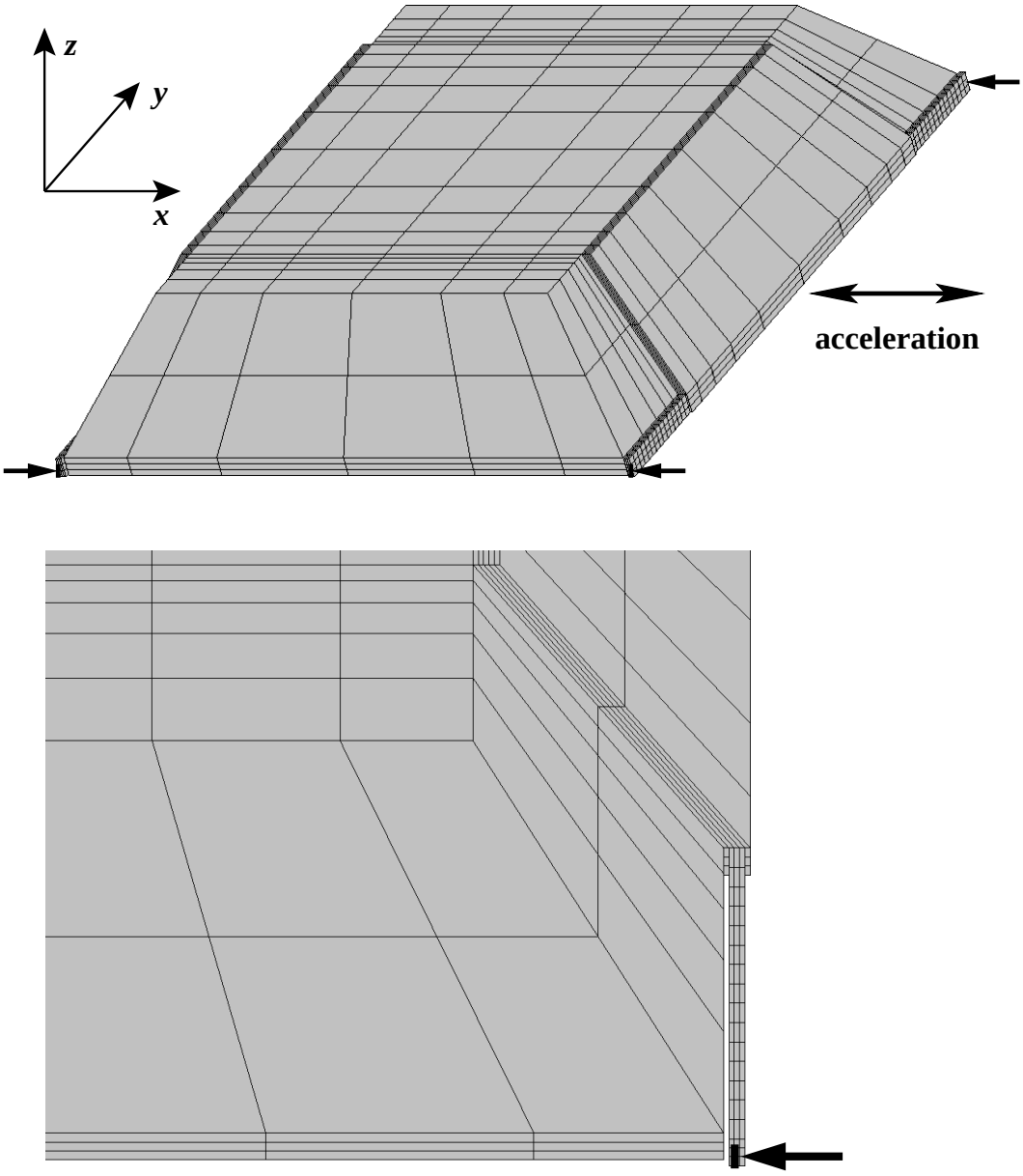

Fig. 3.1: Finite-Element model of the sensor: seismic mass and suspension beams (top) and detailed view of a suspension beam (bottom). The same mesh is used for mechanical and thermal simulations as well as the export to the FNM generator ANTOS. The frame is not modeled. Instead, he suspension beams are given constant temperature and zero displacement boundary conditions at the connecting points to the frame (indicated by arrows).

modeled as a linear thermal resistor from each surface element to a reference, i.e. to the ambient temperature. The heat transfer to the environment due to radiation is modeled to be proportional to T^4.

A transient thermal analysis of the sensor warm-up was performed. Two opposite beams are heated by a power of 3.61mW. The simulation was performed in the analog network simulator Spectre [24], using the generated netlist. The advanced timestepsize control in the analog network simulator is able to resolve transient effects on very different time

scales. This lets the simulation run very efficiently. To simulate the curves shown in Fig. 3.3 takes approximately 30 seconds on a HP9000/785, but still the fast transient temperature raise of the suspension beams gets correctly resolved. The simulation of this problem in ANSYS takes 70 seconds on the same machine. Note that in both cases only the thermal problem is simulated, neglecting the coupling of the thermal effects to the electrical and mechanical behavior of the sensor. A comparison of the simulation results shows negligible differences between the FEM and the FN simulations, as expected (see fig 3.3).

The alternative approach using VHDL-AMS written elements instead of using the simulator-build-in resistive and capacitive elements yields exactly the same results and no significant difference in simulation time, which basically highlights the efficient solution algorithms in Spectre for VHDL-AMS models.

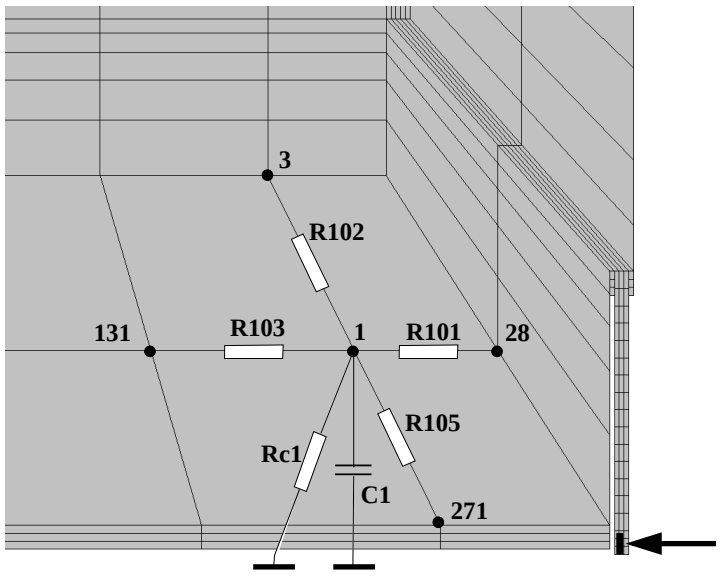

Fig. 3.2: Finite-Element model of the sensor and and sketch of the corresponding finite network. Rc1 represents the surface convection and C1 the thermal heat capacity of the volume associated to node 1.

Below, a part of the input netlist of the FN is given in SPICE format. A sketch is shown in fig. 3.2. The thermal conductivity between neighboring nodes is modeled by linear resistive elements. The heat convection at the surface is modeled by linear resistive elements too, using the naming convention $Rc < node >$. The heat capacity of the volume belonging to a node is modeled as a linear capacitive element. The actual values for those elements are calculated from the FEM-discretization data (node distances, element areas and volumes) by the software tool ANTOS.

```
R101      1    28       80.839
R102      1     3       7426.8
R103      1   131       25.514
R104      1   271       164.98
R105      1  1683       7426.8
Rc1       1     0   3.3746e+07
```

```
C1        1     0   3.6348e-08

R201      2     8       1856.7
R202      2    10       646.71
R203      2   129       191.34
R204      2   270       1200.4
R205      2   481       275.18
Rc2       2     0   2.5307e+08
C2        2     0   4.8468e-09
                  .
                  .
                  .
```

The same part of the netlist is shown below, but SpectreHDL is used to model the relation between the temperature at grid nodes and resulting heat flow rate. The program ANTOS writes only the geometrical data of all elements of the FEM-model into the netlist, namely the distance dx between nodes, the element cross-sectional area A, the element volume V and its material index mi. The actual calculation of the network elements takes place in the FN-element code. The corresponding SpectreHDL model code is presented just below the netlist. The heat radiation is modeled as a nonlinear relation between temperature and resulting heat flow rate.

```
Y1_1s  1     3 genmod  dx=0.00016085  A=6.8976e-11  V=3.6984e-15  mi=2
Y1_2s  1    28 genmod  dx=1.361e-05   A=5.3618e-10  V=2.4325e-15  mi=2
Y1_3s  1   131 genmod  dx=1.3333e-05  A=1.6643e-09  V=7.3968e-15  mi=2
Y1_4s  1  1683 genmod  dx=0.00016085  A=6.8976e-11  V=3.6984e-15  mi=2
Y1_5s  1   271 genmod  dx=2.7776e-05  A=5.3618e-10  V=4.9643e-15  mi=2
Y1_6s  1     0 genmod  dx=0           A=1.6643e-09  V=0           mi=0

Y2_11  2   481 genmod  dx=4e-06       A=2.2683e-11  V=0           mi=0
Y2_1s  2   481 genmod  dx=4e-06       A=4.6293e-11  V=6.1724e-17  mi=2
Y2_21  2    10 genmod  dx=1.361e-05   A=6.6667e-12  V=0           mi=0
Y2_2s  2    10 genmod  dx=1.361e-05   A=6.7023e-11  V=3.0406e-16  mi=2
Y2_3s  2   129 genmod  dx=1.3333e-05  A=2.2192e-10  V=9.8632e-16  mi=2
Y2_4s  2     8 genmod  dx=4.0214e-05  A=6.8976e-11  V=9.246e-16   mi=2
Y2_5s  2   270 genmod  dx=2.7776e-05  A=7.369e-11   V=6.8226e-16  mi=2
Y2_6s  2     0 genmod  dx=0           A=2.2192e-10  V=0           mi=0
                  .
                  .
                  .
```

```
module genmod (n1, n2) (dx, A, V, mi)
node[T,Qp] n1, n2;
parameter real dx = 0.0; // distance to neighbor node
parameter real A  = 0.0; // area
parameter real V  = 0.0; // volume
parameter real mi = 0.0; // material index (if 0, then surface)
{
    real c_th, y_th, y_cv, y_rd;
//  Model parameters, to be set in a model file
//                   (or during instantiation)
    parameter real T_ref  = 300.0;
    parameter real lambda = 157.0;
    parameter real cw     = 2330.0*703.0;
```

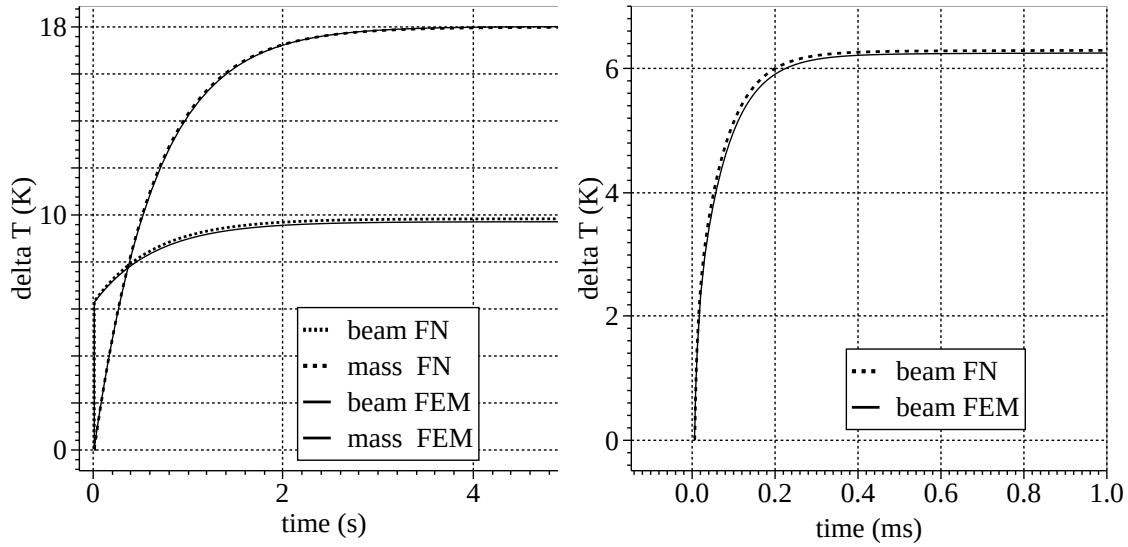

Fig. 3.3: Transient simulation of the sensor warm up, comparing FEM and FN model. Two opposite beams are heated by a power of 3.6mW. The temperature is shown at the heated beams and at the center of the seismic mass. Right hand side: detailed view of the first millisecond after the power has been applied.

```
    parameter real alpha  = 25.7/5.0;
    parameter real a_rad  = 1.0e-3;
    initial {
        y_th = lambda * A / dx;
        c_th = cw * V;
        y_cv = alpha * 2.0 * A;
        y_rd = a_rad * 2.0 * A;
    }
    analog {
        if ( (mi > 0.0) && (dx > 0.0) ) { // inner node
           Qp(n1)    <- c_th * dot(T(n1));
           Qp(n1,n2) <- y_th * T(n1,n2);
        } else {                          // surface with convection
           Qp(n1)    <- y_cv * T(n1);
           Qp(n1)    <- y_rd *( pow(T(n1)+T_ref,4) - pow(T_ref,4) );
        }
    }
}
```

The effect, that the suspension beams warm up ten thousand times faster than the seismic mass, led to the idea to perform a dynamic instead of a static self-test. A pulsed heating regime was simulated (Fig. 3.4), showing the expected result, that the temperature of the suspension beams follows the heating pulses, whereas the seismic mass remains nearly at a constant temperature. This is an important input for the development of compact models for the mechanical behavior of the sensor, which will be described next.

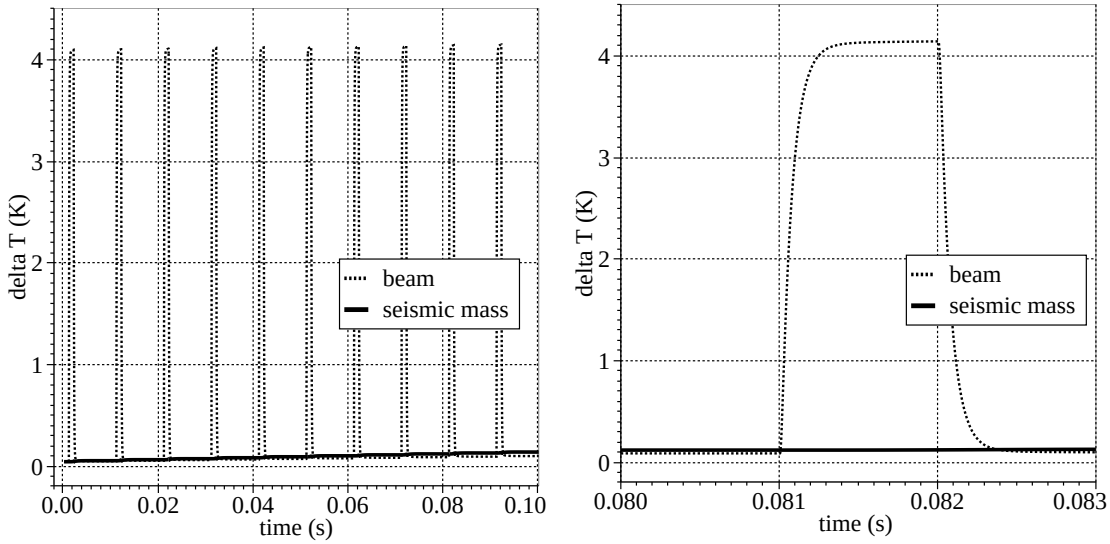

Fig. 3.4: Transient FN simulation of the sensor warm up. Two opposite beams are heated by a pulsed power of 3.6mW, pulse width 1ms, pulse period 10ms. The temperature is shown at the heated beams and at the center of the seismic mass. Right hand side: detailed view of a single power pulse.

3.2.3 The compact model

To develop a CM for the mechanical behavior of the sensor, a FEM analysis was performed. The first step was a modal analysis, yielding the results given in table 3.1 and Fig. 3.5. The simulation model is the same as the one shown in Fig. 3.1. It turned out that

Mode	Frequency (Hz)
1	8 395
2	26 576
3	40 205
4	49 620
5	177 310
6	212 020
7	932 360

Tab. 3.1: Mechanical resonance frequencies of the seismic mass as a result of a FEM modal analysis.

the seismic mass does not show any significant deformations and, therefore, can be treated as a lumped mass. The mechanical behavior of the suspension beams can be described by an analytical formula for clamped beams from [48]:

$$x = 2 \cdot F_x \frac{(l/2)^3}{3 \cdot D} \tag{3.1}$$

$$D = \frac{E \cdot w^3 \cdot h}{12 \cdot (1 - \nu)} . \tag{3.2}$$

Here, F_x stands for the force acting on the beam in the sensor's sense direction, and x, w, h and l are the displacement of the seismic mass and the width, height and length of the suspension beam, respectively. E and ν are the modulus of elasticity and the Poisson ratio.

A quasi-static FEM analysis and its comparison to the modal analysis shows that it should be possible to selectively excite eigenmodes by selecting the appropriate beams for heating. However, one can read from Fig. 3.6, that it is not possible to stimulate the first mode separately, but modes two and four would be excited as well. Still, since the desired motion in sense direction is caused, this heating regime is chosen for the sensor self-test.

A transient FEM analysis must be performed to find out what kind of deflections of the seismic mass would be caused by the selected heating regime. It shows that a heating pulse stimulates significant oscillations only in the sense mode (Fig. 3.7), which is very desirable and intentionally caused by a corresponding aspect ratio of the cross-section of the suspension beams (height much larger than width). The deflection out of the wafer plane (z-direction) can be neglected, because the piezo-resistors in the suspension beams, which detect the beam bending, are switched together as a bride circuit in such a way, that the resulting signals due to a z-deflection cancel out each other. Therefore, it is sufficient in the CM to model deflections in sense direction only. The sensor deflection due to a temperature change in the heated suspension beams (thermal expansion) is taken into account in the CM by a force term acting on the seismic mass. This force term is assumed to depend linearly on the temperature change of the suspension beams and the seismic mass and is fitted to FEM simulation results to yield the correct deflections.

The piezo-resistors are modeled by the following equations

$$R = R_0 \cdot (1 + r_{PK} \cdot x + r_{TK} \cdot \Delta T) \tag{3.3}$$

$$P = R \cdot I^2 \,, \tag{3.4}$$

where r_{PK} describes the change of resistivity due to a beam deflection x and is subject to calibration by measurements. ΔT is the temperature difference of the piezo-resistor to a reference temperature. P is the Joule heating due to an electrical current I, either a heating current or a measurement current through the piezo-resistor. In this manner, the piezo-resistor CM describes the coupling between mechanical, electrical and thermal domains.

In the FEM simulations, no damping due to the air was taken into account. Instead, a small, but arbitrary value for structural damping was used. In the CM, a damping force proportional to the velocity of the seismic mass was introduced. The corresponding damping parameter needs to be adjusted to match measurement results.

Advanced models for squeeze film damping are available, using either a FN approach or a CM [49, 45, 50, 51], and can be readily combined with the presented sensor model.

3.2.4 Simulation results

The CMs are composed to build a macro-model of the entire acceleration sensor. The coupling between mechanical, thermal and electrical behavior occurs in the beams, which

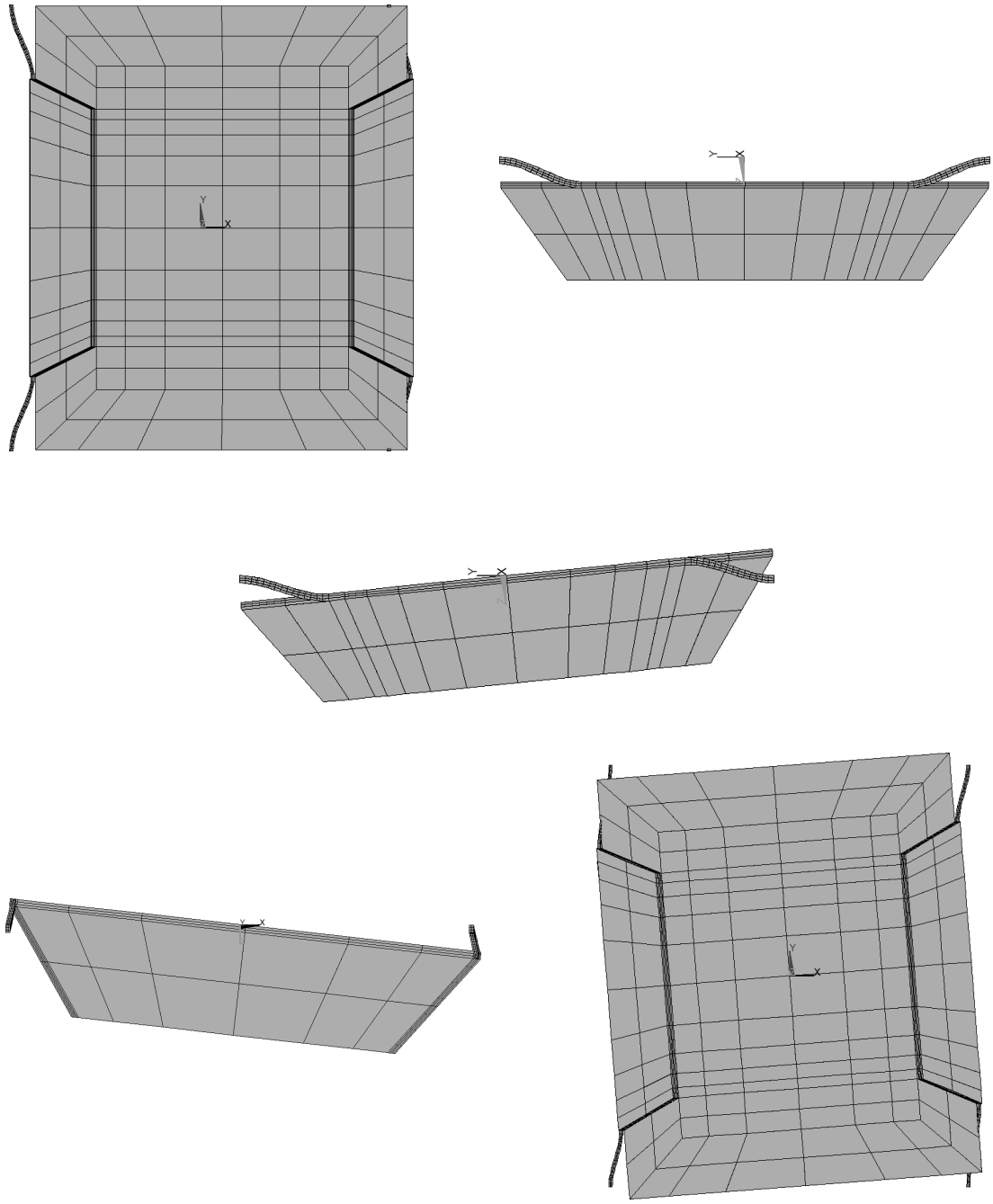

Fig. 3.5: FEM modal analysis: mode shapes of the four lowest and the sixth eigenmodes. Top left: the first mode is a translation in the sense direction of the sensor. Top right: the second mode is a translation out of the wafer plane. Middle and bottom: the higher modes are rotational ones.

contain the heaters and the piezo-resistors and act as mechanical springs between seismic mass and frame (Fig. 3.8).

A small signal modal analysis of the complete sensor system was performed, sweeping

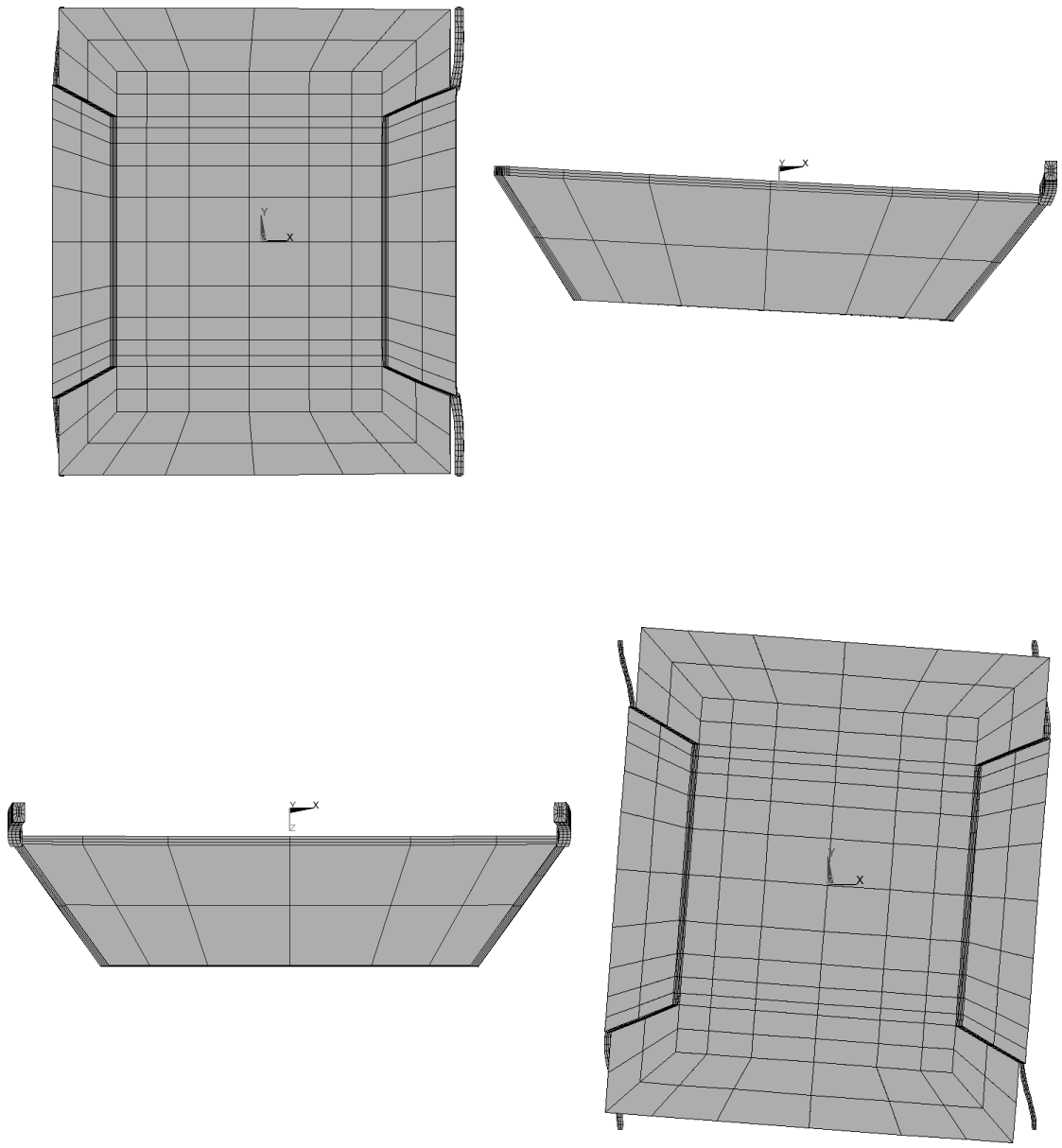

Fig. 3.6: FEM quasi-static thermo-mechanical analysis. A temperature raise of suspension beams is forced and the resulting mechanical deflection shown. Top: the two beams on the right are heated. Bottom: all four resp. two diagonally opposite beams are heated.

the frequency of the heat generation rate in the piezo-resistors of two opposite suspension beams from 1Hz to 1MHz. The results, presented in Fig. 3.9 to 3.11, show that above a few Hertz the temperature of the seismic mass cannot follow the input heating signal. The mass of the suspension beams however is much smaller than that of the seismic mass, making it possible for the temperature to follow the forced heat generation rate

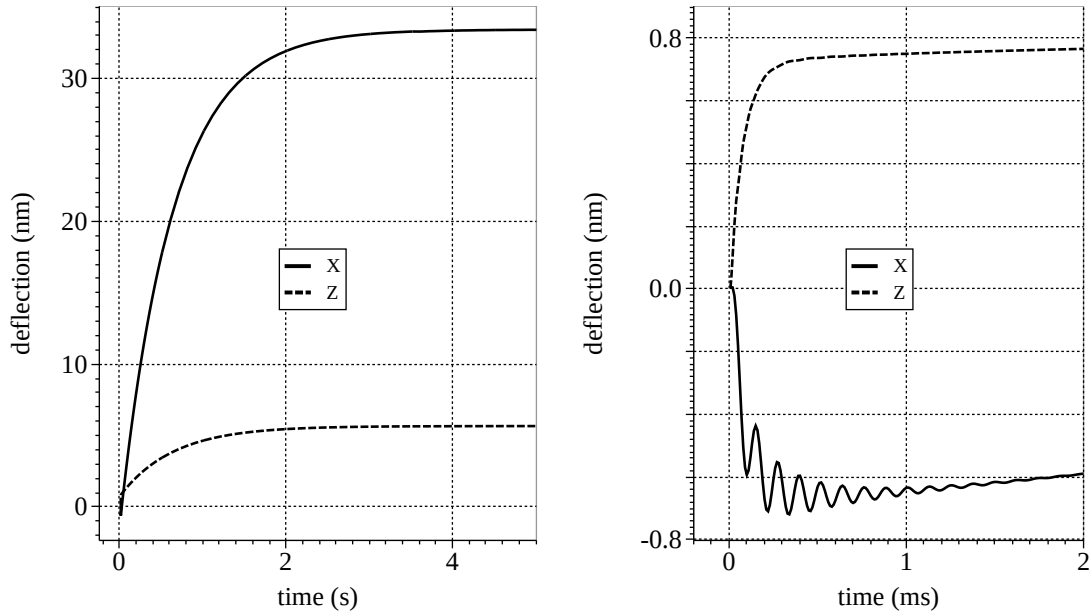

Fig. 3.7: FEM transient thermo-mechanical analysis. A heat generation rate of 3.6mW is applied to two suspension beams, and the resulting mechanical deflection in x and z direction is shown. Right: detailed view of the first two milliseconds, showing oscillations only in the x direction.

up to a frequency of approximately 1kHz. The resulting mechanical deflection of the seismic mass shows a resonance peak at 8.4kHz, which corresponds to the ground mode of the mechanical system (see table 3.1). Those findings show that a thermal excitation of mechanical oscillations is possible and can be explored to develop a self-test regime for the sensor.

A transient simulation of the self-test was performed, using the developed macro-model. A heating pulse of 1ms duration causes the expected oscillations of the seismic mass (Fig. 3.12). The resulting bending of the suspension beams causes a corresponding modulation of the piezo-resistors, which again leads to a cross-voltage in the bridge circuit formed by the piezo-resistors (Fig. 3.13). Additionally that causes a modulation of the heat generation rate, providing a coupling from the mechanical via the electrical to the thermal domain. To model this in a FEM tool, though possible, would be a challenging task.

Since it would require a significant effort to develop and to manufacture a circuit which performs the switching from heating to measurement regime as it would be required if the piezo-resistors were re-used for heating the beams, it was decided to realize separate heating resistors at the suspension beams. The layout problem to place the required connecting wires on the narrow suspension beams turned out to be solvable.

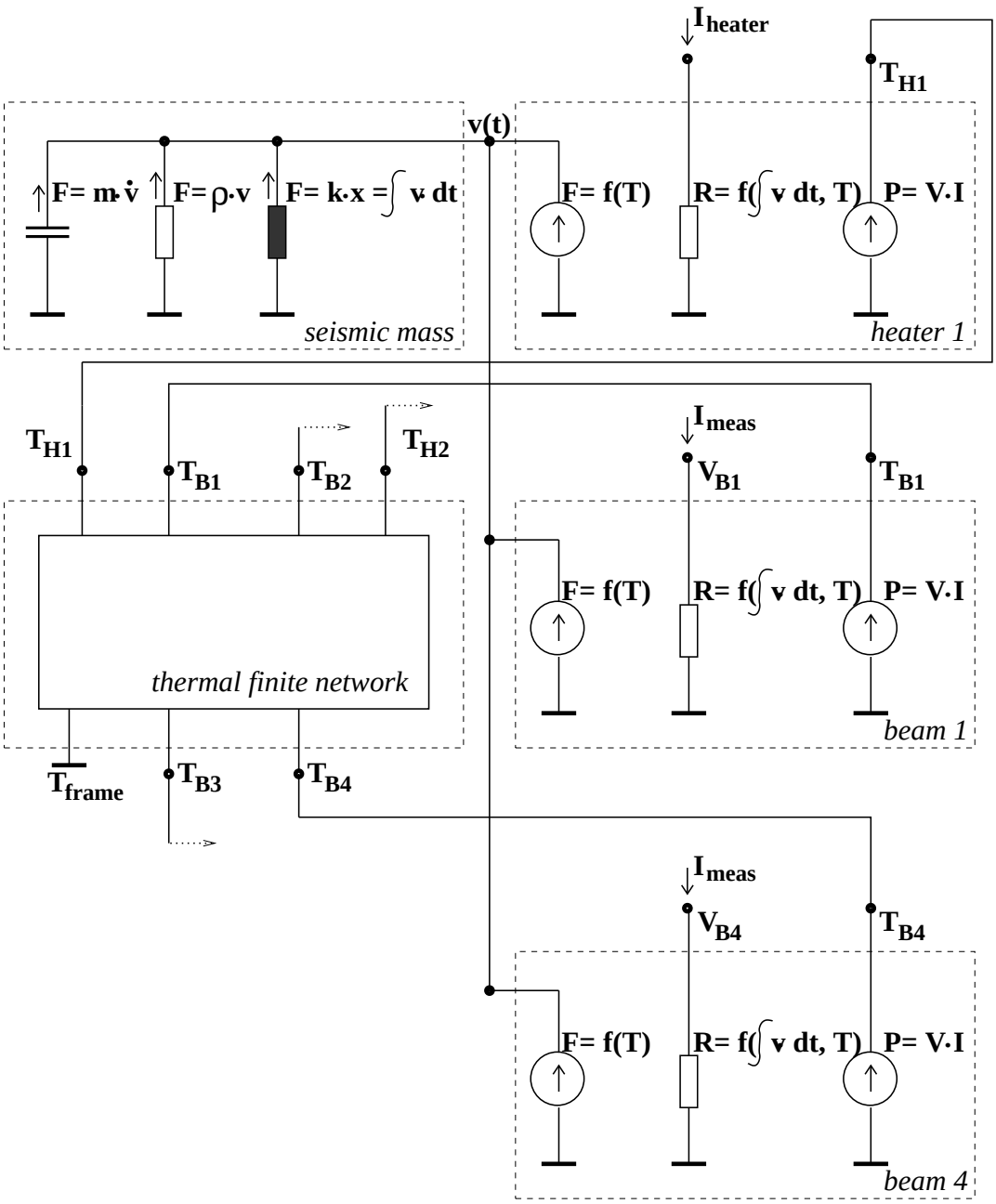

Fig. 3.8: Macro-model of the ASIS-acceleration sensor. Only one heater and two of the four piezo-resistors (labeled beam1 and beam4) are shown. The piezo-resistors couple the thermal, mechanical and electrical behavior. Electrically they are switched to a bridge.

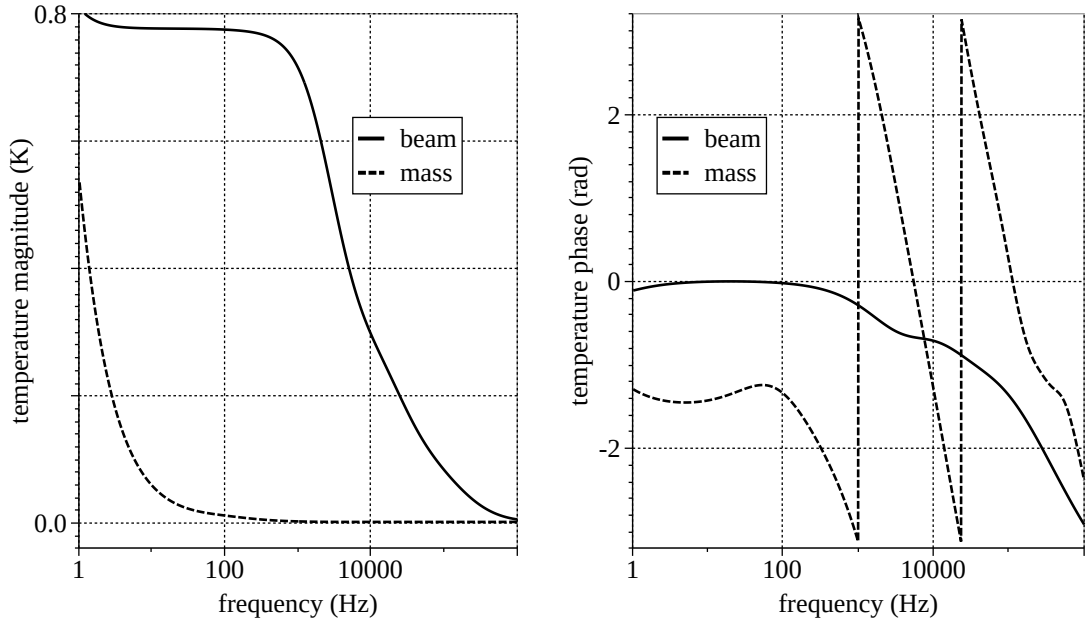

Fig. 3.9: Coupled FNM and CM thermo-mechanical simulation. A small signal analysis is performed, sweeping the frequency of the resistive beam heating from 1Hz to 1MHz. It shows that for frequencies above 1kHz the temperature of the seismic mass cannot follow the transients of the heat generation.

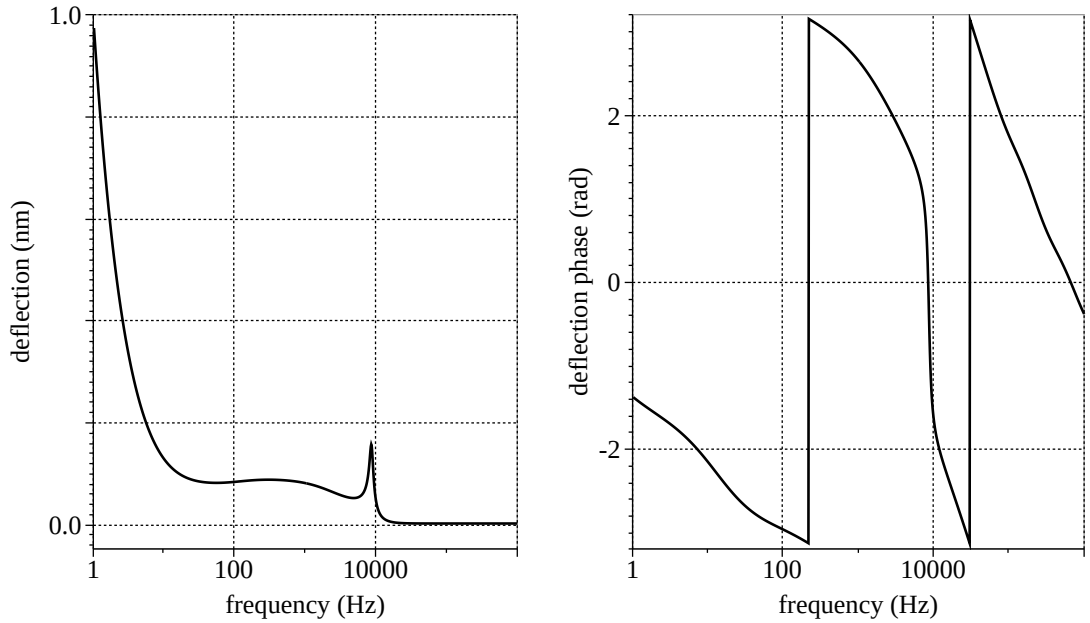

Fig. 3.10: Coupled FNM and CM thermo-mechanical simulation. A small signal analysis is performed, sweeping the frequency of the resistive beam heating from 1Hz to 1MHz. It shows that the seismic mass can be driven into resonance at it's ground mode at 8.4kHz.

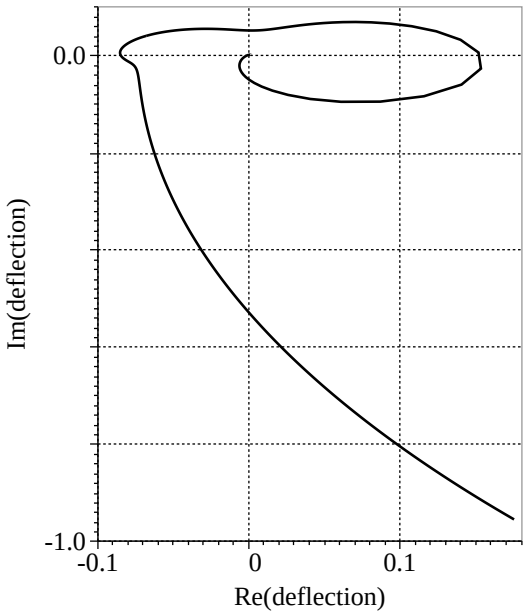

Fig. 3.11: Coupled FNM and CM thermo-mechanical simulation. A small signal analysis is performed, sweeping the frequency of the resistive beam heating from 1Hz to 1MHz. A plot of imaginary versus real part of the deflection shows the typical picture of an oscillatory system with multiple time constants.

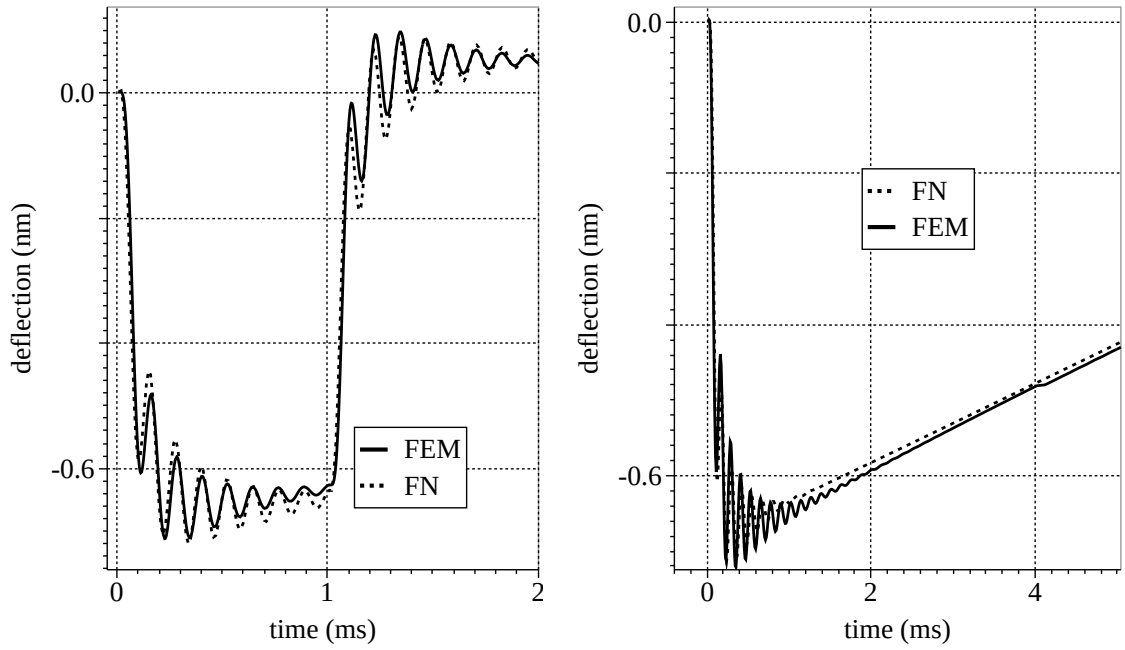

Fig. 3.12: Coupled FNM and CM thermo-mechanical simulation. A heating current pulse from 1 to 2 ms (left) and a step-like increase of the heating current (right) is applied to the piezo-resistors in two suspension beams, corresponding to the chosen self-test regime. The presented mechanical deflection in sense direction shows the expected oscillations.

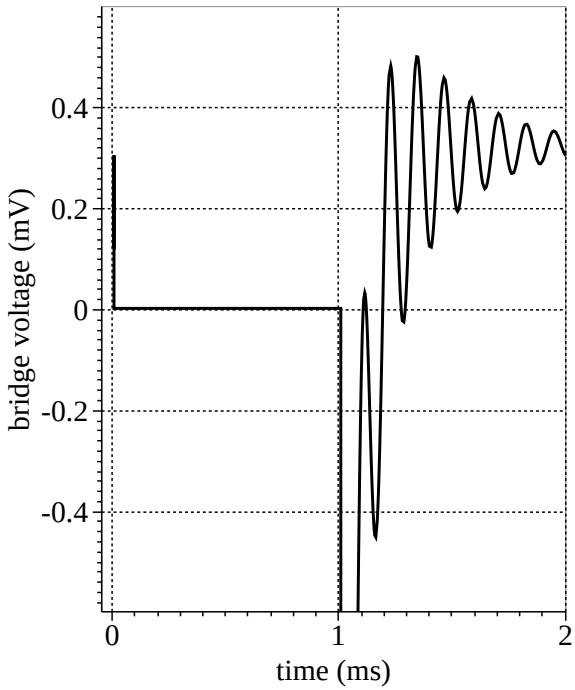

Fig. 3.13: Coupled FNM and CM thermo-mechanical simulation. A heating current pulse of 1 millisecond duration is applied to the piezo-resistors in two suspension beams, corresponding to the chosen self-test regime. The resulting cross voltage at the piezo-bridge shows the expected oscillations. During the heating pulse any output from the bridge is suppressed.

3.3 Basis-functions approach

A crucial problem for the simulation of systems is the generation of efficient device models, which still capture all relevant information about the device behavior. A FEM device model typically has the required accuracy but suffers from high numerical effort required during simulation, making its usage impossible in most system simulation applications.

Since for the system aspect only very few parameters of a device are relevant, the question rises how to generate a device model that describes the device behavior in terms of a very small set of state variables. One approach is to start from a FEM device model and to look for a way to reduce its large amount of degree of freedom.

A frequently used way for model order reduction is to perform a linear modal analysis and to express the spatial variation of the state variables in terms of a small series of modal eigenfunctions [52, 53, 54]. For a limited set of electro-mechanical problems this approach has been automated [55]. Some problems can be seen with this method. Especially for coupled problems, modal eigenfunctions are not readily available. In the case that the mechanical domain couples with others (fluidic, electrostatic etc.), it is attractive to use a modal analysis of the un-coupled mechanical sub-problem [56]. This should work well if the coupled problem is dominated by the mechanical structural and inertial forces, i.e. the coupling to the other domains is only weak. If, however, the coupling forces (fluidic damping or electrostatic attraction) are as strong as or even stronger than the inertial ones, the actual structural deflection shape would differ significantly from any mode shape, thus requiring a long series of modal eigenfunctions to approximate it. The efficiency of the resulting model would be low.

Another way of model order reduction is presented now, which tries to apply the methods as well as the software of another discipline to the field of compact modeling. That discipline is statistical modeling. The parameters of many devices are measured. It turns out that, due to the underlying physics, not all of those parameters vary independently from each other. A Principal Components Analysis (PCA) can be used to significantly reduce the dimensionality of the parameter space. In the field of Integrated Circuit device modeling this method is well established and software tools are available.

3.3.1 Pricipal components analysis for model order reduction

It is obvious that the variations of different state variables of a system with time or due to the change of a control parameter are not independent from each other, but are more or less correlated to each other. This directly leads to the idea to use Principal Components Analysis (PCA) to find a small set of components or factors which can be used to express the variations of all state variables. That gives a reduction of the problem size from the number of state variables to the number of components found by the PCA. This approach is very similar to the Karhunen-Loeve decomposition chosen by Hung [57, 58], but has the advantage that powerful software tools for PCA are commercially available. The PCA-tool SPAYN [59], originally designed for statistical analysis of Spice-parameters, is used in this work.

The sequence of necessary steps for developing a compact model by means of PCA is

outlined now.

a) Quasi-static models

Run a variety of FEM simulations: The relevant control parameters are varied in the desired range to provide the data for the subsequent PCA. All relevant FEM model degree of freedom for all simulated operating points must be stored in a database. This step requires a lot of hardware resources, namely CPU-time and disk space.

Physical analysis of a simplified model system: In order to get the qualitative relation between the control parameters and some variables, which can be used to describe the device behavior, a simplified model system must be found and described analytically. In case of an electrostatically actuated pump membrane, e.g., the control parameters are the applied hydrostatic pressure and electrical voltage, whereas the variable of interest is the displaced volume. The simplified model system could be a rigid plate, suspended by linear springs and acting as an electrical plate capacitor. That would lead to a linear relation between pressure and volume, but to a parabolic relation between volume and applied voltage.

Transform the control parameters: Corresponding to the results of the physical analysis, control parameters and FEM model degree of freedom should be transformed in such a way that the transformed variables exhibit linear correlations, at least in the simplified model system.

Run the PCA: All FEM model degree of freedom and all control parameters are just equally weighted input data to the PCA. Setting weight factors to the input data can add previously gained physical knowledge to the mathematical formalism. The PCA yields a distinct number of factors, which are necessary to reproduce the variations in the data of the FEM simulations of all operating points within a given accuracy. All degree of freedom in the data and the control parameters are correlated linearly to their corresponding factors. Higher order terms and mixed terms can be used in the correlations as well.

Change from factor representation to dominant parameters: To make the results of the PCA physically more transparent, it is possible to use the dominant parameters instead of the factors. The dominant parameters are those which have the strongest correlation to a factor, and they are automatically identified by the PCA-tool. Alternatively they can be chosen manually. That is recommended and can be guided by the results of the previously performed physical analysis. The control parameters which have been varied during the FEM simulations should be used as dominant parameters in any case.

The result of the described sequence of steps is a quasi-static CM, that contains very few degree of freedom and therefore can be simulated very efficiently. Most steps of the model generation can be automated. If one omits all steps which require user interaction, i.e. does not perform parameter transformations and does not apply any weight factors, the model generation can be fully automated. However, the loss of physical model content that comes along with this, causes reduced extrapolation capabilities of the resulting CM.

One major drawback of CM generation by means of PCA is, that in case of discontinuous or non-monotonic relations between control parameters and FEM model degree of freedom, this method will not yield a reasonable CM.

b) Dynamic models

The just described method of developing quasi-static CMs by means of PCA can be extended to develop CMs for dynamic modeling. The new aspects will be outlined now.

Run transient FEM-simulations: The dynamic response of the device to changes in control parameters is simulated. The transient behavior must be sampled, storing the vector of all important model degree of freedom for each time point into a database for the subsequent PCA.

Physical analysis of a simplified model system: The dynamic behavior of the device under consideration must be described by ODEs in terms of very few variables. The idea is to simplify the model to such an extend that an analytical description can be found.

Run the PCA: The time-variable must be excluded from the PCA. Besides this the analysis runs very similar to the quasi-static case, yielding a set of factors, which describe the variation of the data.

Change from factor representation to dominant parameters: The dominant parameter in each factor can be found automatically by the PCA-tool. A manual selection might be necessary, because either the factors or their dominant parameters must have a correspondence to the variables of the analytical model of the simplified system.

Describe the dynamic behavior: ODEs must be found which describe the dynamic behavior of the factors or their dominant parameters. Therefore a correspondence to the variables of the analytical model is required. Then the ODEs of this analytical model can be used. The parameters of those ODEs (like resonance frequencies or damping parameters, e.g.) can be extracted from the transient FEM data.

The deviation of the differential equations for the factors is difficult and requires insight into the dynamic behavior of the device. It is the key step in the development of dynamic CMs. The other steps can be automated. As in the quasi-static case, discontinuous device characteristics cannot be modeled by this method.

3.3.2 Quasi-static example: membrane

Electrostatically actuated membranes can be used as drive units in micro-pumps (see [60] and chapter 5.4). They can be manufactured relatively easy by surface or bulk micromachining technology [61], using only CMOS-compatible materials, and they have no static power consumption. Other actuation principles require additional materials, like piezo-ceramics, e.g., or consume a significant amount of power (thermo-pneumatic drives, e.g.). The disadvantage of an electrostatic drive is the very high required drive voltage and still limited achievable stroke volume. The latter makes self-priming and bubble tolerant pumps for liquids nearly impossible. Still the electrostatic pump membrane exhibits a very interesting behavior like multiple snap effects and hysteresis in the static characteristics. This is the reason why it is an attractive benchmark example for compact modeling.

The previously outlined method of developing a quasi-static CM by means of PCA will be exemplified now by modeling an electrostatically deflected membrane. It will be shown that the CM can be obtained easily and that this method is best suited for automatization,

but has very limited extrapolation capabilities and cannot handle discontinuities in the device characteristics. To handle those problems, physically based analytical modeling is a powerful, though elaborative approach and will be described in section 3.4.

a) Operation principle

A thin membrane, some micrometers thick and with lateral dimensions of approximately a millimeter, is separated from a rigid substrate by an air-gap of some micrometers width. Membrane and substrate are electrically isolated from each other, so that an electrical voltage can be applied between them (see section 3.4.2 for more details and a schematic drawing). Additionally, a hydrostatic pressure difference between air-gap and surrounding medium (air or water in a pump chamber, e.g.) acts on the membrane. The device characteristics of interest is the volume displacement as a function of pressure and applied voltage.

To maximize the volume displacement, which corresponds to the achievable stroke in an application as pump membrane, the voltage is chosen high enough to pull the membrane towards the substrate counter-electrode. This electrostatic pull-in is a discontinuity in the quasi-static device characteristics which is inherent to many MEMS.

b) PCA and CM generation

To generate the data that describes the device operation, a series of coupled electrostatic-mechanical FEM-simulations had to be performed, varying the control parameters pressure and voltage in a wide range. The FEM analysis yields the deflection of the membrane towards the substrate at all FEM-nodes for each data point. The displaced volume can be calculated by integrating the deflection over the membrane area. The nodal deflections together with the control parameters pressure p and voltage V are stored in a database.

A simplified model of the electrostatically actuated membrane was derived next. It is well known, that for small deflections and constant pressure load the membrane deflection depends linearly on the applied pressure. Due to the large aspect ratio between air gap and lateral membrane dimensions, for small deflections w the electric field between membrane and substrate can be assumed to be homogeneous. The electrostatic force between them can therefore be approximated using the formula for the electrostatic pressure load between parallel plates:

$$p_{el} = \epsilon \cdot V^2/(d_{gap} - w)^2 \ . \tag{3.5}$$

That leads to the idea to use V^2 instead of V in the PCA.

A software tool had to be developed to convert the output data format of the FEM-tool into the input data format of the PCA-tool. The PCA can then be performed and gives the result that two factors are necessary to express more than 99% of all variations in the FEM-data. Pressure p and transformed voltage V^2 are found to be the dominant parameters of factor one and two, respectively. Shown below are the results of the PCA, namely the nodal displacements dz_i as a function of the dominant parameters. Here, only linear terms are used for the correlations, but as shown in figures 3.14 to 3.16, higher order terms can be used for increased accuracy.

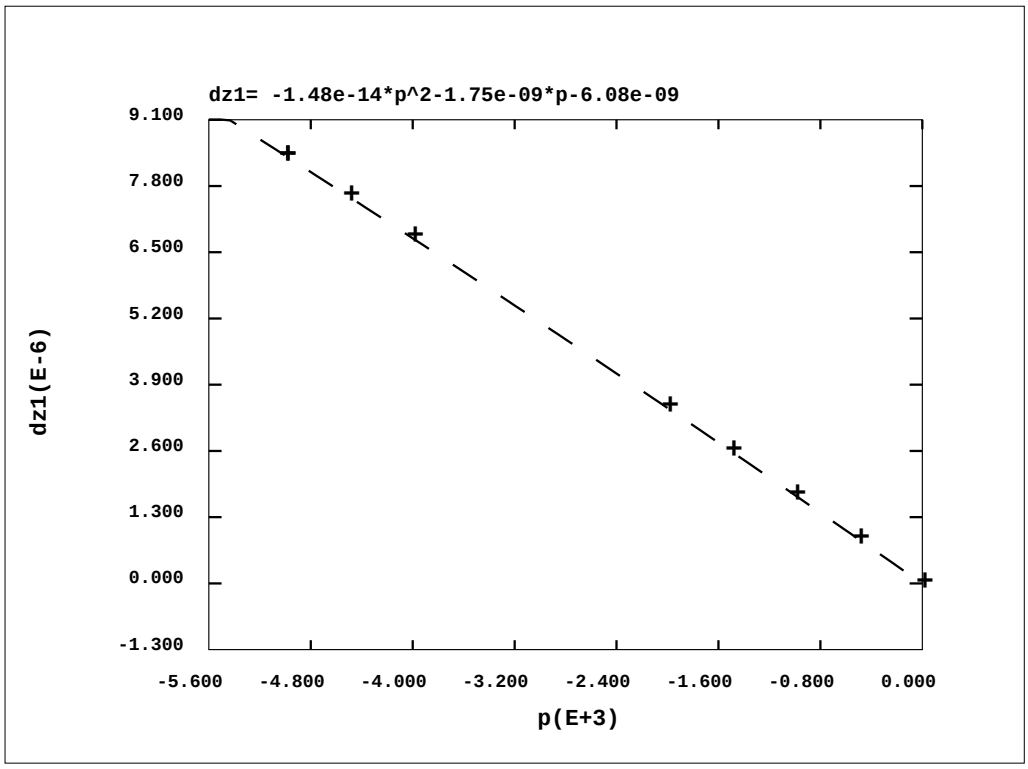

Fig. 3.14: Second order polynomial fit between applied pressure and membrane center displacement (node 1 in the FEM net).

```
p = $1

sqr(V) = $2

dz1 = 1.468e-06 - 1.842e-09*($1 + 1.000e+03) - 2.076e-10*($2 - 1.308e+03)
dz2 = 1.460e-06 - 1.833e-09*($1 + 1.000e+03) - 2.066e-10*($2 - 1.308e+03)
dz3 = 1.438e-06 - 1.805e-09*($1 + 1.000e+03) - 2.035e-10*($2 - 1.308e+03)
                                .
                                .
                                .
```

A part of the final CM, written in SpectreHDL, is shown below. Here, second order terms and mixed terms of the two dominant parameters p and V^2 are used to model the displacements dz_i. The displaced volume vol appears as an internal variable (called node) in the model. The terminal through variable, i.e. the volume flow rate W is calculated as the time derivative of vol. The electrical displacement current due to changes in the applied voltage or varying electrical capacitance is modeled as well, using the nodal displacements and a local plate capacitor approximation.

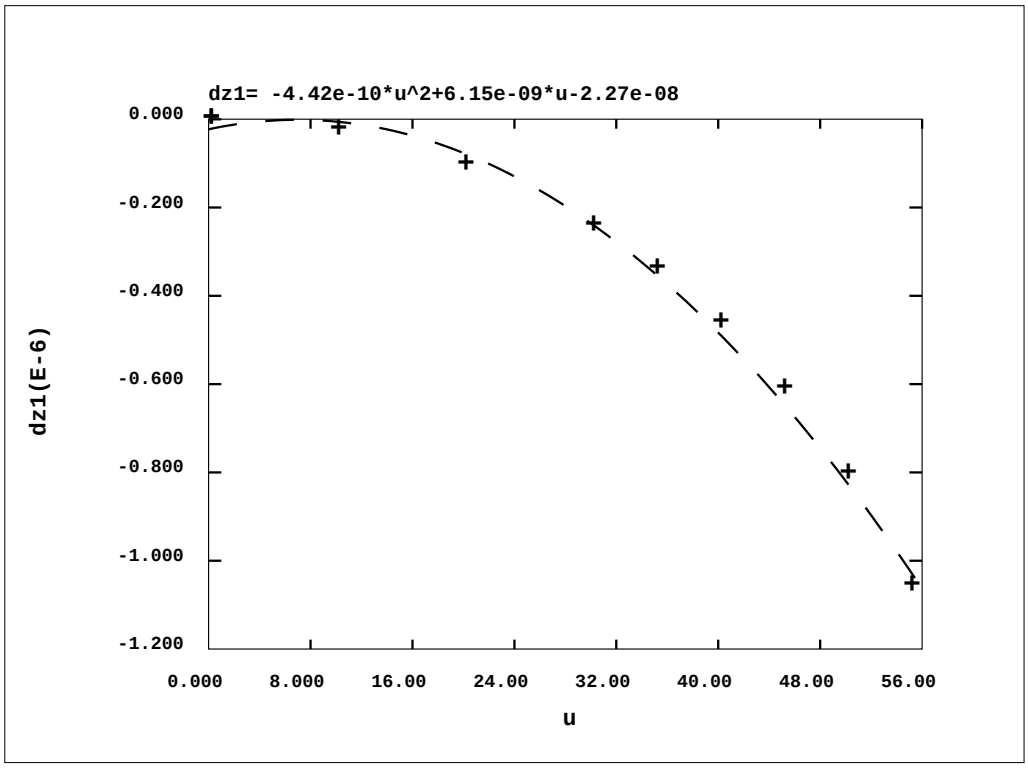

Fig. 3.15: Second order polynomial fit between applied voltage and membrane center displacement.

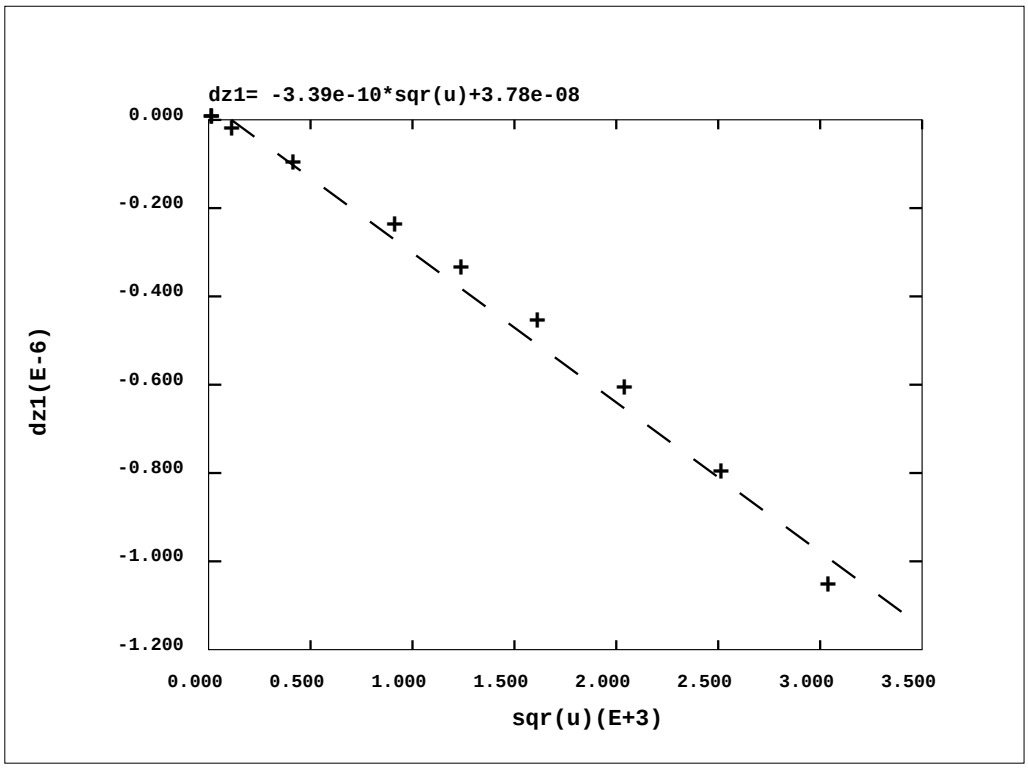

Fig. 3.16: Linear fit between the square of the applied voltage and membrane center displacement.

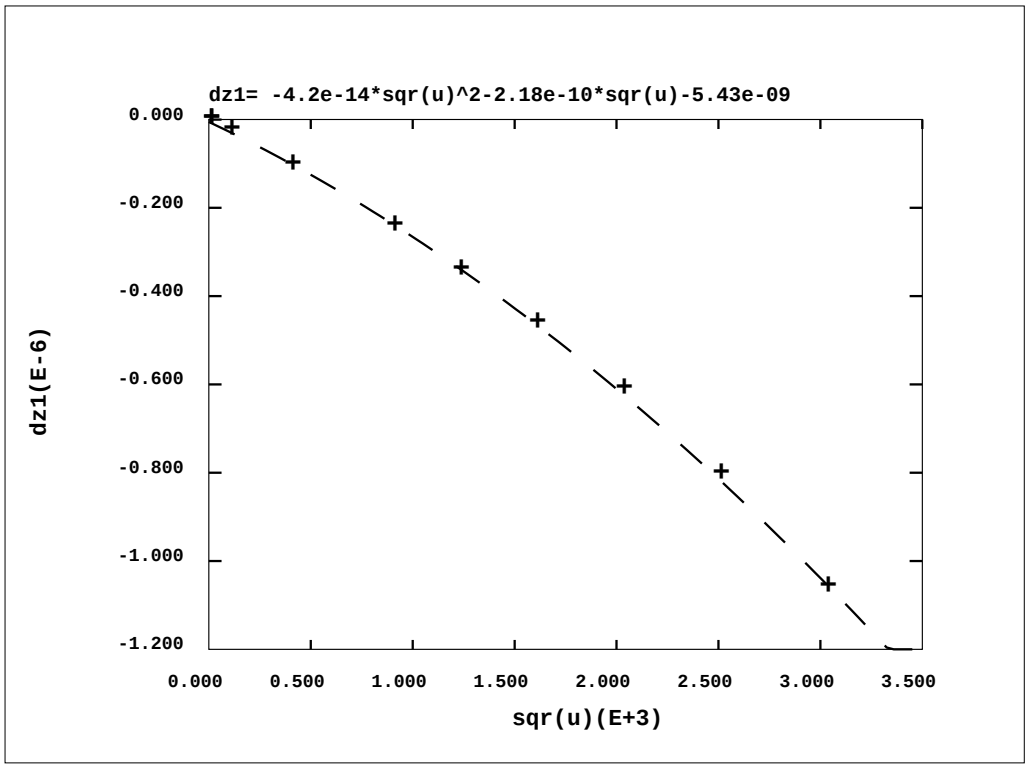

Fig. 3.17: Second order polynomial fit between the square of the applied voltage and membrane center displacement.

```
// Membrane Model
// P.Voigt

module membran (v_in, v_gnd, p_in, p_gnd) (d0, dox, lmembran, wmembran)
node[V,I] v_in, v_gnd;
node[P,W] p_in, p_gnd;       // unit: bar,  ml/min
parameter real d0       = 5.0e-6;  // membrane gap, unit: m
parameter real dox      = 2.0e-6;  // isolation oxide thickness
parameter real lmembran = 5.0e-3/2.0;  // membrane edge length
parameter real wmembran = 0.1e-3;  // membrane edge width
{
    real c0 = eps0*lmembran*wmembran/d0 / 20.0;
    real p, u, uu, c,
         dz1,  dz2,  dz3,  dz4,  dz5,  dz6,  dz7,  dz8,  dz9,  dz10,
         dz11, dz12, dz13, dz14, dz15, dz16, dz17, dz18, dz19, dz20;
    node [M,U] vol;         // displaced volume, unit: nl
//  Model parameters, to be set in a model file (or during instantiation)
    parameter real epsox    = 3.9;

    analog {
u  = V(v_in, v_gnd);         // input voltage
uu = u*u;
p  = 1.0e+5*P(p_in, p_gnd);  // input pressure

dz1  = 1.511e-06 - 1.824e-09*(p + 1.000e+03) - 1.800e-10*(uu - 1.308e+03)
 - 9.911e-14*(p + 1.000e+03)*(uu - 1.308e+03) - 5.650e-14*(p + 1.000e+03)^2
  - 1.487e-14*(uu - 1.308e+03)^2 - 4.774e-17*(p + 1.000e+03)^2*(uu - 1.308e+03)
   - 1.793e-17*(uu - 1.308e+03)^2*(p + 1.000e+03);
                              .
                              .
                              .
```

```
.
.
.
dz20  = 1.359e-08 - 1.646e-11*(p + 1.000e+03) - 1.693e-12*(uu - 1.308e+03)
 - 8.120e-16*(p + 1.000e+03)*(uu - 1.308e+03) - 4.334e-16*(p + 1.000e+03)^2
 - 1.205e-16*(uu - 1.308e+03)^2 - 3.770e-19*(p + 1.000e+03)^2*(uu - 1.308e+03)
 - 1.426e-19*(uu - 1.308e+03)^2*(p + 1.000e+03) ;

M(vol) <- -1.0e+12*4.0*wmembran*lmembran*(
          0.5*dz1+ dz2+ dz3+ dz4+ dz5+ dz6+ dz7+ dz8+ dz9+ dz10
              + dz11+dz12+dz13+dz14+dz15+dz16+dz17+dz18+dz19+dz20)/20.0;

W(p_in, p_gnd) <- 1.0e-6*60.0*dot(M(vol));  // unit: ml/min

        c = c0 / (1.0+dz1/d0) + ... + c0 / (1.0+dz20/d0);

I(v_in, v_gnd) <- dot(c*u);
    }
}
```

c) Simulation results

On the left hand side of figure 3.18, the CM simulation results are compared to the FEM-simulations, using the same range of data which was used for the PCA ($-2kPa$ to $0kPa$ and $0V$ to $50V$). As expected, the CM matches the FEM perfectly well. The extrapolation outside this pressure range gives fairly poor results however. That is not only the case in the pressure range above $0kPa$, where the device characteristics are discontinuous (see chapter 3.4.2 below for a detailed explanation of this effect), but also below $-2kPa$, as can be seen in the right part of Fig. 3.18 and in the left of Fig. 3.19. Using a larger pressure range for the PCA ($-4kPa$ to $0kPa$) would extend the accurate modeling range (right part of Fig. 3.19), but still the model cannot be used to extrapolate outside the range used by the PCA to fit the correlations.

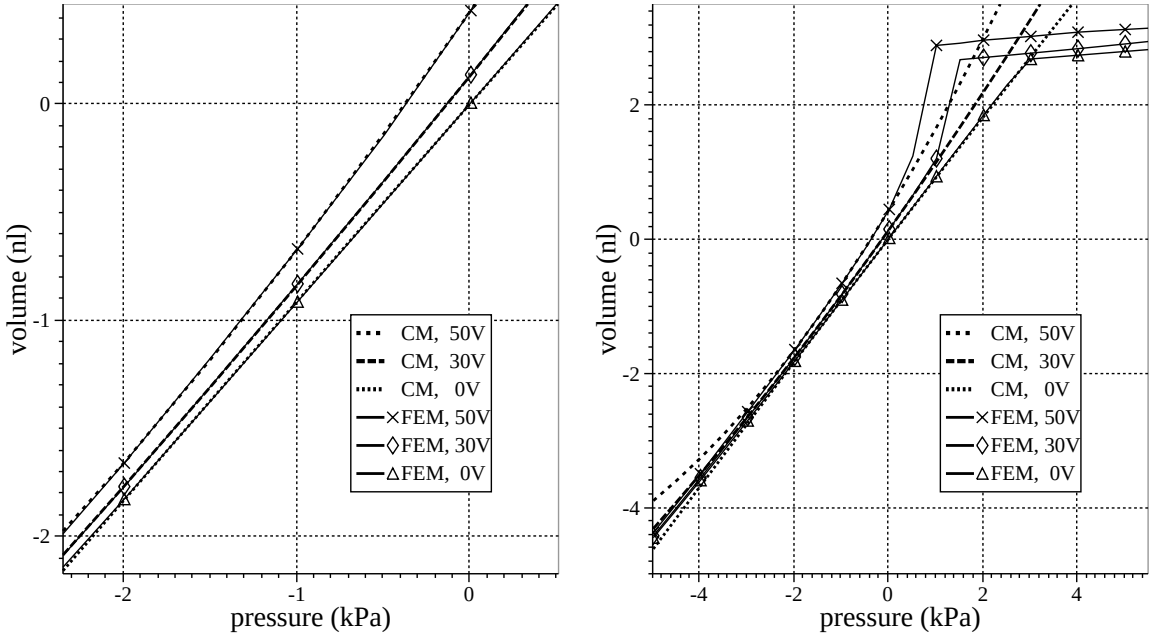

Fig. 3.18: Displaced volume versus applied pressure, comparing FEM and CM data. Left: pressure range from -2kPa to 0kPa was used in the PCA to generate the CM. Right: extrapolation of the CM fails outside the pressure range, which was used in the PCA.

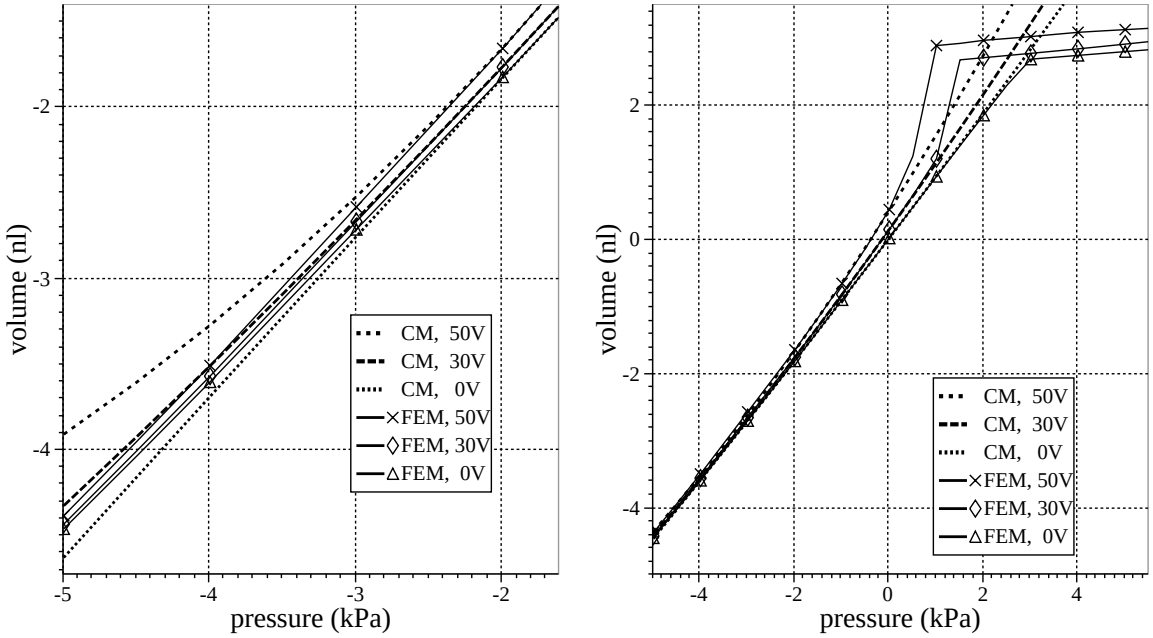

Fig. 3.19: Displaced volume versus applied pressure, comparing FEM and CM data. Left: extrapolation fails outside the pressure range used for the PCA. Right: extended pressure range down to -4kPa was used for the PCA.

Only if by means of a physical analysis some information about the physical basis of the device behavior is incorporated into the model, it can be used for extrapolation. This is illustrated in Fig. 3.20: on the left hand side, an extrapolation outside the voltage range

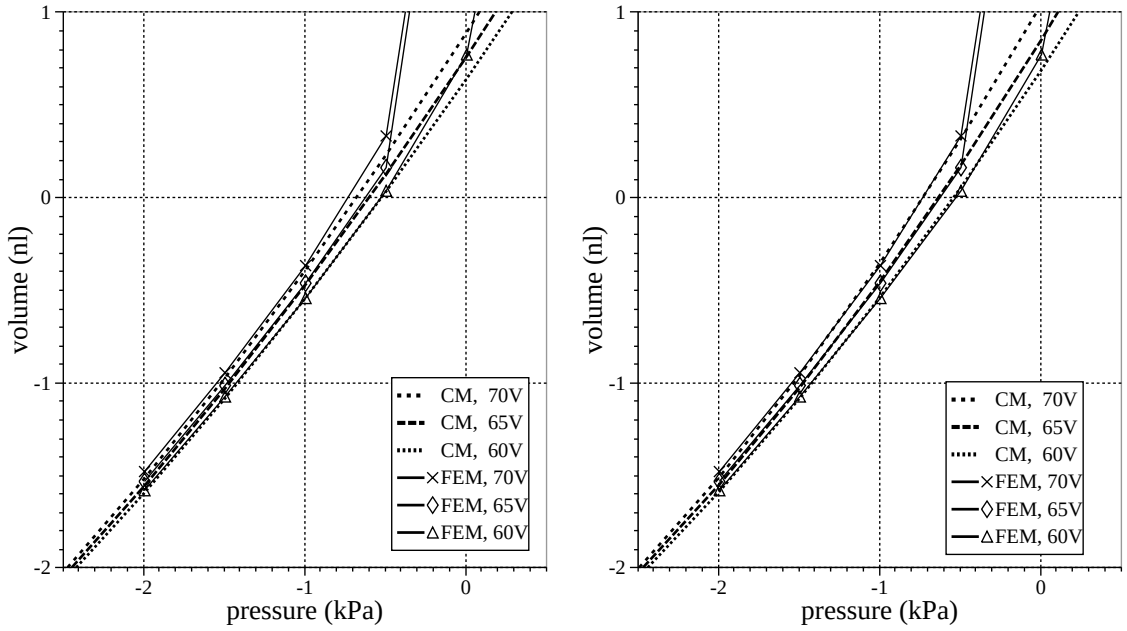

Fig. 3.20: Displaced volume versus applied pressure, comparing FEM and CM data. The applied voltages are above those used for the PCA. Left: untransformed voltage used in the PCA. Right: quadratic transformation was used in the PCA.

used for the PCA was performed, using the non-transformed voltage in the PCA. On the right of this figure, however, the transformed voltage u^2 was used instead, thus using previously acquired knowledge about the device behavior. The extrapolation capabilities of this model are significantly better, although the discontinuous behavior, namely the pull-in effect, still cannot be modeled.

3.3.3 Dynamic model example: acceleration sensor

To demonstrate the generation of a dynamic CM using PCA, the thermal self-test of an acceleration sensor is used. This sensor and its dynamic behavior was already described in section 3.2.

a) Dynamic FEM model and PCA

To study the dynamic properties of a system, its response to steplike changes of input stimuli can be analyzed. In the given case of the acceleration sensor the response to a steplike change of the heating current through the resistors located on the suspension beams is analyzed. To this end, a coupled thermo-mechanical FEM-simulation was performed. The heat generation in the resistors was applied to the FEM-model as a constant load (heat generation rate Q_p), thus neglecting the dependence of the piezoresistors conductivity on the temperature.

The results of the FEM-simulation are sampled in a time-interval from zero to two milliseconds after the heating current was applied. The solution vector for each time-point

was stored in a database. The PCA, which was performed on this data, gave the result that the variation in the data can be expressed using three independent factors. The dominant parameters in those factors are the displacement $u8$ and the temperature $T14$ of nodes located in the middle of the suspension beams, and the temperature $T17$ at a node in the center of the seismic mass. The dynamic response of those dominant parameters to a stepl-like increase in the heating power is plotted in the left of figures 3.21 and 3.22.

All other nodal degree of freedom can be expressed by these dominant parameters. When only linear terms are used, then 95% of the data variation is modeled. By adding quadratic and mixed terms this value is increased to more than 99%.

```
u8  = $1

T14 = $2

T17 = $3

u1 = -3.419e-10  + 1.574e+00*($1 - 1.896e-11)
                 - 8.186e-11*($2 - 5.939e+00)
                 - 2.900e-10*($3 - 3.310e-02)
u3 = -2.450e-10  + 1.545e+00*($1 - 1.896e-11)
                 - 5.934e-11*($2 - 5.939e+00)
                 - 2.074e-10*($3 - 3.310e-02)
u4 = -1.676e-10  + 1.483e+00*($1 - 1.896e-11)
                 - 4.112e-11*($2 - 5.939e+00)
                 - 1.391e-10*($3 - 3.310e-02)
                           .
                           .
                           .
T1 =  1.589e+00  + 9.339e+07*($1 - 1.896e-11)
                 + 3.091e-01*($2 - 5.939e+00)
                 + 1.586e+00*($3 - 3.310e-02)
T3 =  3.807e+00  + 7.777e+07*($1 - 1.896e-11)
                 + 6.559e-01*($2 - 5.939e+00)
                 + 1.277e+00*($3 - 3.310e-02)
T4 =  5.816e+00  + 5.399e+07*($1 - 1.896e-11)
                 + 9.656e-01*($2 - 5.939e+00)
                 + 1.094e+00*($3 - 3.310e-02)
                           .
                           .
                           .                                $
```

b) Dynamic model for the factors

The type of the dominant parameters, their location and their dynamic response calculated in the FEM make it possible to identify physical effects which determine their dynamic behavior. The parameters $T14$ and $T17$ show the typical behavior of two systems with thermal resistivity and capacitance, which are coupled through a common boundary. That can be described by two coupled ordinary differential equations of first order (eqns. (3.6), (3.7)). The coefficients of this set of equations can be easily extracted from

the FEM data.

$$c_{w1} \cdot \dot{T}_{14} + r_{w1} \cdot T_{14} = -f_c \cdot T_{17} + Q_p \quad (3.6)$$

$$c_{w2} \cdot \dot{T}_{17} + r_{w2} \cdot T_{17} = -f_r \cdot T_{14} \quad (3.7)$$

The parameter $u8$ can obviously be described by the differential equation of a damped harmonic oscillator (eqn. (3.8)). Important for the resulting model is the fact that both other dominant parameters $T14$ and $T17$ appear in the force term of this differential equation, motivated by the fact, that a temperature increase of the beams and the seismic mass causes their thermal expansion and, subsequently, a mechanical deflection. The oscillation frequency can either be determined analytically, calculating the size of the seismic mass and using formulae for beam bending to describe the suspension beams, or can be extracted from FEM data.

$$m \cdot \ddot{u}_8 + d \cdot \dot{u}_8 + k \cdot u_8 = f_v \cdot T_{14} + f_u \cdot T_{17} + f_p \cdot \dot{Q}_p \quad (3.8)$$

Since the damping of the sensor due to air friction was not modeled in the FEM, but just mimicked using structural damping, a simple fit of the damping parameter is sufficient. The parameters in the force term, which actually describe the coupling between the thermal and the mechanical problems, have been extracted from the FEM data as well.

The resulting CM, written in SpectreHDL, is shown here:

```
// acceleration sensor: thermo-mechanical CM based on PCA
// P.Voigt

module mafethe (n_th1, n_th2, n_mech) ()
node[T,Qp] n_th1, n_th2;
node[X,F] n_mech;
{
    node [X, F] u8, u8p;
    node [T,Qp] T14, T17;
//Model parameters, to be set in a model file (or during instantiation)
    parameter real k    = 1.0e3;      // spring constant
    parameter real d    = 2.0e-3;     // damping constant
    parameter real m    = 0.365e-6;   // seismic mass
    parameter real fitp = -0.45e-9;
    parameter real fitu = -1.36e-6;
    parameter real fitv = 2.0e-9;
    parameter real fitc = -0.11e-3;
    parameter real fitr = -0.54e-3;
    parameter real rw1  = 1.9*1.9e-3/6.24;// beam: thermal cond.
    parameter real cw1  = 0.05e-6;        // beam: thermal cap.
    parameter real rw2  = 0.29e-3;        // mass: thermal cond.
    parameter real cw2  = 0.12e-3;        // mass: thermal cap.
    analog {
F(u8)   <- fitp * 0.25 *dot(Qp(n_th1)+Qp(n_th2));
F(u8)   <- fitu * T(T17);
F(u8)   <- fitv * T(T14);
F(u8)   <- k    * X(u8);
X(u8p)  <- dot(X(u8));
F(u8)   <- d    * dot(X(u8));
F(u8)   <- m    * dot(X(u8p));
```

```
Qp(T14) <- -0.25 * (Qp(n_th1)+Qp(n_th2));
Qp(T14) <- fitc * T(T17);
Qp(T14) <- rw1 * T(T14);
Qp(T14) <- cw1 * dot(T(T14));

Qp(T17) <- fitr * T(T14);
Qp(T17) <- rw2 * T(T17);
Qp(T17) <- cw2 * dot(T(T17));

//T4  - position of heating resistor 1
T(n_th1)  <-  9.656e-01*T(T14) + 1.094*T(T17);
//T15 - position of heating resistor 2
T(n_th2)  <-  7.970e-01*T(T14) - 0.030*T(T17);
//u17 - center of seismic mass
X(n_mech) <- -1.1e-10*T(T14) + 1.556e+00*X(u8) - 2.0e-10*T(T17);
    }
}
```

The device terminal nodes n_{th1} and n_{th2} are representing the thermal properties of the piezoresistors. Here, the Joule heating, generated in the piezoresistors, is forced into the compact model, and the temperature at this node is fed back to the electrical model of the piezoresistor to account for the temperature dependence of the conductivity. The device terminal node n_{mech} represents the mechanical state of the seismic mass. It is used to couple the mechanical deflection into the electrical model of the piezoresistor to account for the stress dependence of the conductivity.

c) Simulation results

The CM was used to simulate the response of the sensor to a steplike change in heating power and to a heating pulse of 1ms duration. The results are compared to coupled thermo-mechanical FEM-simulations. As can be seen in figures 3.21 and 3.22, the FEM results are matched very well. The required CPU-time is only a few seconds compared to some hours for the FEM.

The PCA-based CM reaches the same accuracy as the FN model described in section 3.2. A comparison is given in figures 3.23 to 3.25. The numerical efficiency, however, is much better. The PCA-based CM is at least an order of magnitude faster than FN-models, depending on the actual number of grid nodes in the FN model.

Because the simulations with PCA-generated compact models run very efficiently, compared to FEM simulations or FNM simulations, presented in section 3.2, also detailed simulations covering a long time-span can be performed, taking only a few seconds of CPU-time. In Fig. 3.24 and 3.25 the device response to a long series of heating pulses is shown. It turns out that the beams heat up and cool down very quickly, causing mechanical oscillations, whereas the seismic mass warms up very slowly, causing a slight shift in its mechanical equilibrium position.

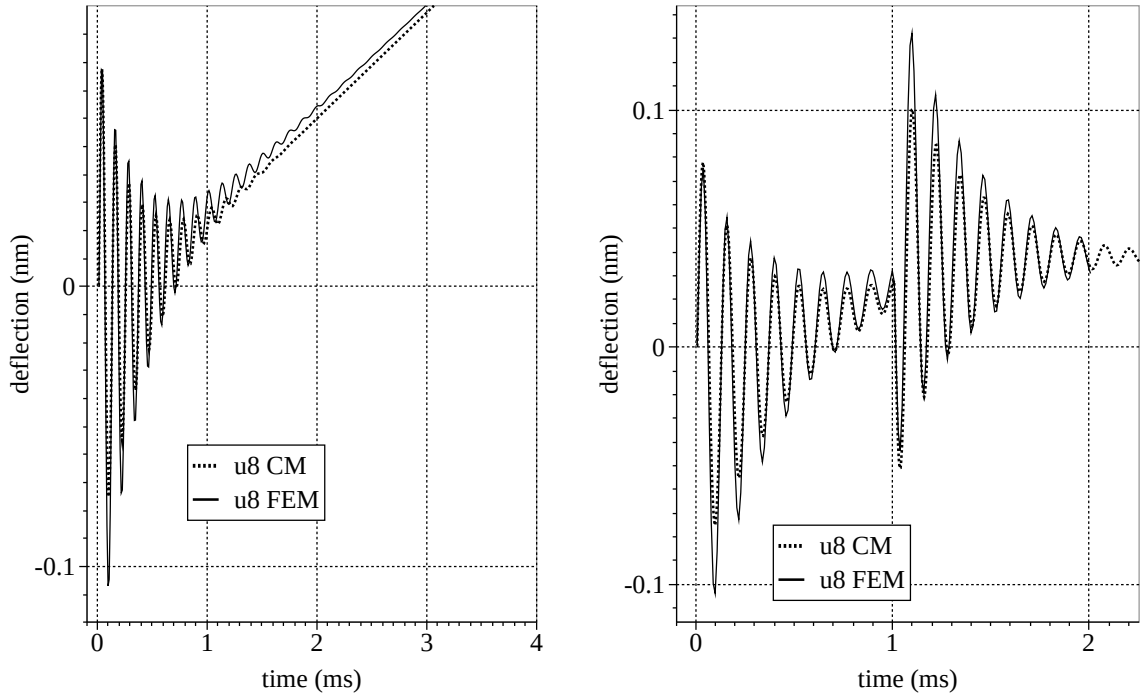

Fig. 3.21: Simulated transient response to a steplike (left) and pulsed (right) heat generation rate. The resulting dynamic behavior of the dominant parameter $u8$ is shown, comparing the PCA based CM against FEM-data.

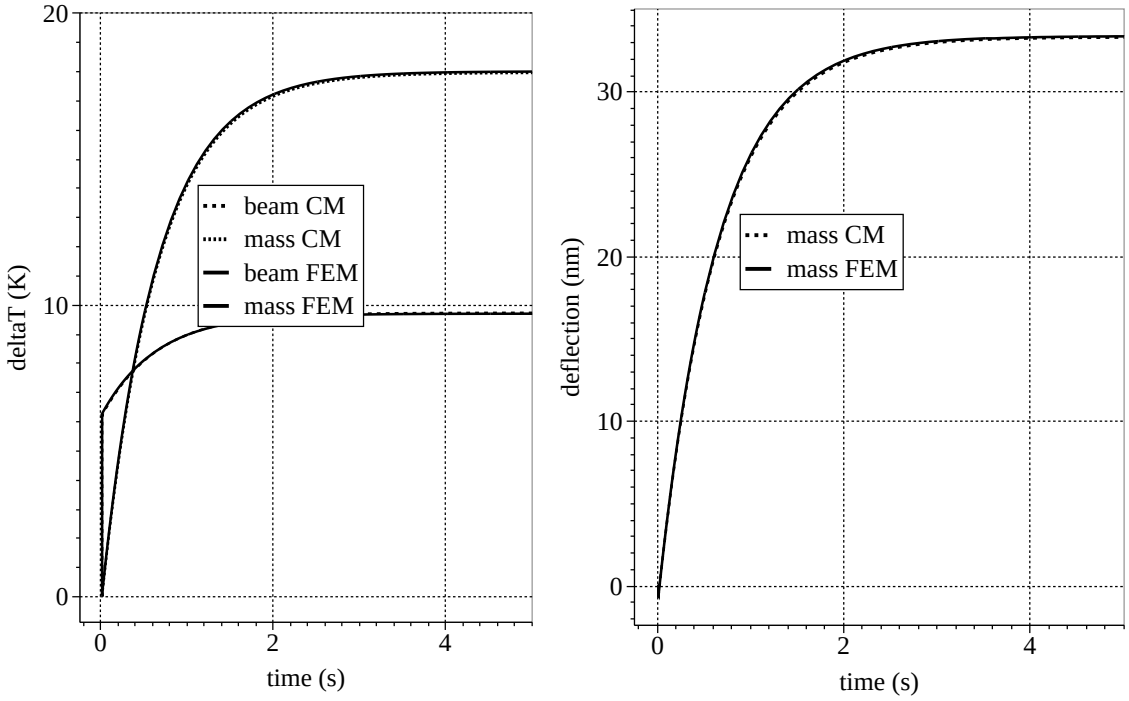

Fig. 3.22: Simulated transient response to a steplike heat generation rate. The temperature raise of the heated suspension beams ($T14$) and the seismic mass ($T17$) (left) and the resulting deflection of the seismic mass (right) is shown.

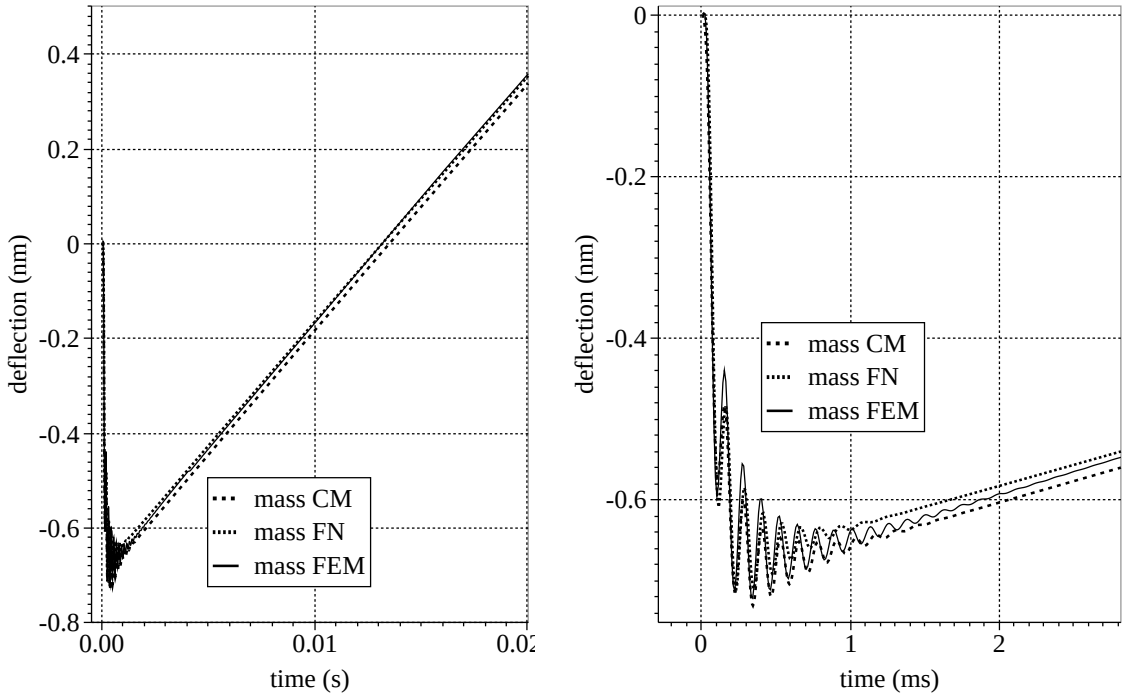

Fig. 3.23: Simulated transient response to a steplike heat generation rate. The resulting deflection of the seismic mass is shown, giving a detailed view on the right. A comparison of three different modeling approaches shows very good agreement between them.

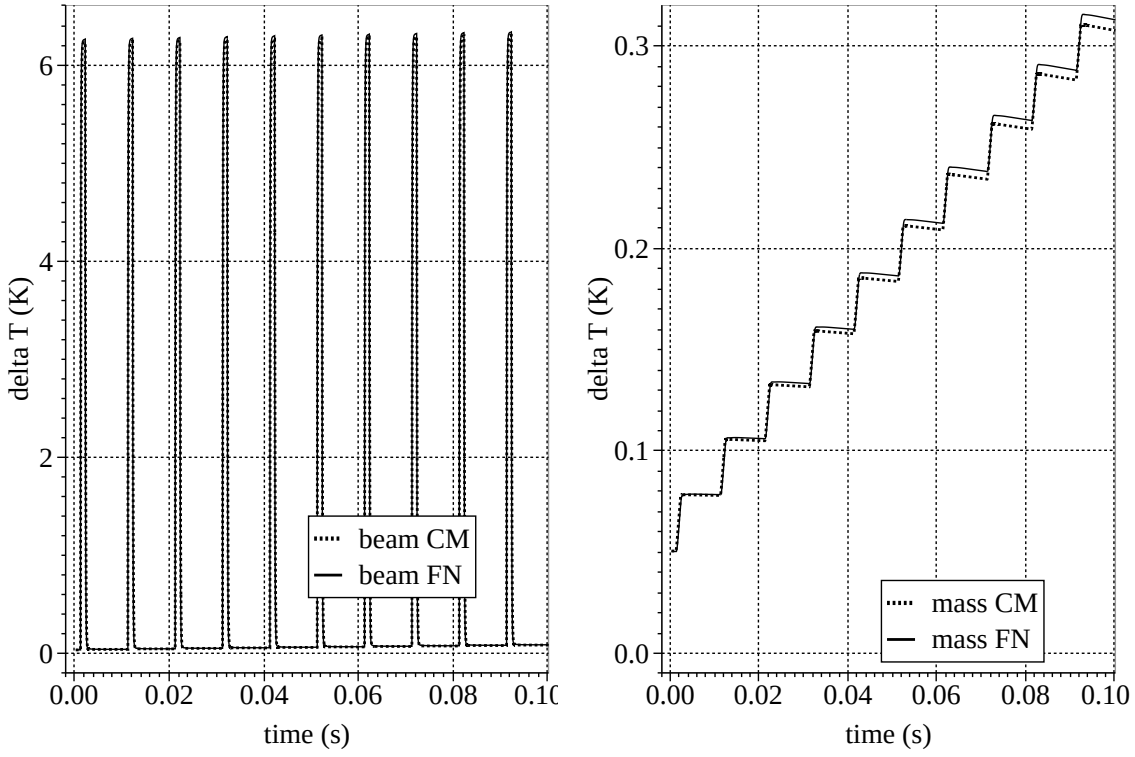

Fig. 3.24: Simulated transient response to a pulsed heat generation rate. The temperature raise of the heated suspension beam (left) follows the the heat generation rate, whereas the temperature of the seismic mass (right) remains nearly constant. The result of a FN model based simulation (see chapter 3.2) is compared to the PCA based CM.

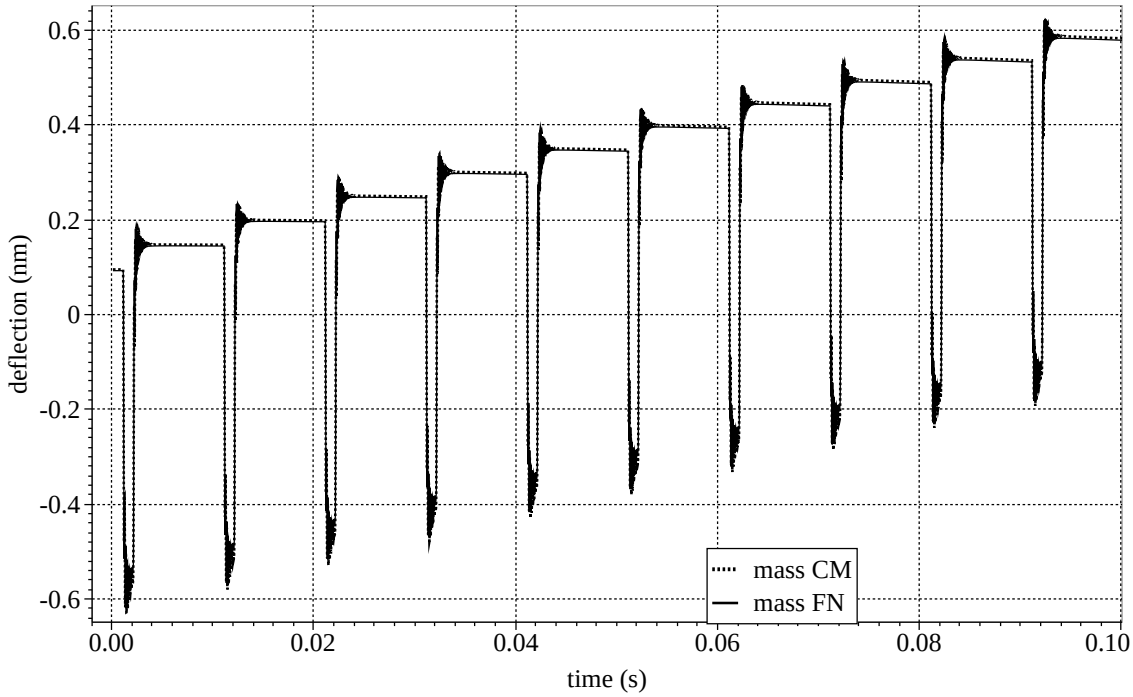

Fig. 3.25: Simulated transient response to a pulsed heat generation rate. The deflection of the seismic mass is caused by the temperature raise of both, the suspension beams and the seismic mass. The result of a FN model based simulation (see chapter 3.2) is compared to the PCA based CM.

3.4 Analytically derived models

As shown in the previous two sections, finite network modeling and modeling based on a basis-functions approach are useful modeling methods, but cannot address certain problems. They cannot be efficiently used to model design and process variations and they have very limited extrapolation capabilities. And finally, they can hardly be used for statistical modeling, yield analysis and related tasks. It will be shown next, that analytically derived, physically based models provide a means to efficiently address those questions.

3.4.1 Physically based models

For statistical modeling, yield analysis etc., the compact model must explicitly express all relevant physical effects, which determine the device behavior. A continuous field model for those physical effects can be used to determine a set of node variables, describing the interaction of the device with other devices of the system and the environment. If the method outlined in chapter 2 is followed, that yields a set of node variables that fulfill conservation laws, namely the node rule for the through variables and the mesh loop rule for the across variables, thus forming a GKN.

The final result of the model development process is a compact model that describes the dynamic device behavior in terms of a set of ODAEs. The number of internal state variables of the CM, which need to be iterated during the simulation of the model, must be as small as possible. The input parameters of the CM are design parameters and technology parameters. Examples are photo-mask dimensions, layer thicknesses and material parameters. Ideally, no fit parameters are used, but in most cases it will be necessary to simplify the real device, until an analytical description of the physical effect under consideration is possible. That means, that fit parameters might be necessary to compensate for the error made by the analytical approximations. Otherwise, the accuracy of the resulting model could be insufficient for the applications it is intended for.

It is important to mention here, that those fit parameters are not global fit parameters, but are related to a well understood approximation of a certain physical effect. That means that it is obvious on what data for what device operation conditions to extract those fit parameters. That allows to set up a local extraction strategy for the fit parameters.

Since the dependencies of the device behavior on device geometry, operating conditions, material and process parameters are contained in the model equations, the fit parameters should only weakly depend on them. If that is not truly the case, such a dependence was not explicitly modeled, but maybe overlooked and pushed into the fit parameters. That would mean that the device model needs to be improved to correctly model those effects. The resulting model has good extrapolation capabilities, as long as the range, wherein the analytical approximations are valid, is not left. The knowledge about this range is an essential part of the model itself.

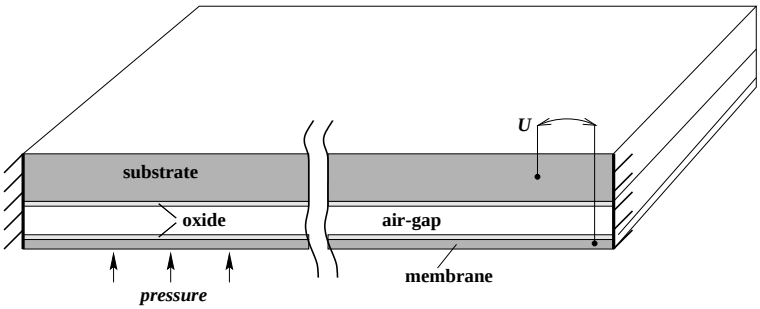

Fig. 3.26: Schematic view of an electrostatically actuated membrane as it can be used as pump membrane in micro-pumps.

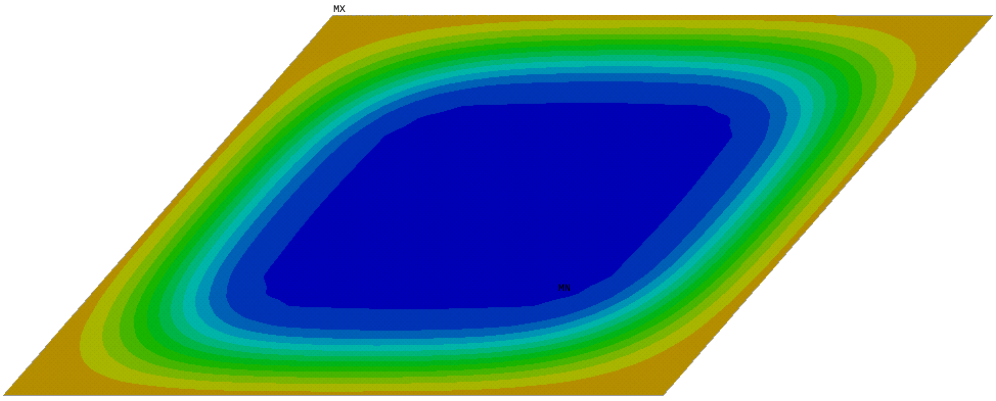

Fig. 3.27: FEM-simulated membrane deflection. A voltage of 150V is applied. It is possible to distinguish three regions: the approximately square shaped touch-down area (dark grey), the edges, and the corners.

3.4.2 Example: an electrostatically actuated pump membrane

Electrostatically actuated pump membranes typically consist of a flexible membrane-like top-electrode and a rigid bottom-electrode. When an electric voltage is applied between these electrodes, the electrostatic attracting force deflects the pump membrane. If the applied voltage is sufficiently high, the membrane snaps towards the counter-electrode, thus maximizing the achievable stroke volume [62]. To avoid an electrical shortage, the electrodes must be covered by isolating layers. The quasi-static characteristics of an electrostatically actuated membrane are presented in Fig. 3.28.

When a voltage is applied to the membrane, and additionally, an increasing hydrostatic pressure[1] moves the pump membrane towards the counter-electrode, then at a certain pressure and resulting membrane deflection the electrostatic attracting force overcomes the restoring mechanical force, thus pulling in the membrane. The bending shape of a pulled-in membrane is shown in Fig. 3.27. To release the membrane, a lower pressure is required, so that the pressure-controlled quasi-static characteristics exhibit a hysteresis (see left of Fig. 3.28).

[1] In the context of pump-membranes, pressure always means the pressure difference between both sides

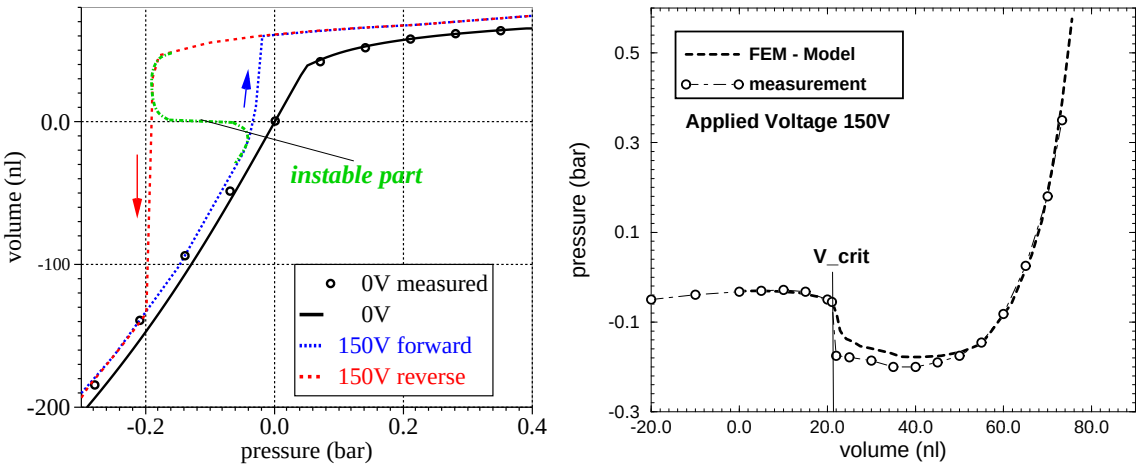

Fig. 3.28: FEM-simulated static characteristics of a membrane. The left figure shows the volume deflection vs. applied hydrostatic pressure. The right figure shows the resulting pressure, when the volume is the controlled parameter. A voltage of 150V is applied to the membrane, causing the snap effects.

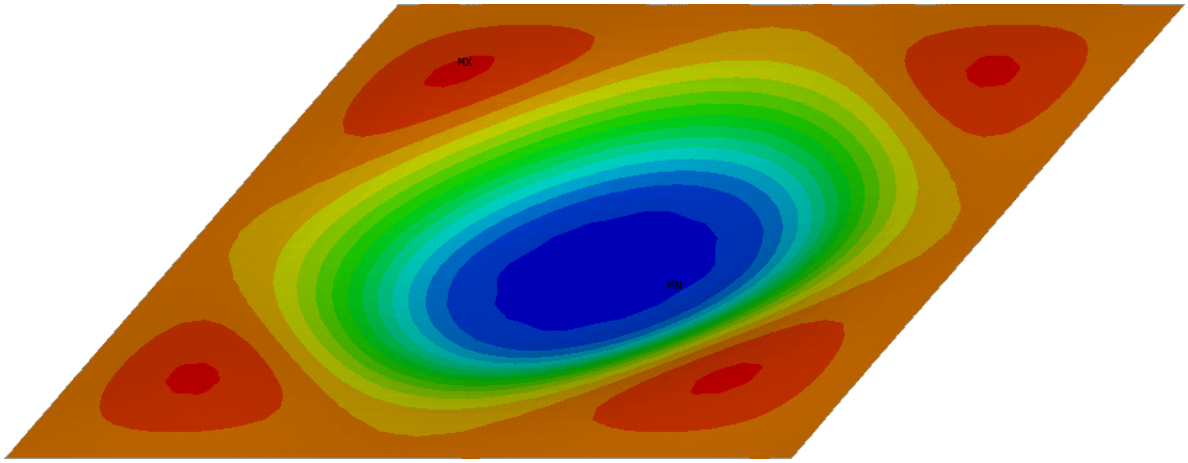

Fig. 3.29: FEM-simulated membrane deflection. A voltage of 150V is applied and the displaced volume is fixed to be 20nl, which is next to the shape snap point.

To access the instable part of the volume-versus-pressure characteristics, one has to change from pressure control to volume control (Fig. 3.28, right). These characteristics also show a discontinuity, caused by an abrupt change in the shape of the membrane deflection. A FEM-analysis reveals, that the shape snap effect appears to be a redistribution of displaced volume under the condition that the total displaced volume is constant. Figures 3.29 and 3.30 illustrate this effect. The volume redistribution is driven by the inhomogeneities of the electrostatic load.

The complexity of the membrane behavior is comparable to the breakdown phenomena of multi-layer CMOS structures. Fig. 3.31 shows the simulated latch-up of a lateral

of the membrane, i.e. between pump-chamber and air-gap.

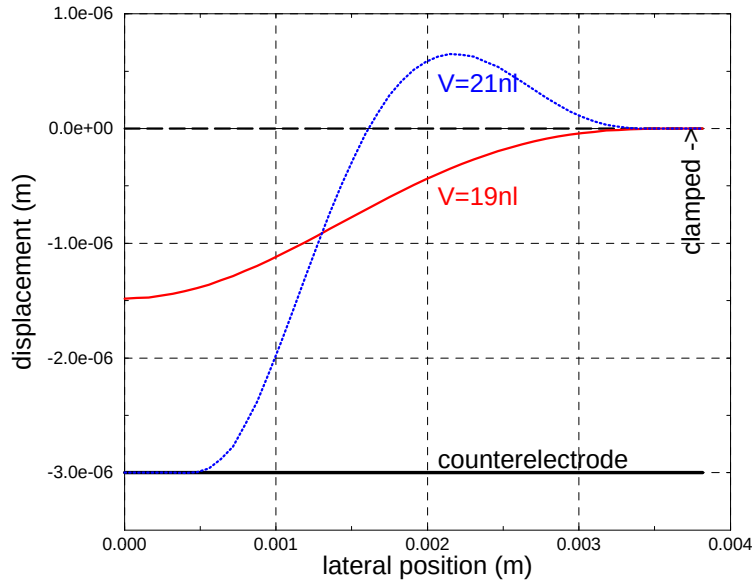

Fig. 3.30: FEM-simulated membrane deflection. A cutline diagonally from the center to a corner of the membrane is shown, immediately before (solid line) and after (dotted line) the shape snap occurs.

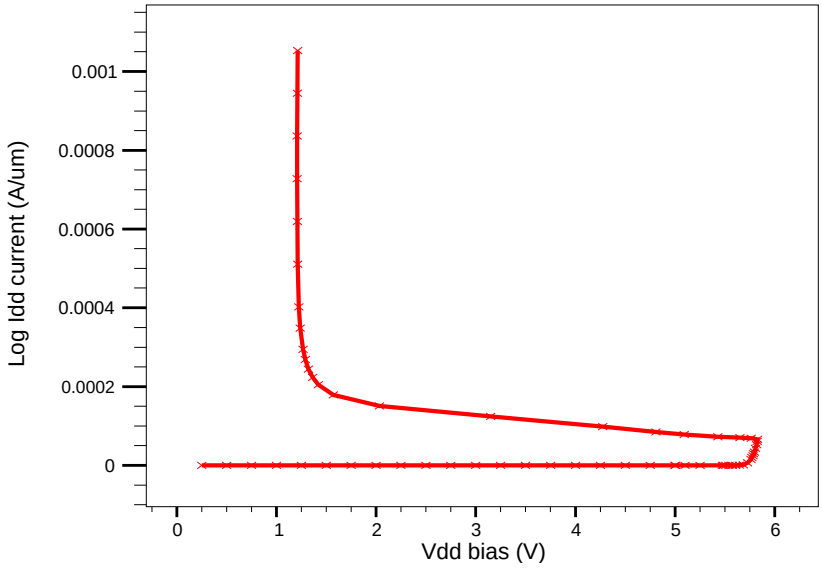

Fig. 3.31: Simulated latch-up of a lateral CMOS $n^+\,p\,n\,p^+$ structure. The second breakdown, when the voltage drops to a small value, has it's correspondence in the shape snapping of an electrostatically actuated membrane.

$n^+\,p\,n\,p^+$ structure [63], which is very similar to the quasi-static characteristics of a membrane. The latter is shown in Fig. 3.28. The right hand side of this figure shows the case that a hydrostatic pressure is the result of a controlled volume in presence of an applied voltage. In that case, the instable part of the pressure controlled characteristics, shown at the left of Fig. 3.28, can be accessed.

3.4.3 The compact model

To find a physically based compact model, that describes the behavior of the membrane, the status of the membrane must be described by analytical expressions in terms of as few as possible state variables. As a first step, the membrane deflection w caused by an applied hydrostatic pressure p is expressed analytically [48] by:

$$w_{max} = 0.00126 \frac{p \cdot l_{memb}^4}{D} \tag{3.9}$$

$$w(x,y) = w_{max} \cos(\frac{\pi \cdot x}{l_{memb}}) \cos(\frac{\pi \cdot y}{l_{memb}}) \tag{3.10}$$

$$D = \frac{E \cdot d_{memb}^3}{12 \cdot (1-\nu)} . \tag{3.11}$$

Here, l_{memb} and d_{memb} are edge length and thickness of the membrane, x and y are the distance from the membrane center point in the corresponding directions, whereas E and ν are modulus of elasticity and Poisson ratio, respectively. For large deflections, even though analytical descriptions are known [64, 65], a simple fit function is deliberately used to account for the resulting non-linearities. The corresponding fit parameter was extracted from comparison with FEM-simulations. This approach preserves high accuracy even in the region of large deflection (region of large negative pressure in Fig. 4.2).

As soon as the membrane touches the counter-electrode, another approximation comes to play. The membrane is considered to consist of three different kind of regions as sketched in Fig. 3.33. A comparison to the results of a FEM-simulation in Fig. 3.27 shows, that this approach is well justified. A comparable approach can be found in [66]. The touch-down region A_t is excluded from the force balance and therefore the areas A_p can be approximated by formulae from [48] for rectangular membranes with one edge much longer than the other (2D approximation):

$$w_{max} = 0.0026 \frac{p \cdot l_{eff}^4}{D} \tag{3.12}$$

$$w(x) = w_{max} \cos(\frac{\pi \cdot x}{l_{eff}}) . \tag{3.13}$$

The effective membrane length l_{eff} is the edge length of the membrane reduced by the edge length of the touch-down area A_t. The corner areas A_c are assumed to behave similar to one quarter of a square membrane with the edge length l_{eff}, modified by a fit factor.

As a result of these analytical expressions, the state of the membrane can be described by two variables, namely the center deflection w_{max} and the effective membrane length l_{eff}. For deflections smaller than the gap between membrane and counter-electrode, l_{eff} is constant, equal to the geometrical membrane length l_{memb}. When the membrane has snapped down and touches the counter-electrode, w_{max} stays constant while l_{eff} decreases with increasing pressure, following approximately a one over four power law, according to equation (3.12).

Once the bending shape of the membrane is known, the electrostatic attracting force between membrane and counter-electrode can be calculated as well as the corresponding electric capacitance. Due to the very large aspect ratio between lateral membrane dimensions l_{memb} and gap width d_{gap} the approximation of a homogeneous electric field is well

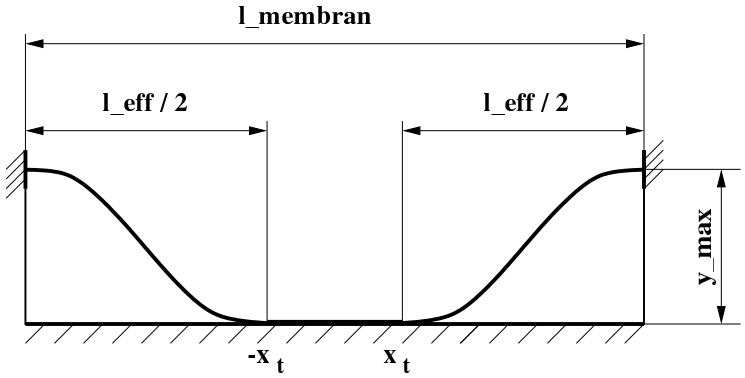

Fig. 3.32: Membrane deflection curve. The segment from $-x_t$ to x_t, touching the counter-electrode, is excluded from the force balance, thus reducing the effective membrane length to l_{eff}.

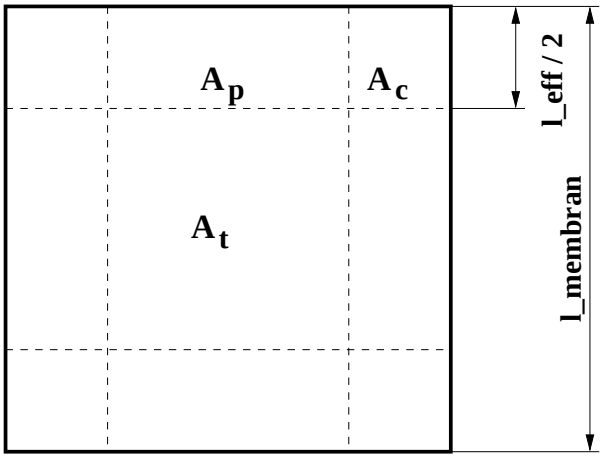

Fig. 3.33: Top view of a membrane, indicating different regions: A_t - counter-electrode touched, A_p - 2D approximation of the deflection curve, A_c - a corner fill fit applies.

justified. This leads to a simple formula for the local electrostatic pressure due to an applied voltage V:

$$p_{el}(x, y) = \epsilon \cdot V^2/(d_{gap} - w(x, y))^2 \, . \tag{3.14}$$

A formula for the membrane bending which considers non-uniform pressure loads would be difficult to obtain because the electrostatic pressure itself depends on the membrane bending. To keep the modeling process simple, the electrostatic pressure is averaged using equation (3.14) and the membrane bending shapes given in equation (3.9) and (3.12). The resulting averaged electrostatic pressure now adds to the applied hydrostatic pressure.

As described above, under the condition of a controlled deflection volume the bending shape of the membrane can snap from one into another state. An analytical description of the membrane behavior under such conditions would be extremely difficult to develop. In order to still accurately capture the correct snap conditions, fit parameters are introduced in the model, which can be determined by means of parameter extraction from FEM-simulated data. The achieved accuracy is illustrated in Fig. 4.9.

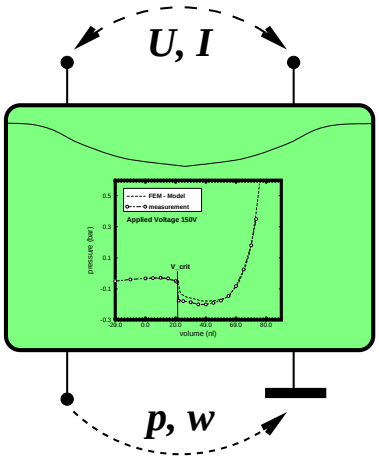

Fig. 3.34: Symbol of the membrane CM, as it could be used in a schematic editor.

In contrast to the fit-parameters introduced before, the latter ones are not well based on a solid physical analysis, but use coarse, qualitative approximations, only based on an empirical insight into the shape-snapping effect, as it could be gained from investigating the results of the FEM-analysis. This still does not harm the overall quality of the resulting model, because only a separated physical effect is involved, which occurs only under certain operation conditions.

The membrane bending shape is finally used to calculate the displaced volume. This results in a compact model for the electrostatically actuated membrane which has two internal state variables l_{eff} and w_{max} and four terminals. Two terminals belong to the electrical domain and the remaining two have a fluidic nature, with pressure and volume flow rate as the assigned quantities (Fig. 3.34).

The CM was coded in SpectreHDL, thus allowing the simulation on system level in an analog circuit simulator. The model sourcecode is shown in appendix B.

3.4.4 Extrapolation capability of the compact model

To test the extrapolation capabilities of the developed membrane model, a design parameter – namely the gap width between membrane and counter-electrode – was varied from 3 to 5μm. Using the same physical model parameter set for the modified device one still finds the model to be very accurate (Fig. 3.35), corroborating the aforementioned statement that a physically based modeling strategy is best suited for design studies. It is worth to mention here that the gap width has a highly nonlinear impact on the behavior of the membrane, which causes a simple linear extrapolation of certain device properties to be insufficient.

It should be mentioned here, that the accuracy of the model is reasonably good, even if all fit-parameters are set to unity, which means, that no parameter-extraction has been performed yet. That allows qualitative analysis such as the verification of system concepts to be performed even if no device measurement data is available yet.

Both the optimized 3μm gap model and the extrapolated 5μm gap model have been used

to simulate the frequency-dependent pump rate of an electrostatically driven micropump as reported in [60]. It shows that both models accurately describe the device operation (see section 5.4).

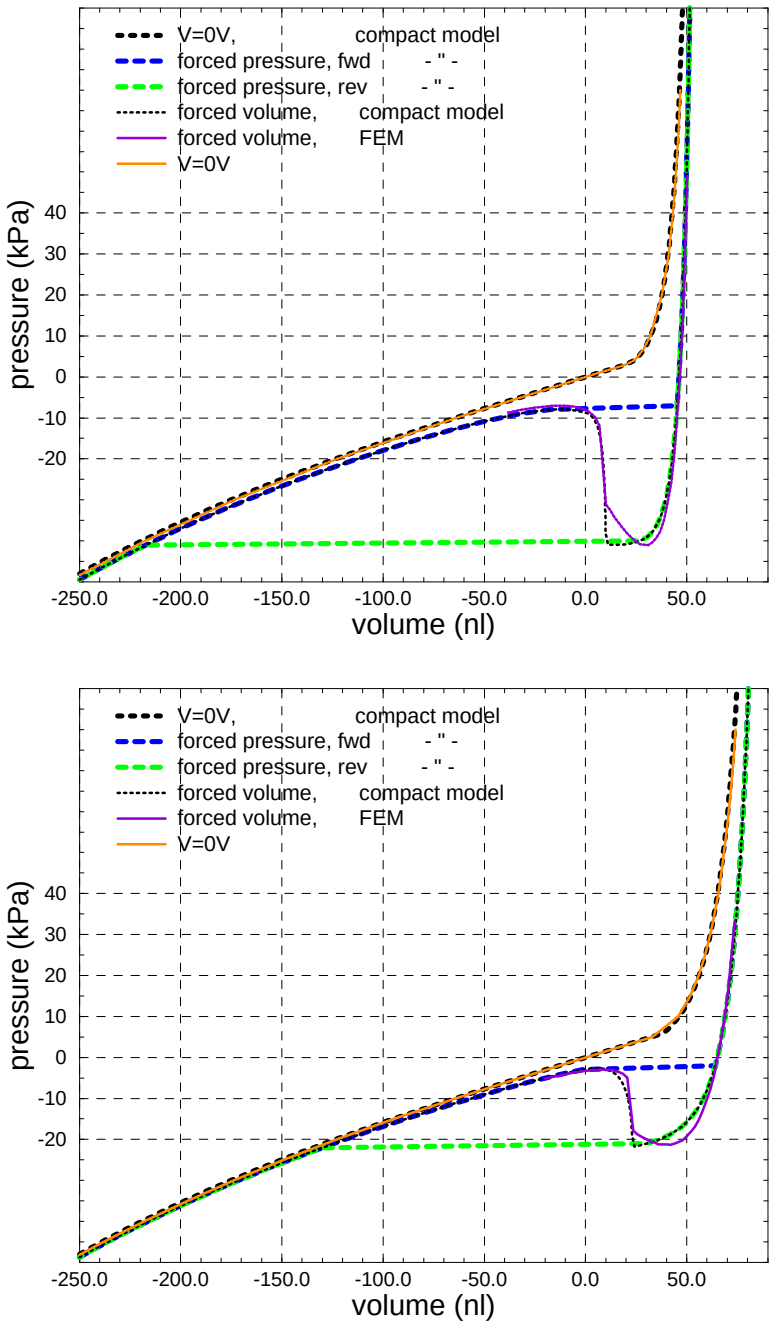

Fig. 3.35: Simulated static characteristics (hydrostatic pressure vs. displaced volume) of an electrostatically deflected membrane. Dotted/dashed lines: CM, solid lines: FEM. A voltage of 150 V is applied to the membrane, causing the well known snap effect. The fitting parameters of the device model are extracted from a membrane with 3μm gap width (top), then applied to a membrane with 5μm gap width (bottom). The achieved accuracy for the 5μm device shows the extrapolation capabilities of the underlying device model.

3.5 Summary

Three different methods of developing device models for system-level modeling have been presented. The demonstrated example of modeling the self-test of the ASIS acceleration sensor demonstrates the capabilities of a hybrid modeling approach, mixing FNMs and CMs to build a system macro-model. The simulation efficiency is high, compared to FEM-based approaches, and all relevant coupling effects are treated in a simultaneous manner. Thus, the usual convergence problems, related to successive coupling approaches in the case of strong coupling effects, can be avoided.

Once the required interface software between CAD-tool and analog network simulator is available, the simulation model can be set up easily and quickly. The advanced time integration algorithms implemented in circuit simulation tools are available. Additionally, all kind of numerical analysis (OP, DC, AC, transient, noise, sensitivity etc.) which are implemented in such tools, can be performed, even if different physical domains are coupled. This gives more flexibility and numerical efficiency than is typically available in FEM tools, while maintaining the same level of accuracy as the FEM analysis.

The experience gained from the presented example shows that it is worthwhile to extend the FN modeling to others than the thermal domain. It seems possible to use this approach as an very flexible, user programmable tool to simulate systems that couple different physical domains. The finite element which expresses the coupling between different physical domains, can be written in VHDL-AMS, whereas the discretization grid is set up in a CAD-tool. An special software tool, as a generalized version of ANTOS, then compiles the netlist for the circuit simulator, representing the system of ODEs that needs to be solved.

Two drawbacks of this approach should yet be mentioned here: First, the simulation time is still quite long compared to simulations based on CMs, because the number of equations that need to be solved is very high. Second, this method is inflexible with respect to variations of geometry and other parameters, because the full procedure of model generation must be re-run with each variation, starting from the solid model in the CAD-tool.

To summarize, The FN modeling approach provides a flexible, user-programmable coupled FEM plus CM simulation tool.

A PCA of a database, which was created from a set of FEM-simulations, can be used to generate a quasi-static CM of a device and yields very good results, as long as the device characteristics are continuous and the data range used to generate the database is not left. If some knowledge about the device physics is incorporated by transforming parameters, limited extrapolation capabilities can be added to the CM. The complete model generation procedure can be automated, thus requiring nearly no user interaction, but – due to the FEM-simulations – a lot of computer resources.

Since the dependencies on the device geometry, process parameters etc. are not explicitly expressed in the CM, the complete model generation must be rerun for each design or process modification, starting from an updated FEM model.

PCA-based CMs can be used to model the dynamic behavior of systems. Compared to FEM- or FN-models, the numerical efficiency is much better, while still the same level of

accuracy can be maintained. The setup of the dynamic equations for the resulting factors of the PCA respectively their dominant parameters is a complicated task and cannot be automated. Additionally, all the draw-backs of quasi-static PCA-based CMs hold true.

Analytical, physically based models can be used to efficiently simulate devices, which exhibit very complex behavior, including hysteresis effects and multiple discontinuities. A quasi-static example was presented in section 3.4. A dynamic example will be given in section 5.2.

This modeling method can be used for statistical modeling, yield/failure analysis etc., because all model parameters allow for a physical interpretation, thus making it possible to establish and subsequently to interprete correlations between variations of process parameters, design parameters, material parameters on the one hand, and the resulting changes in device and even system performance on the other hand.

The remaining fit parameters are closely related to certain physical effects, which are approximated by the device model equations. It will be shown in section 4.2, that a very efficient local parameter extraction strategy for those parameters can be established.

It could be demonstrated, that the resulting CM has good extrapolation capabilities, thus making predictive simulations possible not only on device level, but also on system level (shown below in section 5.4).

The disadvantage of this very powerful modeling method is that building such models requires a profound understanding of the physics of the device operation. Analytical modeling is a very involved task and requires a lot of engineering time. It is not seen how this model generation method could be automated.

So finally the decision for one of the presented modeling methods depends on the requests, which the resulting model must fulfill, requiring a careful evaluation of the pros and cons of each approach in light of the given circumstances like engineering resources, time constraints, hardware resources.

4. Parameter extraction

Model development cannot be considered independently of model validation and parameter extraction. Each modeling approach requires an appropriate extraction technique and, in return, the limitations of different extraction methods may influence the decision for a specific modeling strategy.

Of special importance is the case of parameterization of analytical, physically based compact models. Given that the model is constructed in such a way, that physical parameters and fit-parameters can clearly be distinguished from each other, an efficient parameter extraction strategy can be set up. The resulting model (including the extracted parameter set) can serve for important purposes such as design studies or statistical process control, e.g., thus justifying the usually large effort for the model development.

4.1 Parameter extraction methods

4.1.1 Fit-based models

In case of a modeling strategy purely based on data fitting, the model verification is simply a test if the simulated data reproduces the input data from measurement or CFM simulation within the required accuracy. The appropriate extraction technique would be a global optimization algorithm. The advantage is a very fast setup of the extraction, but one pays with typically lengthy optimization runs.

Additionally, one faces all the well-known problems of global optimization schemes. The optimization can be trapped in a local minimum. The result of an optimization therefore can depend on the initial guess of the parameters, and it may be very sensitive to small fluctuations in the target data, due to measurement noise, e.g. The extracted parameters can hardly be used for statistical process monitoring and a physical interpretation is quite often impossible.

4.1.2 Finite network models

Assuming that all information to build the FNM (geometry data and material parameters, e.g.) was readily available, no parameter extraction is necessary. Since a modification of any parameters in FNMs is difficult, and the simulation is not very efficient due to the large number of internal variables (grid nodes) of the FNM, a usage of FNMs to fit insufficiently well known parameters cannot be recommended.

The model verification is still an important step though. The critical points which must be

checked carefully are the mesh quality and the interfaces to the outer parts of the system, where the interaction is lumped into a single external node (as described in section 3.2). Such advanced tools like error estimators for the mesh quality are not available for FNMs. Therefore, the test for the mesh quality must be performed by optical inspection by an advanced engineer, or a FEM tool must be used for this purpose.

4.1.3 Basis-function models

The PCA is basically a method based on data fitting. Therefore, here no additional parameter-extraction is required. If however ODEs are used to describe the dynamic behavior of the device (as in section 3.3.1), then the parameters of these ODEs can be determined using parameter-extraction methods. The target data for the parameter extraction can come from measurements or FEM simulations. Since the deviation of the ODEs is based on a physical analysis of the device operation, the same approaches to the extraction of their parameters can be used as as to analytical, physically based models, which will be described in the following section.

4.1.4 Analytical, physically based models

If the developed model is based on the physical analysis of the device, a global optimization scheme could easily erode the physical content of the model parameters. Therefore, an extraction scheme utilizing direct extraction steps and carefully tuned local optimization needs to be employed [67]. Model validation becomes a very challenging task since it must be verified, if the model reproduces all relevant physical effects together with their process and geometry dependence. In that case, both steps, model validation and extraction setup, are very time consuming, but the resulting model parameters can be used for physical interpretation, yield analysis, process monitoring, etc. The time required for an actual parameter extraction run is typically short, thus allowing the processing of a large amount of data as it is required for statistical analysis [68].

The parameters with a physical meaning are (more or less) independent from an actual device structure, thus allowing to measure them using dedicated test structures. A parameter database may be established, making simulations in an early development stage possible, before real devices exist yet.

At the beginning of a parameter-extraction, a decision has to be made which parameters to extract. As mentioned before, normally the material parameters, device geometries and process parameters are known. Only the fit parameters must be extracted to improve the accuracy of the model (see Fig. 4.1 for a schematic picture). If however some of the just mentioned so called physical parameters are not available, or if their measurement is assumed to be too inaccurate, they can be extracted using measured device characteristics. Another reason for extracting physical device parameters is, that they can exhibit fluctuations from device to device. A measurement of those fluctuations and their correlation to known process fluctuations and to observed variations in system performance can be used for statistical modeling, for building yield models, for design centering etc.

Once the set of parameters that needs to be extracted has been set, a sequence of extraction

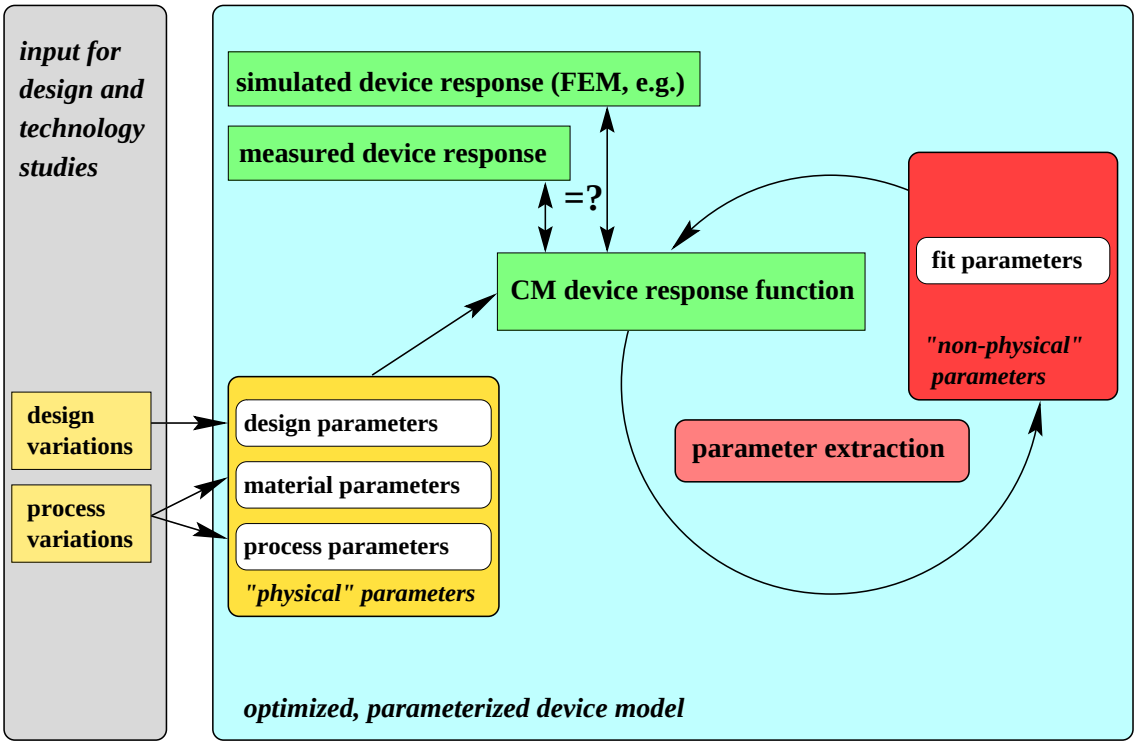

Fig. 4.1: Parameter extraction procedure for physically based compact models: with the physical parameters as input, the extraction sequence for the fit-parameters is iterated, until the device characteristics are matched. The resulting model (incl. the parameter set) allows for extrapolations.

steps must be found. It is important to start with the basic parameters, which impact most operating regions of the device. Parameters, which impact only very limited operating regions, can be extracted later in the extraction course. Ideally, only one parameter should be extracted at once.

For each parameter, the operating region must be determined, wherein this parameter has the strongest impact on the device behavior. If all other parameters have significantly less impact in this region, then the parameter can be determined, no matter if the other parameters are not accurately determined yet.

Now the parameter under consideration can be extracted directly. That means, that measured data points are substituting nodal variables in the model equations, and the resulting equation system is solved for the desired parameter. All other parameters appearing in those equations have either their default values or their previously extracted values if available. Here it becomes obviously that the parameter extraction sequence usually must be iterated (as sketched in Fig. 4.1): the extracted parameter value is – although not strongly – still dependent on other parameters, which are not extracted accurately enough yet. Given that this dependence is really not strong, very few parameter extraction cycles (typically not more than three) yield a stable, accurate model parameter set. Another point is important with direct extractions: since only very few data points are necessary,

the measurements of the device data can be performed very efficiently (example: if the principal shape of a curve is well known, the slope can be determined by measuring only two data points). Making point measurements is much faster than sweeping operation conditions. That makes direct extraction applicable for routinely measurements in production (for statistical process control (SPC), e.g.).

If direct extraction is not possible, because of transcendent model equations, e.g., local optimization can be used. Local optimization uses a very small subset of all parameters to match a very narrow, carefully selected range of the measured device data. To reduce the measurement effort, already the range of measured device data can be limited to the regions where the parameters to be extracted have their strongest impact.

The parameters with a physical meaning are (more or less) independent from an actual device structure, thus allowing to extract them by measuring dedicated test structures. A parameter database may be established, that makes simulations possible in an early development stage, before real devices exist.

Powerful software tool are available for the parameter extraction. To make those tools available for MEMS device CMs, some work is required, though. First, the interface to analog network simulators must be extended in such a way, that VHDL-AMS models can be simulated. Second, special extraction routines must be created, which perform the parameter extraction steps required for all devices under consideration.

In this work, a software interface has been created between Utmost and Spectre, which allows to run SpectreHDL models. Utmost-routines have been created, which allow the extraction of parameters for non-electrical four-terminal devices in a quasistatic as well as in transient operation mode.

4.2 Quasi-static example: electrostatically actuated membrane

The quasi-static CM of an electrostatically actuated membrane was presented in section 3.4.2. Now the parameter extraction sequence for this CM will be explained. The seven fit-parameters of this model will be extracted, whereas the other model parameters (the physical ones) are kept constant. They are assumed to be known from other measurements. Instead of really measured data, FEM-simulated data is used to perform the extractions.

The basic-most parameter of the model is the one, which fits the stiffness of the membrane for small deflections. Many effects can be hidden by this parameter: inaccurate material parameters like elasticity module, inaccurate geometry values like membrane diameter, inaccurate process parameters like membrane thickness. The parameter can be extracted by local optimization, using the data range in the rectangular box, shown in Fig. 4.2. All other parameters are still at their default values.

Alternatively, a direct extraction can be applied. Two data points in the marked region in Fig. 4.2 are used to determine the slope of the curve. From this slope, the fit parameter can be directly calculated, using the model equation for small deflections, corresponding to

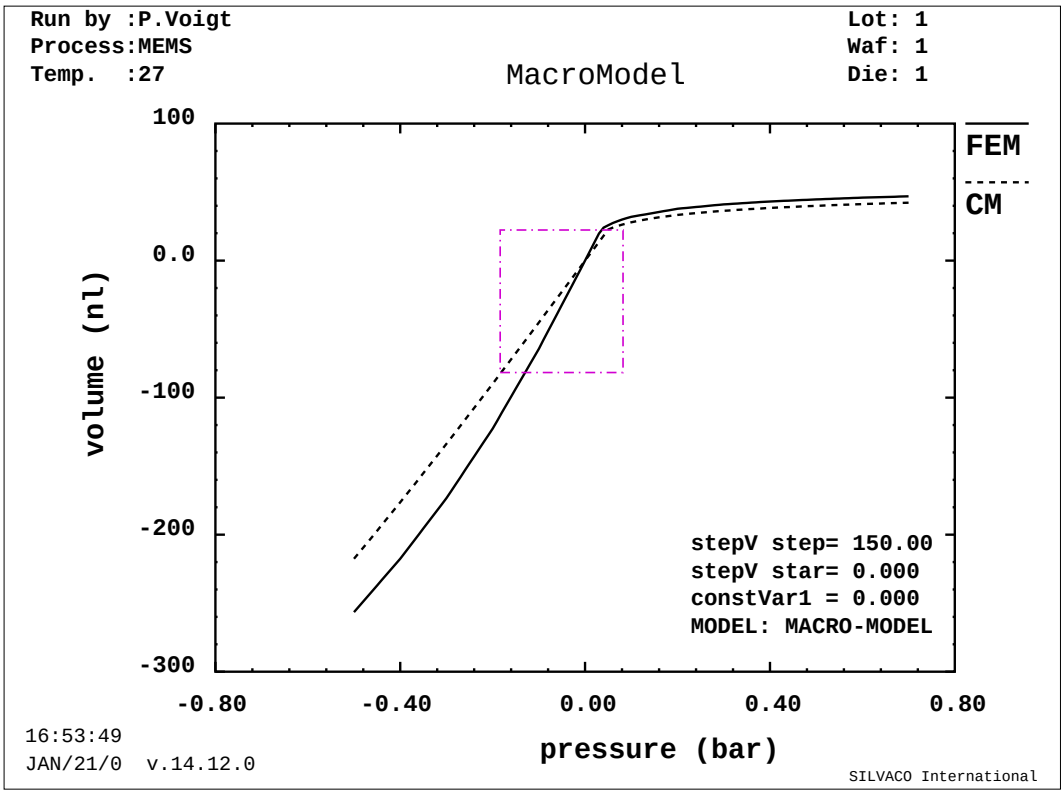

Fig. 4.2: First step: membrane stiffness to be fitted in the box region.

formula 3.9. That illustrates, that for a direct extraction only few data points are necessary instead of a sweep, thus significantly reducing the measurement effort.

The resulting simulated curve is compared to measured data in Fig. 4.3, showing a perfect fit for small deflections. The nonlinear effects for large deflections are fitted next, optimizing the corresponding parameter on the data range in the box in Fig. 4.3.

In the next step, the parameters for corner and edge filling are optimized in the box, shown in Fig. 4.4. Because these parameters have some weak impact on other operating regions as well, namely for large negative pressure, the accuracy of the model in this region is slightly reduced, as can be seen in Fig. 4.5. Re-adjusting the parameter for nonlinear effect in case of large deflections leads to high accuracy in this region as well (Fig. 4.6). This confirms the above statement, that the parameter extraction sequence must be iterated, but very few iterations are sufficient usually (only two cycles in the presented case).

Finally, the parameters for voltage-caused pull in and shape snapping are extracted (Fig. 4.7 to Fig. 4.9). The resulting model reproduces the device behavior accurately and can be used to extrapolate for modified design parameters, as shown in sections 3.4.4 and 5.4.4.

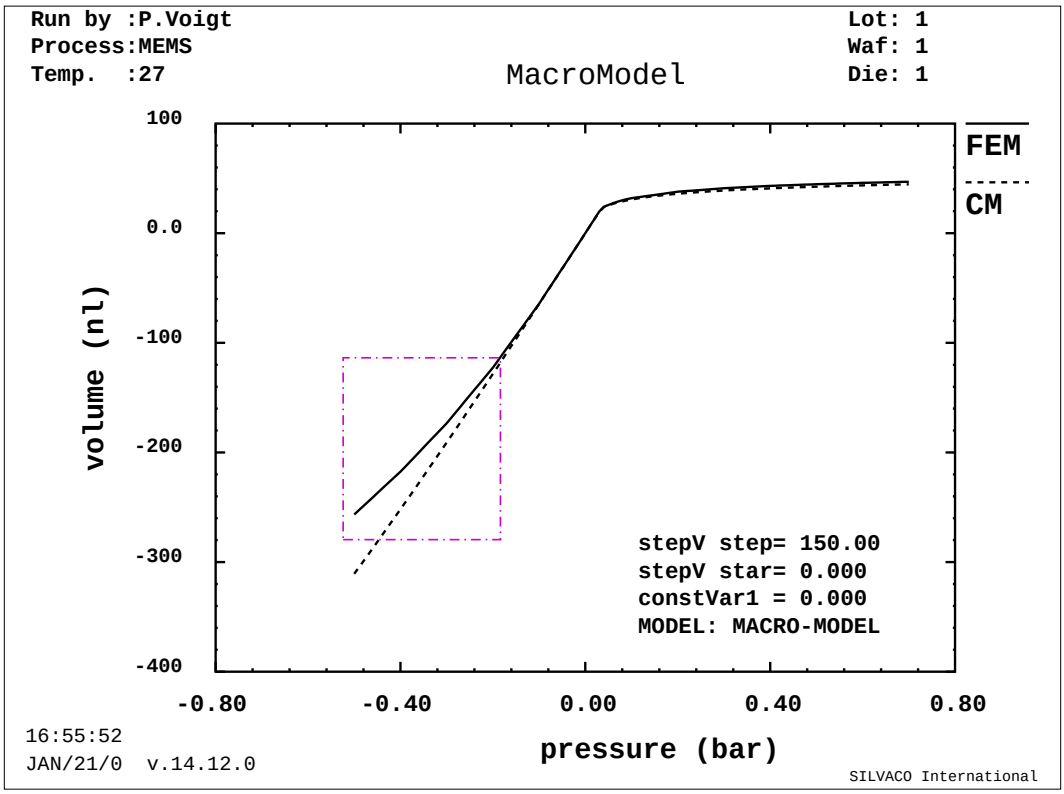

Fig. 4.3: Second step: nonlinearity of membrane stiffness for large deflections to be fitted in the box region.

4.3 Transient example: flap valve

The construction and operating principle of a flap valve as well as its compact model will be described in section 5.2. The mechanical part of the model basically is a mechanical oscillator with strong damping. The compact model of the valve flap was implemented into a system simulator [24], using VHDL-AMS. The system simulator was called from a parameter extraction software package [69], thus allowing the optimization of the parameters of the compact model to match the measured or FEM-simulated data. Most parameters of the model can be extracted on data of quasi-static device operation (some results in Fig. 5.12). The parameters to fit the size of the moving mass and the damping parameters require to use data of the dynamic behavior of the flap. The transient response of the valve flap to an step-like increase of pressure was used to this end. The required extraction routine was implemented in Utmost. An intermediate result of the parameter extraction is shown in Fig. 5.16. To extract the parameters, a sequence of optimization steps was applied, where each step uses a small part of the measured data.

The extraction of model parameters describing the dynamic behavior of devices is quite important for PCA-generated compact models, because the ODEs describing the dynamics of the factors are based on analytical models, containing approximations and the corresponding fit-parameters.

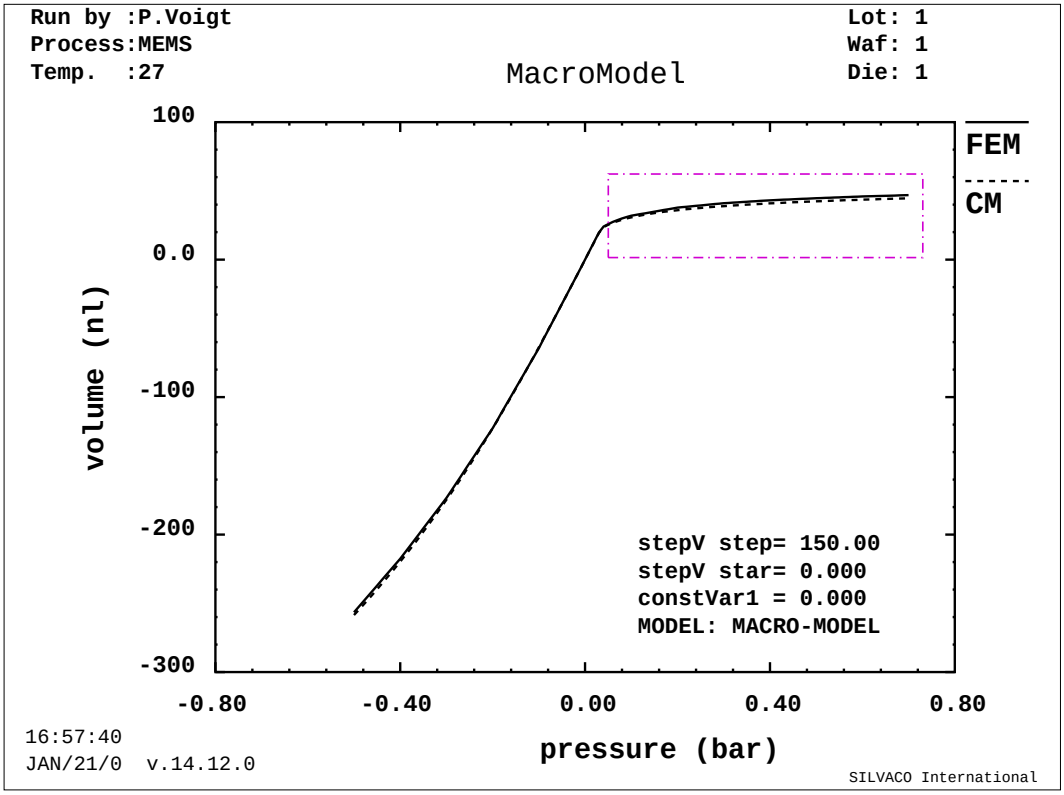

Fig. 4.4: Third step: membrane stiffness at edges and corners to be fitted in the box region.

4.4 Summary

It could be demonstrated that the methods for parameter extraction and the corresponding software tools, which are used in microelectronics for device model parameter extraction, can successfully be adopted to MEMS device compact modeling. It showed that parameter sets for analytically derived, physically based compact models, which contain only few, well understood fit parameters, can be extracted very efficiently. Since no global optimization steps are involved, the resulting parameter sets can be used for statistical modeling.

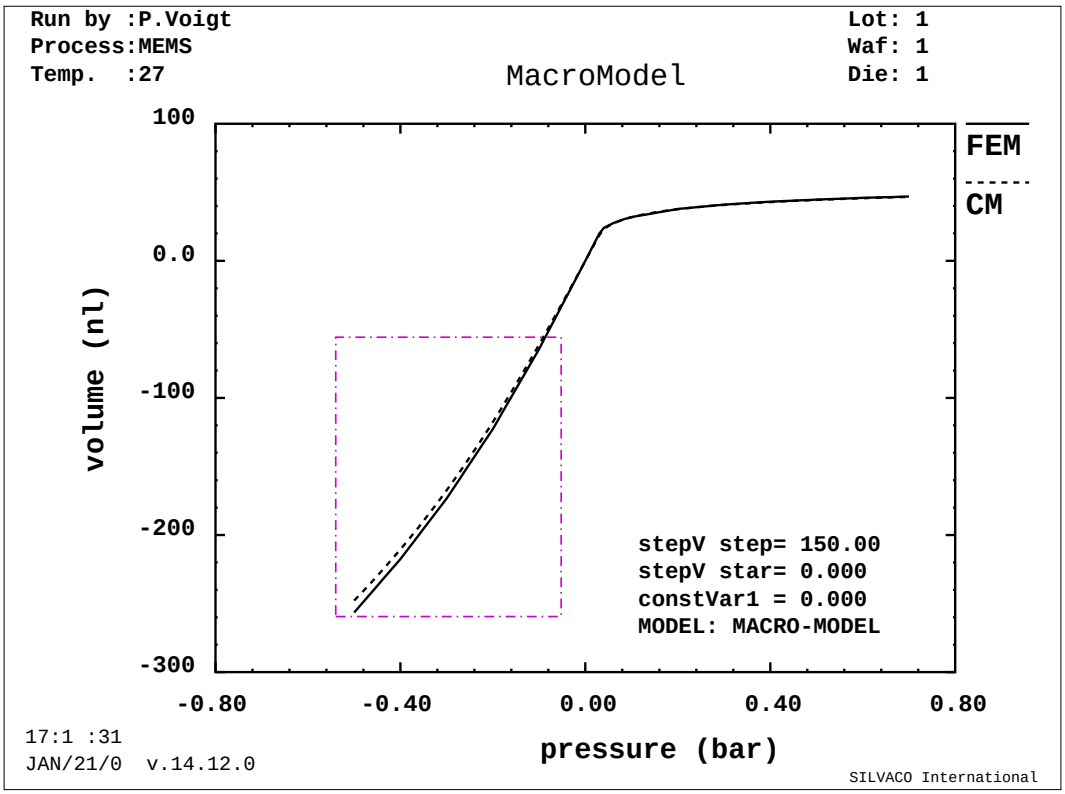

Fig. 4.5: Fourth step, re-iterating step two: nonlinearity of membrane stiffness to be fitted in the box region.

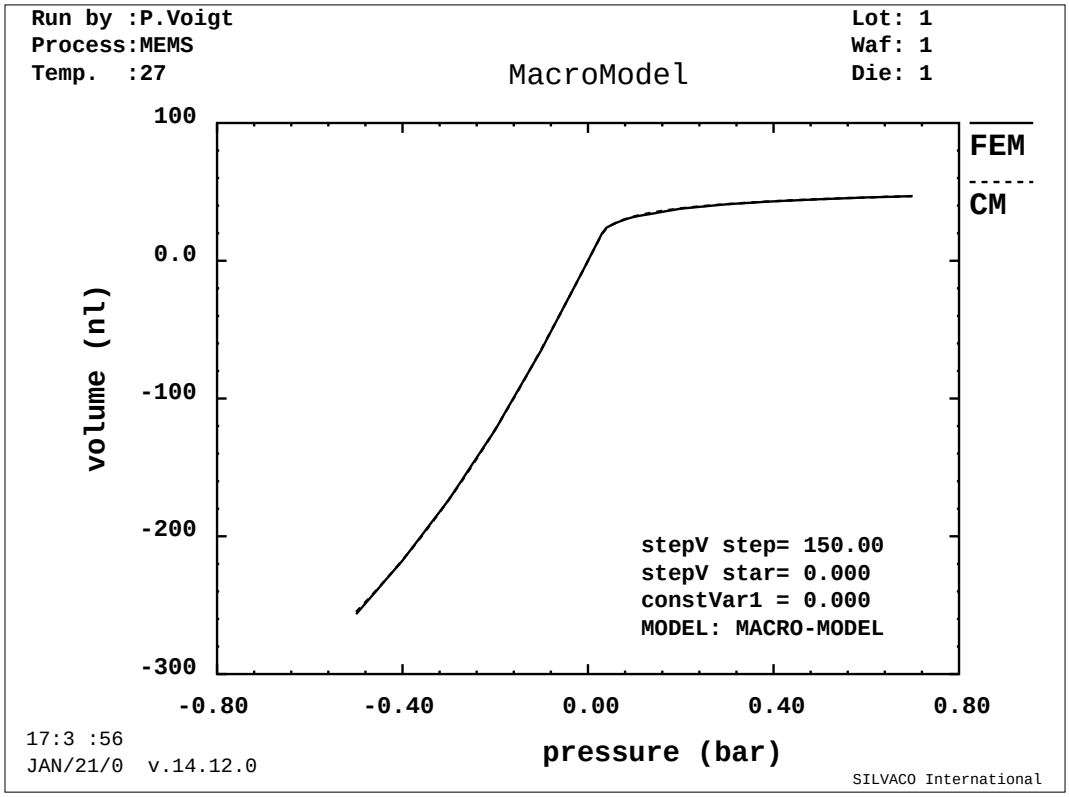

Fig. 4.6: Final result of the first part of the parameter extraction sequence, dealing with the mechanical properties only.

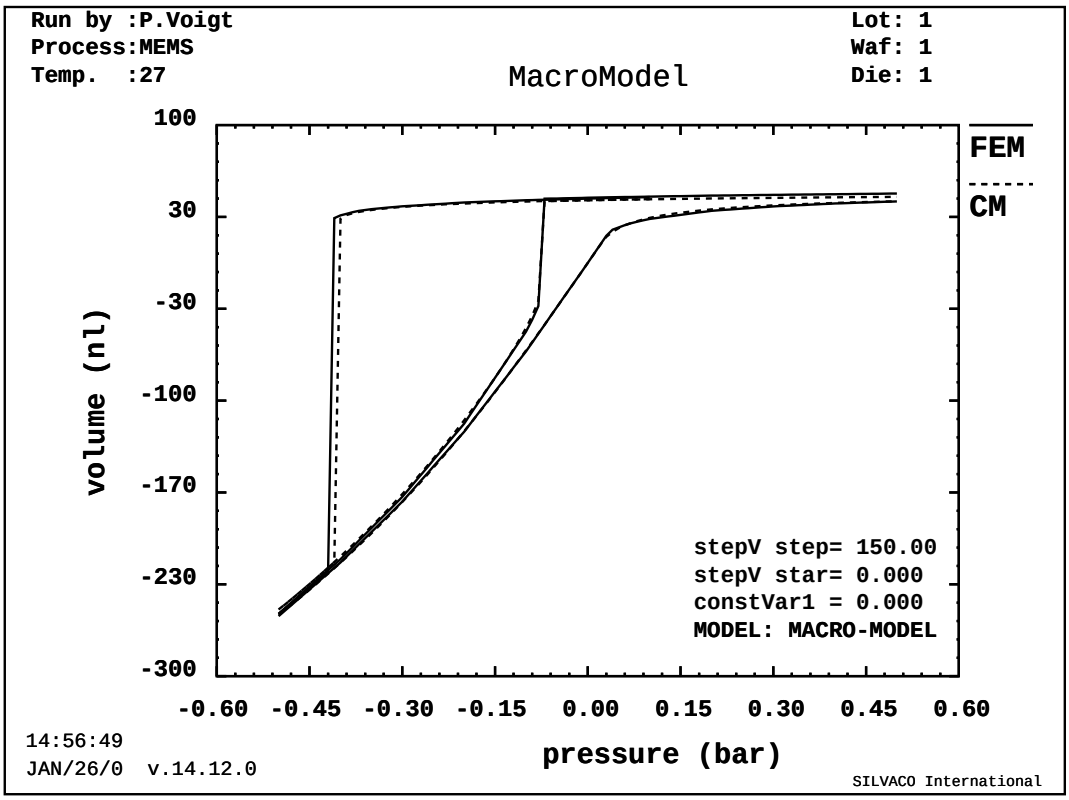

Fig. 4.7: Final results of a parameter extraction for the pressure-controlled quasi-static membrane characteristics. The applied electric voltage causes a hysteresis.

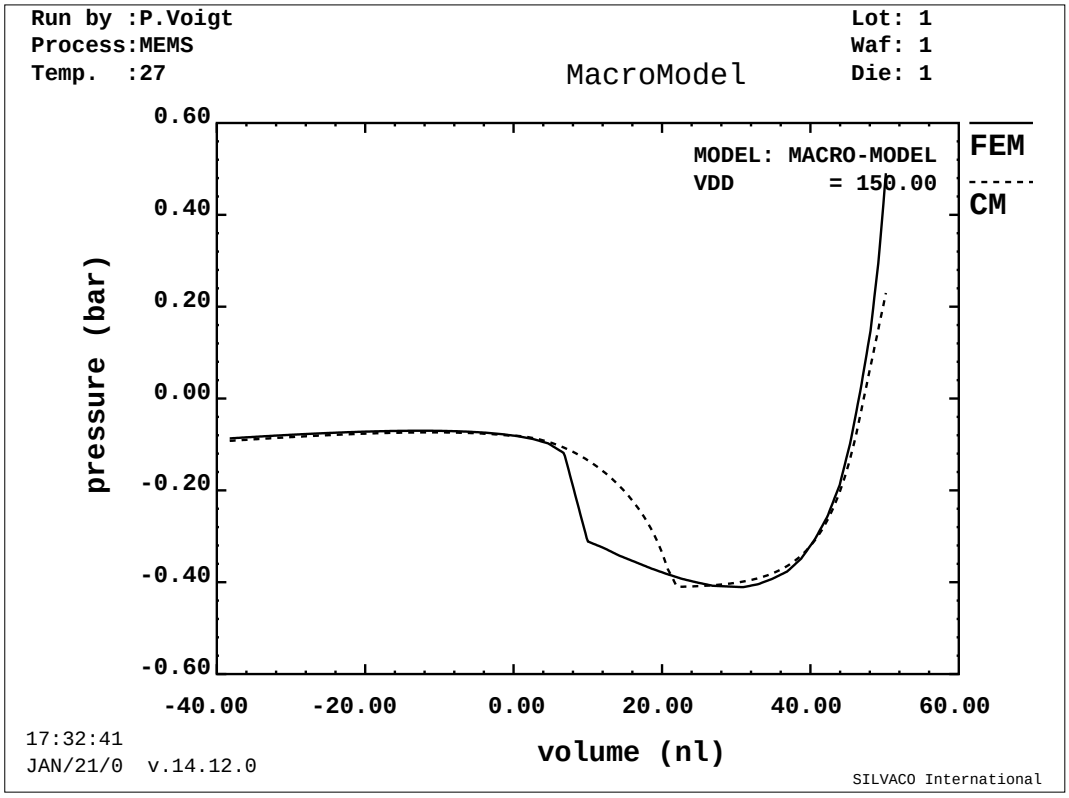

Fig. 4.8: Volume-controlled quasi-static membrane characteristics. Fit-parameters for the shape snap effect have to be extracted on this data.

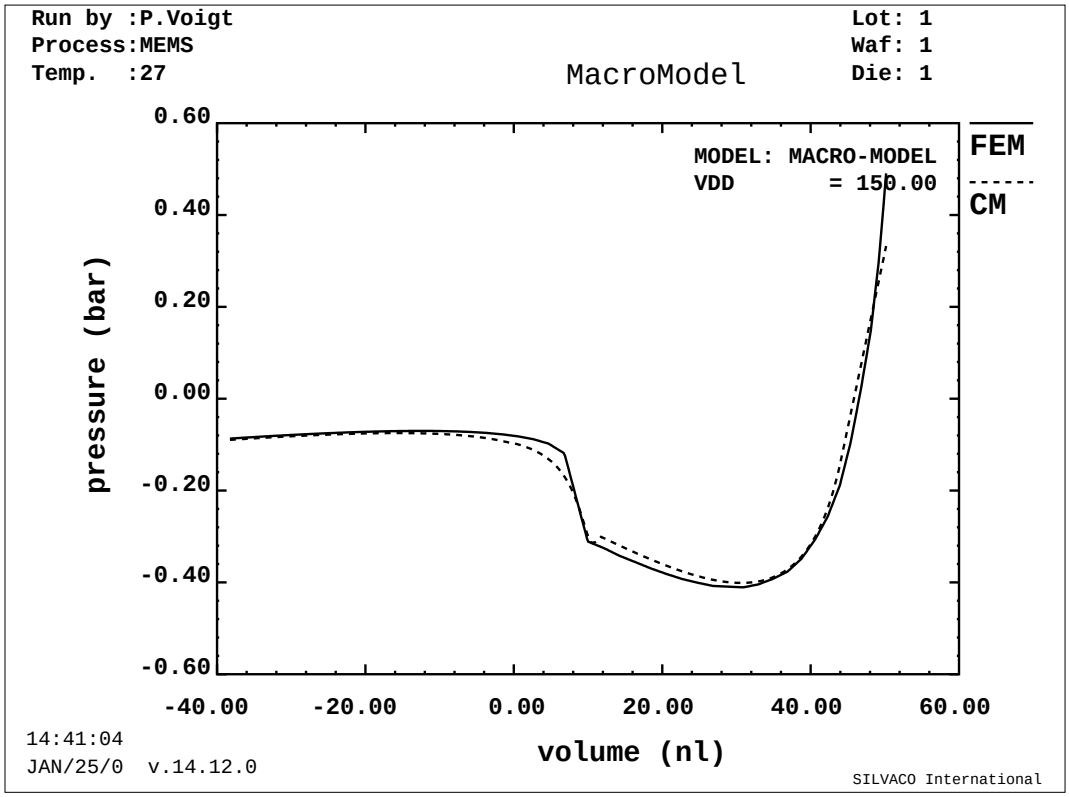

Fig. 4.9: Final results of a parameter extraction for the volume-controlled quasi-static membrane characteristics. Fit-parameters for the shape snap effect are extracted by means of an error minimization against FEM-simulated data.

5. Examples

In this chapter, five examples are presented, which illustrate various applications of compact modeling for microsystems. The first example demonstrates the integration of mechanical elements in an electrical circuit and the good performance of the chosen simulation approach in this case of strong, nonlinear coupling between mechanical and electrical behavior.

The second example is the analytical model of a flap valve. Combining it with the finite network model of tubes, presented as example three, and with the physically based model of an electrically actuated membrane, which was already developed in chapter 3.4.2, the macro-model of a micropump can be compiled. This is shown in detail in the fourth example.

The last example shows how to use analytical, physically based models to study the impact of process fluctuations on the performance of a complex, electro-mechanical system.

5.1 Electro-mechanical system: oscillator

5.1.1 Introduction

There are two reasons why the micro-electro-mechanical flip-flop structure was selected for presentation in the following section. First, in the membrane capacitor occurs a strong, highly non-linear coupling between mechanical and electrical phenomena. This requires an efficient simultaneous simulation of both parts of the problem, ruling out most other simulation approaches besides a common simulation of both problems in an electrical network simulator, including the mechanical part by especially derived compact models. Second, there exists a potential practical application of the presented structure.

The idea behind the presented microsystem design is to extract the mechanical eigenfrequency of a membrane by analyzing the electrical output signal of the circuit. That could be an interesting alternative to optical and other measurements [70], especially for routinely measurements in a production environment [71, 72]. This easy to measure teststructure we suggest for the extraction of mechanical parameters of thin layers [73]. An application to the extraction of damping properties seems possible as well.

5.1.2 Description of the teststructure

The structure under consideration is an electro-mechanical oscillator, realized as a flipflop with the capacitors C1 and C2 in the feedback loops (Fig. 5.1). The resistivity of the

transistors Mr11 to Mr22 can be varied in a very wide range by the control voltages V_{rp} and V_{rn}, thus allowing for a flexible control of the charge/uncharge time constant of the capacitors. The resulting oscillation frequency of the flipflop ranges from several kHz up to some 10MHz.

The above capacitors are polysilicon membranes with an area of $50\mu m$ x $150\mu m$, separated from a silicon substrate by a $0.5\mu m$ wide air gap. Together with the n^+–doped substrate as counter-electrode they form the two feedback capacitors of the flipflop circuit. The membrane structure allows for mechanical oscillations, excited by the electrical voltage across the capacitor. The capacitance varies due to the change in the distance between membrane and counter-electrode and, therefore, is responsible for the strong feedback between the mechanical and the electrical part of the system.

Such membranes are used in pressure sensors, microphones etc. and can be produced in a standard CMOS process with additional facilities for surface micromachining [74].

5.1.3 The simulation model

As mentioned above, a simulation approachwhich is well applicable for the given flipflop structure, is the analog network simulation. Therefore a compact model of the membrane capacitor had to be developed. A FEM analysis of the mechanical membrane properties resulted in the oscillation modes and their eigenfrequencies. Since an electrostatic actuation preferably stimulates the basic oscillation mode, the higher modes could be neglected in the compact model. The mechanical status of the membrane is described by a single parameter, the center deflection.

Subsequently, the membrane could be modeled as a simple damped oscillator. The electrostatic attraction of the membrane towards the counterelectrode due to the applied voltage acts on the oscillator as an external force, depending on the applied voltage and the actual gap between membrane and counterelectrode. This gap varies due to the membrane deflection.

The coupling between the electrical and mechanical subsystems appears in two ways: First, the attracting force depends on the distance d between membrane and counterelectrode and on the applied voltage. Second, the electric capacitance of the membrane capacitor depends on d also, thus impacting the electric circuit behavior. Especially if the mechanical deflection of the membrane is large, a significant change in the electrical capacitance of the membranes is expected, leading to a strong, non-linear bi-directional coupling between the mechanical and electrical behavior of the system. In such a situation, an efficient, simultaneous solution of both sub-problems is required. Successive iteration algorithms would definitely fail.

The resulting compact model of the membranes was implemented in HDL-A [26] and later on in VHDL-AMS.

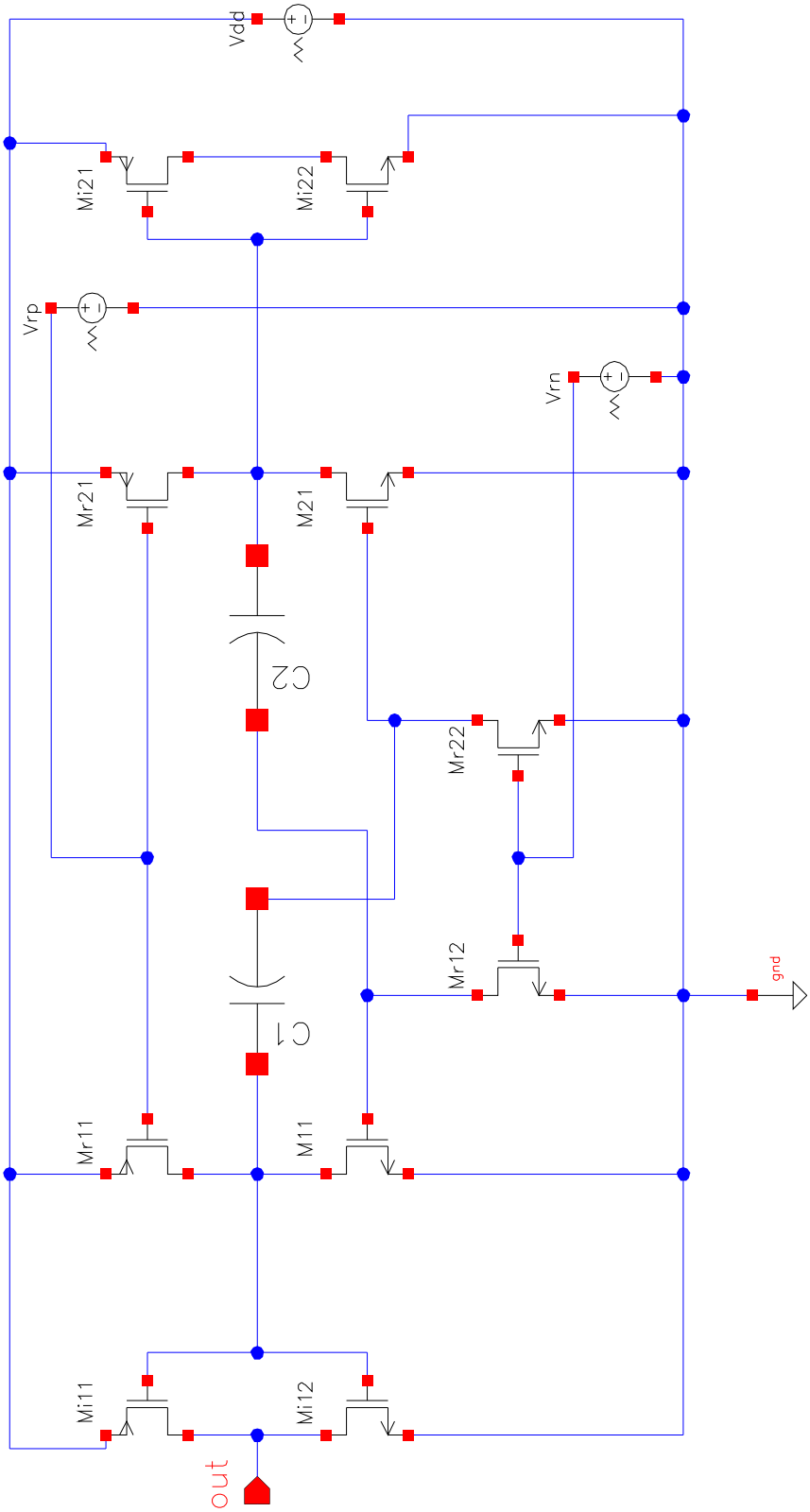

Fig. 5.1: Schematic view of the flipflop oscillator. C1 and C2 are membrane capacitors, allowing for mechanical oscillations.

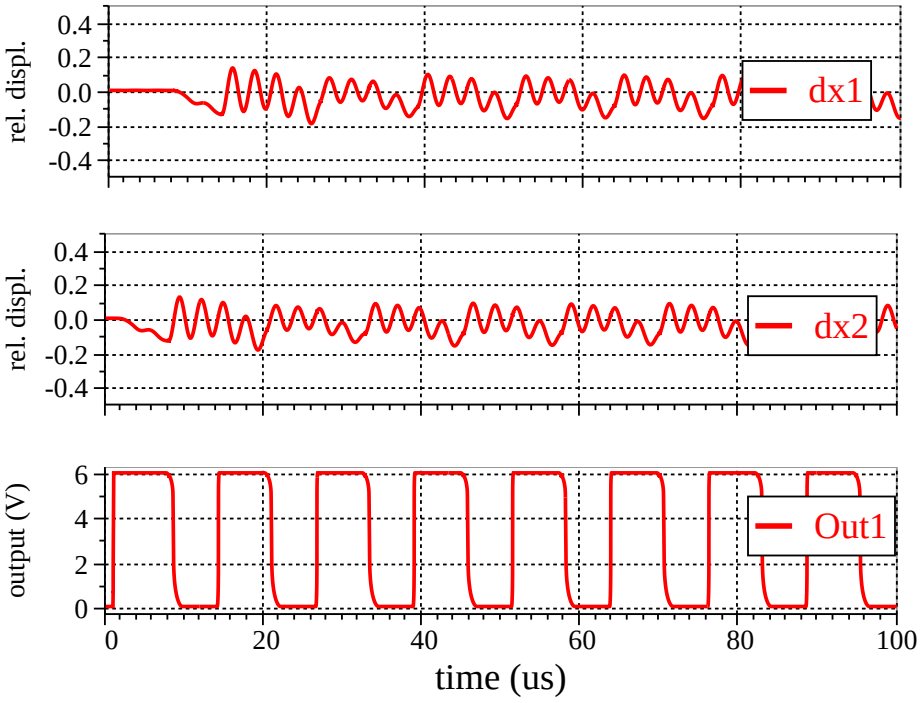

Fig. 5.2: Transient behavior of the flipflop oscillator: deflection relative to the gap distance (membrane 1: dx1, membrane 2: dx2) and output voltage. The flipflop oscillation frequency is below the mechanical resonance frequency.

5.1.4 Simulation results

An analysis of the transient behavior of the flipflop structure (Fig. 5.1) was performed using the analog network simulator Spectre.

First, the control voltages V_{rn} and V_{rp} are adjusted to such values that the flipflop oscillates well below the mechanical resonance frequency of the membrane. During operation, the membranes are exposed to steplike voltage changes from near 0V to approximately the supply voltage V_{dd} and vice versa. The attracting force due to the applied voltage bends them down, leading to a membrane oscillation (Fig. 5.2).

If now the control voltages V_{rn} and V_{rp} are adjusted to such values that the flipflop oscillation frequency matches the mechanical resonance frequency of the membranes, the amplitudes d_{x1} and d_{x2} of the membrane oscillations enlarge significantly (Fig. 5.3). The oscillating membrane modulates their capacitance, which results in a modulation of the flipflop oscillation frequency, which, in return, leads to a modulated membrane excitation. This effect becomes especially pronounced if the flipflop initially oscillates above the mechanical resonance frequency of the membrane, as can bee seen in Fig. 5.4. An oscillation of the membranes increases its average capacitance, thereby reducing the oscillation frequency of the flipflop, shifting it closer to the mechanical resonance frequency. This again increases the excitation efficiency and therefore the oscillation amplitudes of the membranes, thereby further increasing the membrane capacitances. This goes on until the flipflop oscillates at the mechanical resonance frequency of the membranes.

Thus, by analyzing the output signal of the flipflop, it is possible to determine mechanical

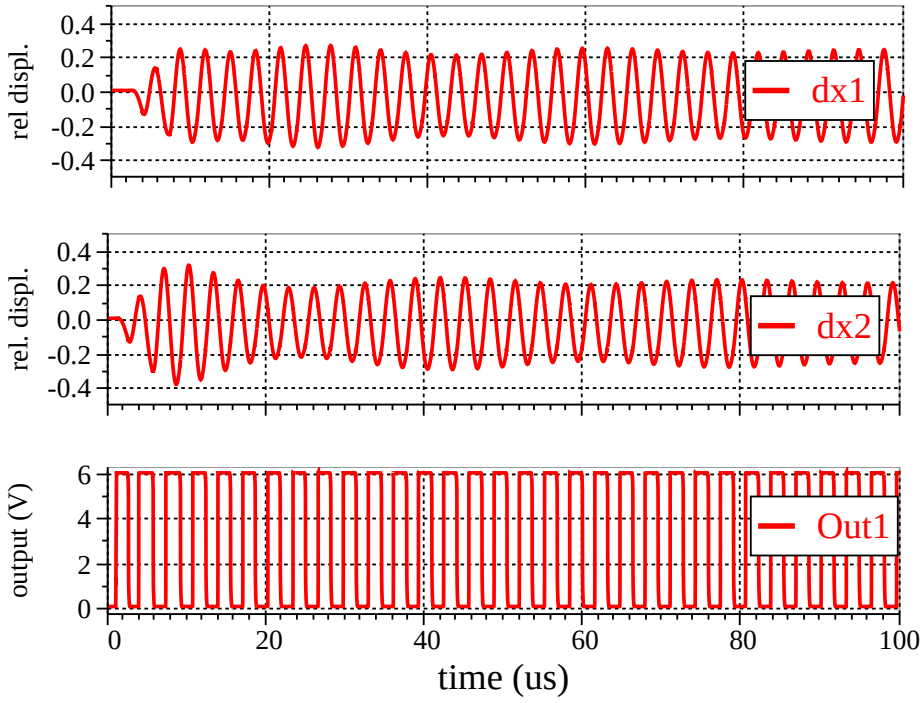

Fig. 5.3: Transient behavior of the flipflop oscillator: membrane deflection relative to the gap distance, and output voltage. The flipflop oscillation frequency is very close to the mechanical resonance frequency.

properties of membranes.

If the oscillation frequency of the flipflop is further increased, no significant mechanical oscillation can be excited (Fig. 5.5). A reduction of the damping, which can be achieved by reducing the air pressure, increases the oscillation amplitude. This makes it possible, that again a reduction of the flipflop frequency together with the resulting increase in mechanical oscillation amplitude can occur, until the system locks into the mechanical resonance frequency (Fig. 5.6). This effect could eventually be explored to measure damping properties of microstructures. In the case of low damping, the system appears to be very instable, leading to a behavior that looks ”chaotic” (Fig. 5.7).

All simulations presented here run very efficiently, taking no longer than 15 seconds on a HP9000/785.

5.1.5 Conclusion

A flipflop circuit with two integrated membranes as a test structure was presented, which exhibits strong coupling between the mechanical and electrical domains. We demonstrated that compact modeling is a powerful approach to the modeling of microsystems, especially in the case of such a strong coupling. We do not see any other simulation approach, which would allow for a complete analysis of the transient system behavior.

By means of system simulation it was possible to model the behavior of the above microsystem. The strong electromechanical coupling leads to the peculiar effects of modu-

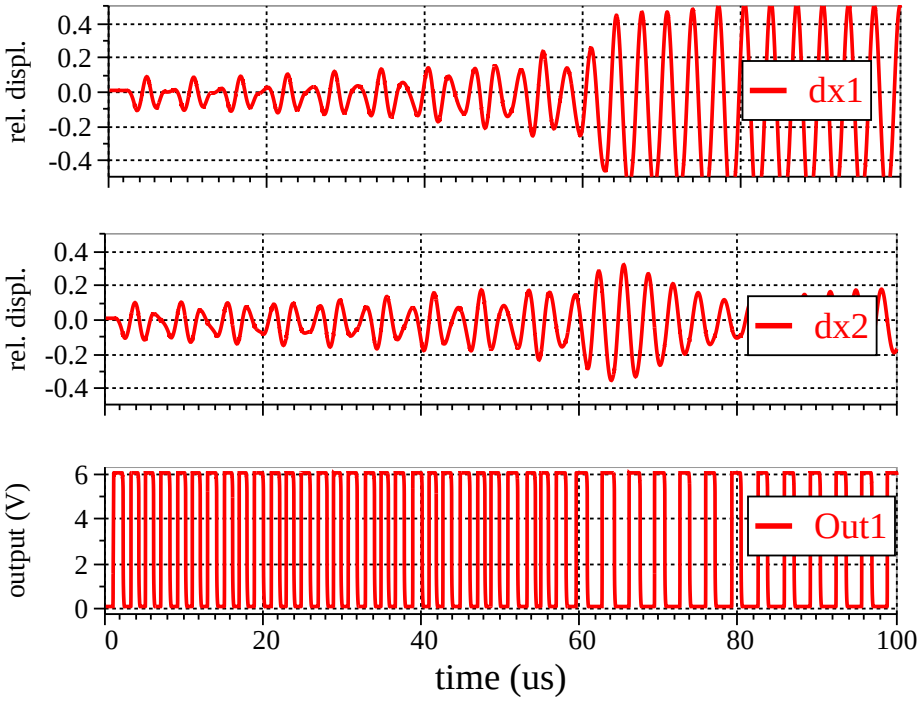

Fig. 5.4: Transient behavior of the flipflop oscillator: membrane deflection relative to the gap distance, and output voltage. The flipflop oscillation frequency is above the mechanical resonance frequency.

lated oscillations in the output signal and to the lock-in of the flipflop into the mechanical resonance frequency, which should enable to determine the mechanical resonance frequency of the membrane by a purely electrical measurement. Therefore this microsystem is proposed as a teststructure for a micro-electromechanical test-chip, allowing to extract the mechanical properties of thin layers.

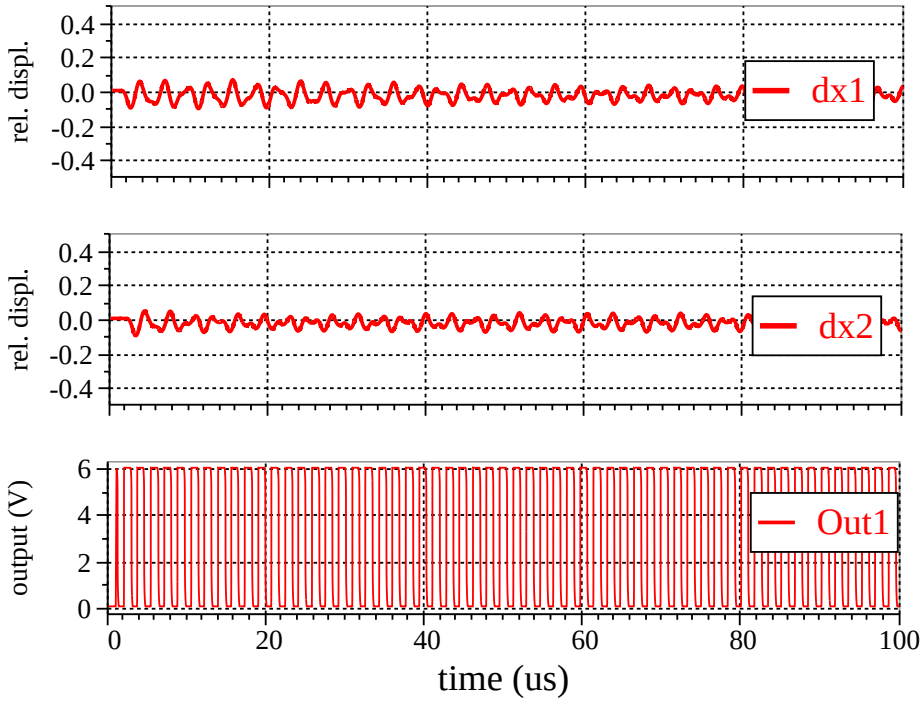

Fig. 5.5: Transient behavior of the flipflop oscillator: membrane deflection relative to the gap distance, and output voltage. The flipflop oscillation frequency is far above the mechanical resonance frequency.

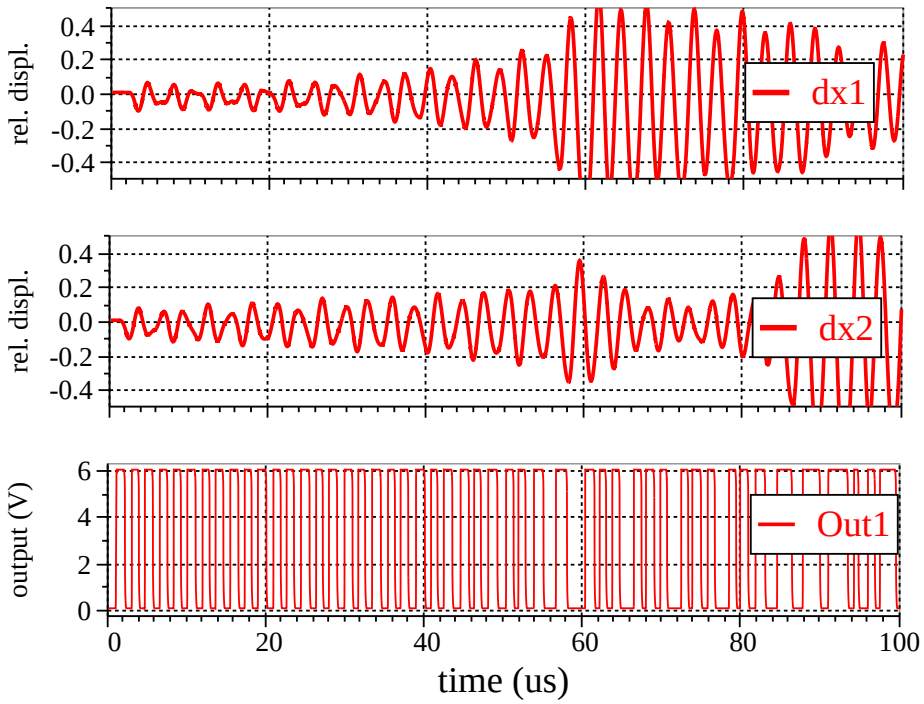

Fig. 5.6: Transient behavior of the flipflop oscillator: membrane deflection relative to the gap distance, and output voltage. The flipflop oscillation frequency is far above the mechanical resonance frequency. The damping is reduced by a factor of five.

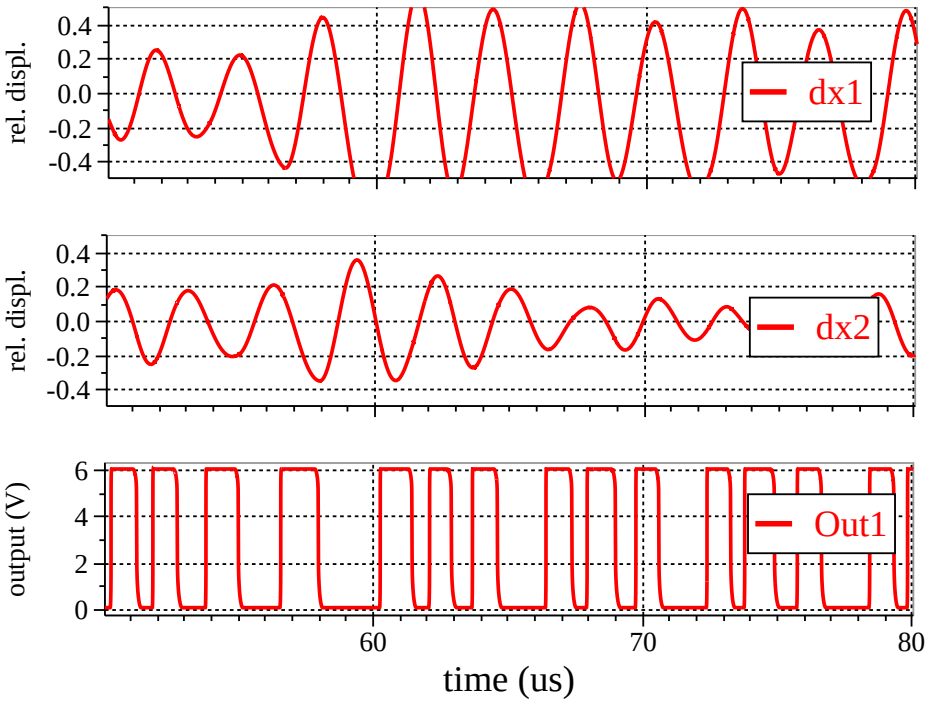

Fig. 5.7: Transient behavior of the flipflop oscillator: membrane deflection relative to the gap distance, and output voltage. The flipflop oscillation frequency is far above the mechanical resonance frequency. The damping is reduced by a factor of five. Detailed view.

5.2 A microfluidic flap valve model

5.2.1 Introduction

Active and passive check valves are an essential part in fluidic systems to control a fluid flow [75, 76]. In combination with an actuation unit they can be used to build pumps[60, 77]. Compared to dynamic nozzle valves, flap valves have the advantage of negligible leakage flow and therefore a high direction value [78, 79]. Disadvantages are, however, the complicated manufacturing process, and the sensitivity to particles, especially of the reverse leakage flow. The transient behavior of the valve flaps in the surrounding liquid can strongly determine the behavior of fluidic systems, leading to such peculiar phenomena as reverse pumping [4].

The flap valve modeled here was developed by R. Zengerle and is described in [60, 80]. It is made from three wafers (see Fig. 5.8) by means of selective, anisotropic wet etching of crystalline silicon and subsequent wafer-bonding. The bottom wafer contains the inlet opening and the valve seat, the middle wafer establishes a part of the pump chamber and is used to build the valve flap, whereas the top wafer caps the pump chamber, connects to the outlet, and may also be used to build a pump membrane.

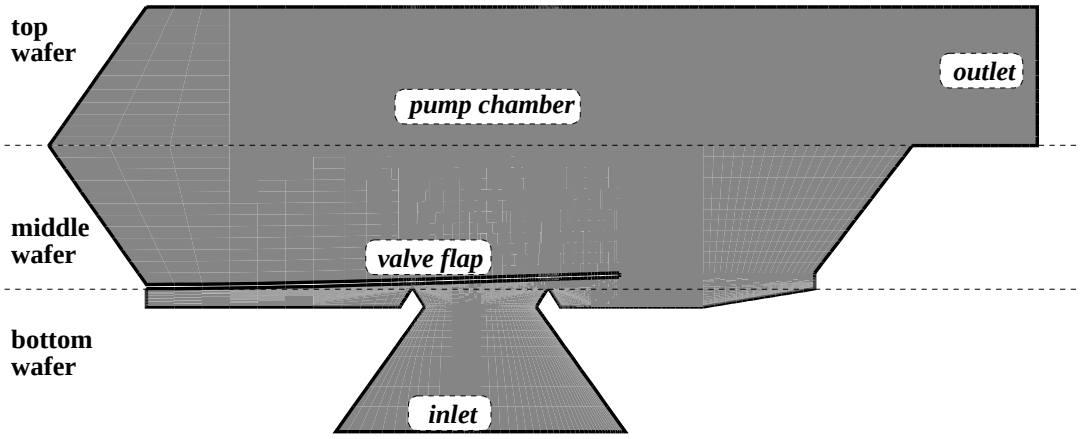

Fig. 5.8: Schematic view of a flap valve, made from three silicon wafers by anisotropic wet etching.

5.2.2 The compact model

Since the system behavior of the entire micropump is very sensitive to the properties of the valves [4], special attention had to be paid to the development of an accurate valve compact model. To this end, quasi-static and transient coupled FEM simulations using ANSYS and FLOTRAN [81] were performed by G. Schrag [36, 82, 83] to analyze in detail the interaction of the valve flap with the fluid flowing around it. The coupling between the structural analysis tool and the hydrodynamic simulator was realized in a similar way as described in [50] and [4].

The desired result of a CM development for the flap valve is an analytical expression

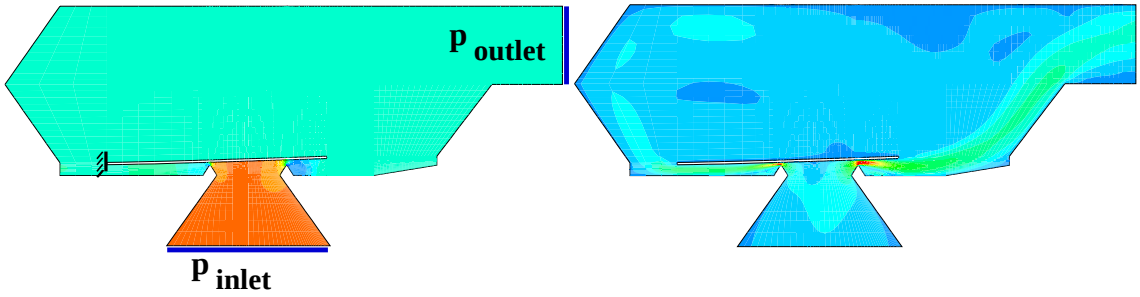

Fig. 5.9: Simulated quasi-static pressure distribution (left) and fluid flow velocity distribution (right) in a flap valve, when the valve is operated in forward direction, i.e. an applied pressure drop $\Delta p = p_{inlet} - p_{outlet} > 0$ opens the valve flap. It shows that the pressure in the pump chamber is nearly constant, keeping the fluid flow velocity low there.

describing the transient relation between pressure drop across the valve and flow rate through it.

At first, the displacement of the valve flap due to an applied pressure is modeled. A FEM analysis of this problem has shown that the pressure acts on the flap mostly in the region directly above the valve opening and, therefore, can be lumped to a force at the flap mid point. The resulting bending of the flap can be approximated reasonably well by an analytical formula for beam bending from [48]:

$$y_{mid} = \Delta p \cdot A \frac{l_{mid}^3}{3D} \tag{5.1}$$

$$D = \frac{E \cdot d_{flap}^3}{12 \cdot (1 - \nu)} . \tag{5.2}$$

Here, A stands for the cross sectional area of the valve, and y_{mid} and l_{mid} are the flap displacement at the center of A and the flap length measured from the flap suspension to the center of A, whereas E and ν are modulus of elasticity and Poisson ratio of the flap material, respectively. Therefore, the state of the flap can be described approximately by a single parameter, namely the flap displacement y_{mid}. In this way, y_{mid}. enters the CM as an internal state variable. When Δp changes from positive (valve open) to negative values (valve closed), the membrane hits the valve seat, and the stiffness of the flap increases significantly. This causes a discontinuity in the derivative of the function $y = y(\Delta p)$ (see Fig. 5.13). It should be noted here that even in reverse direction the flap can bend, i.e. negative displacement values are possible. This is an important factor for the model stability, because the bending in reverse direction allows to store energy (kinetic energy of the liquid is stored as potential energy of the deformed flap).

To get an analytical expression for the quasi-static flow rate through the valve, only the region is considered to be of importance where most of the pressure drop occurs (see Fig. 5.11). Because it would be difficult to describe the fairly complex behavior of the fluid in this region, an approximation for the quasistatic fluid flow w_{qs} through a rectan-

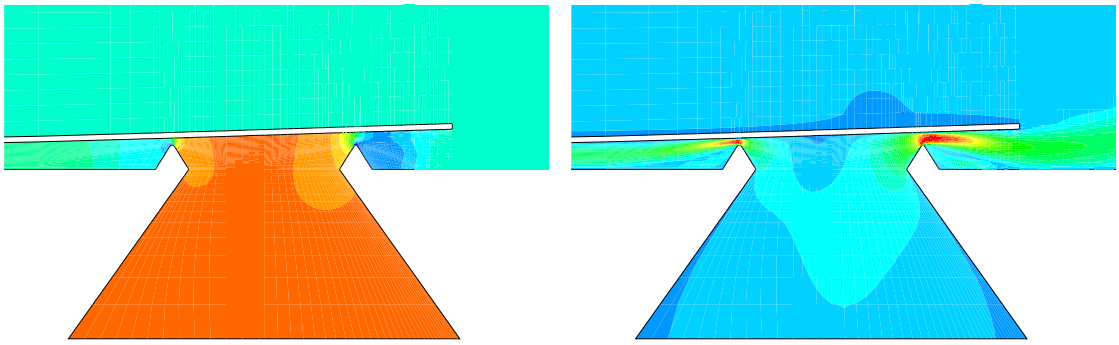

Fig. 5.10: Simulated quasi-static pressure distribution (left) and fluid flow velocity distribution (right) in a flap valve, detailed view. It can be seen that the pressure drops mostly in the proximity of the valve seat.

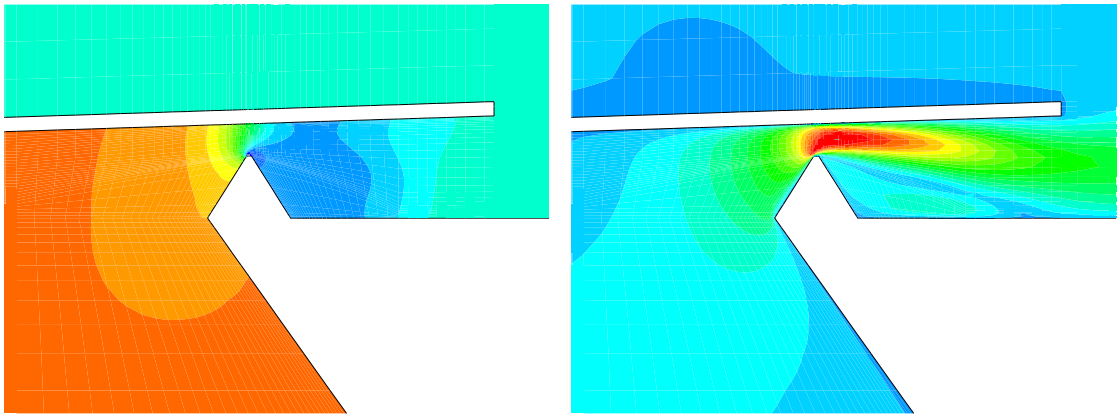

Fig. 5.11: Simulated quasi-static pressure distribution (left) and fluid flow velocity distribution (right) in the proximity of the valve seat of a flap valve. The pressure drop occurs in the vicinity of the valve seat.

gular slit is used [84]:

$$w_{qs} = l_{perim} \cdot y_{mid} \cdot \sqrt{\frac{2 \cdot \Delta p}{\rho \left(\lambda \frac{l_{pdrop}}{2 l_{perim}} + 1.5\right)}} \tag{5.3}$$

$$\lambda = 96/Re \tag{5.4}$$

$$Re = \overline{v} \cdot 2\, y_{mid}/\nu\,. \tag{5.5}$$

Here ν is the kinematic viscosity of the fluid, l_{perim} stands for the perimeter length of the valve seat, and l_{pdrop} is the width of the range wherein most of the pressure drop occurs. The latter is assumed to be equal to y_{mid} times a fit parameter. This value is used in the CM again to modify the area at which the pressure applies to the valve flap. The complete compact model code can be found in appendix A.

The involved model parameters can be obtained from a comparison to FEM simulated data (Fig. 5.12). A comparison of the compact model with measurements from [80] and with FEM results is presented in Fig. 5.13 and demonstrates the validity of this approach.

A transient FEM analysis of the valve flap behavior shows that the flap can perform damped oscillations in the fluid. The mechanical restriction due to the valve seat is ne-

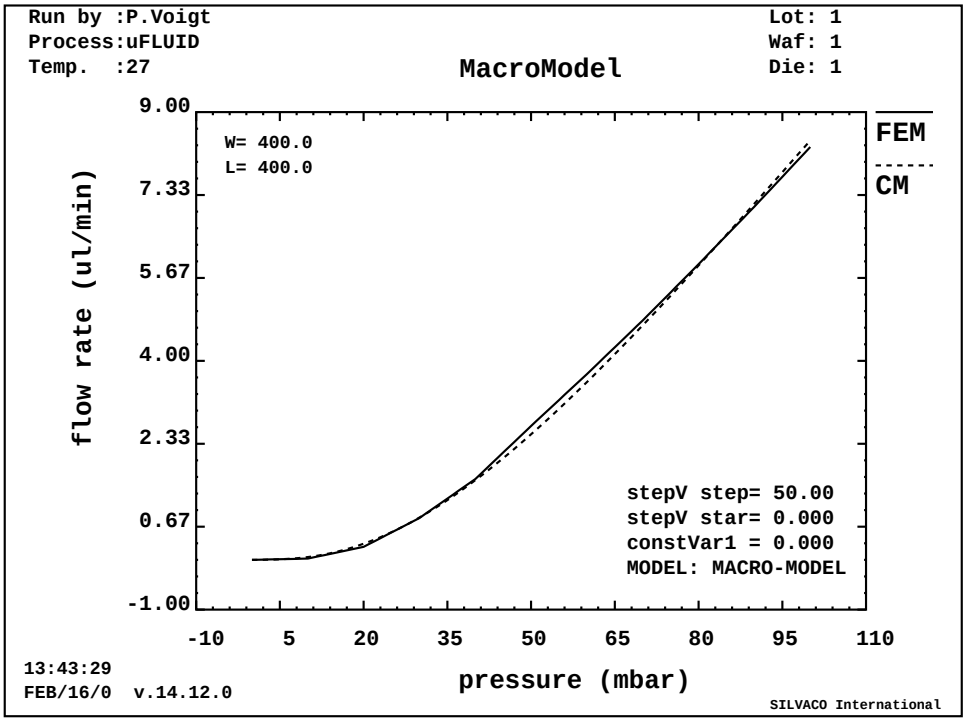

Fig. 5.12: Quasi-static flow rate vs. pressure characteristics of a flap valve. A parameter extraction for the compact model was performed using FEM simulation results as target data.

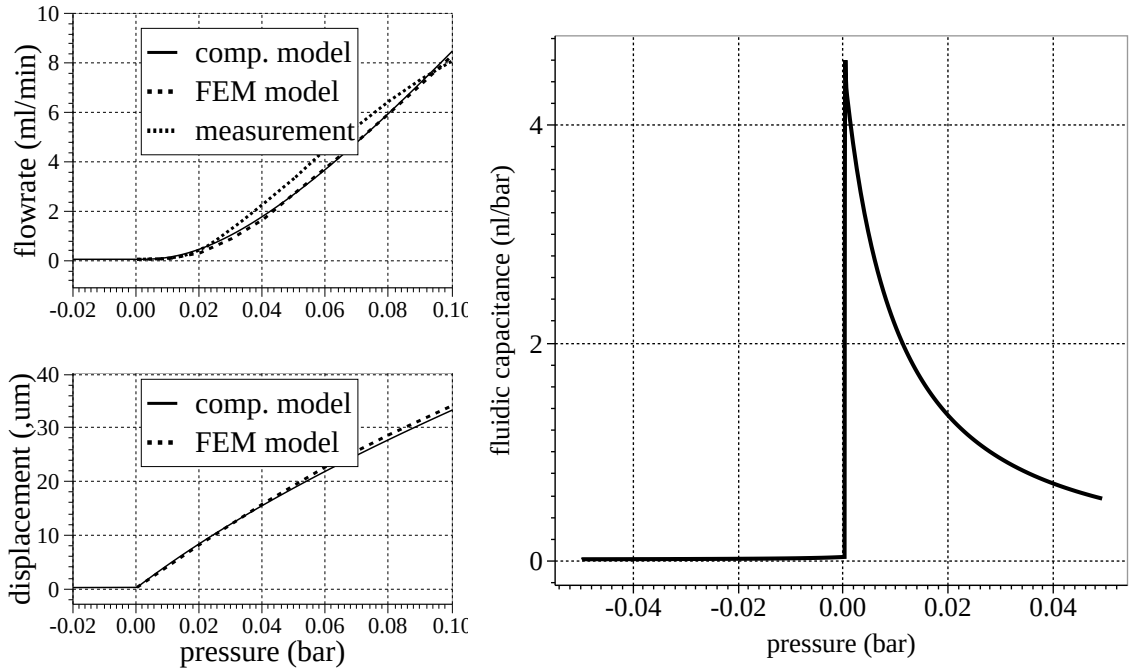

Fig. 5.13: Static characteristics of a valve (flap displacement, mass flow and fluidic capacitance vs. pressure). The simulation results of the compact model are represented by solid lines.

glected in this simulation. The oscillation frequency in water is by a factor of 6 lower than in vacuum, and strong damping is observed (Fig. 5.14). An inspection of the velocity dis-

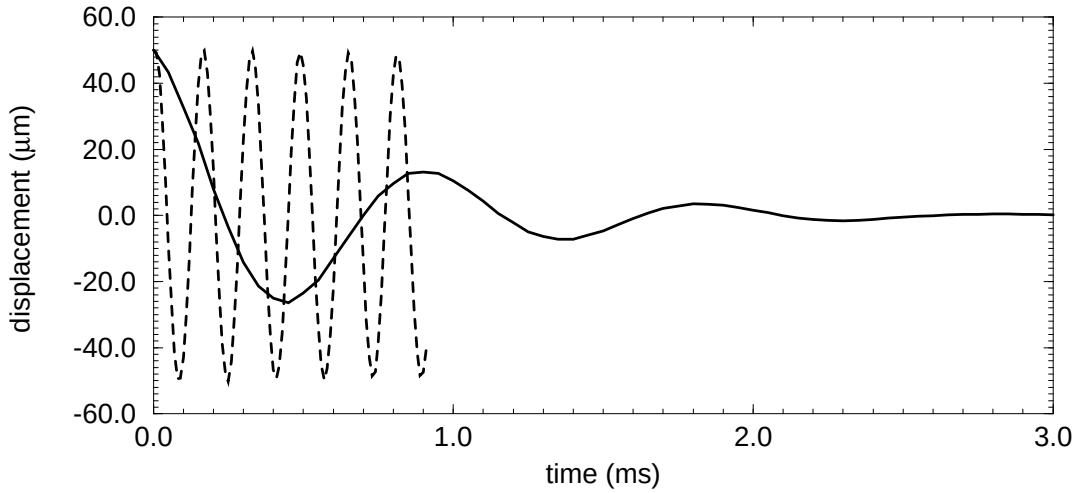

Fig. 5.14: FEM simulation of an oscillating flap (valve seat ignored) without (dotted line) and with (solid line) damping due to surrounding liquid. The flap is initially displaced by $50\mu m$ and then released to oscillation. In the presence of a liquid the oscillation frequency is decreased by a factor of 6 and strong damping is observed.

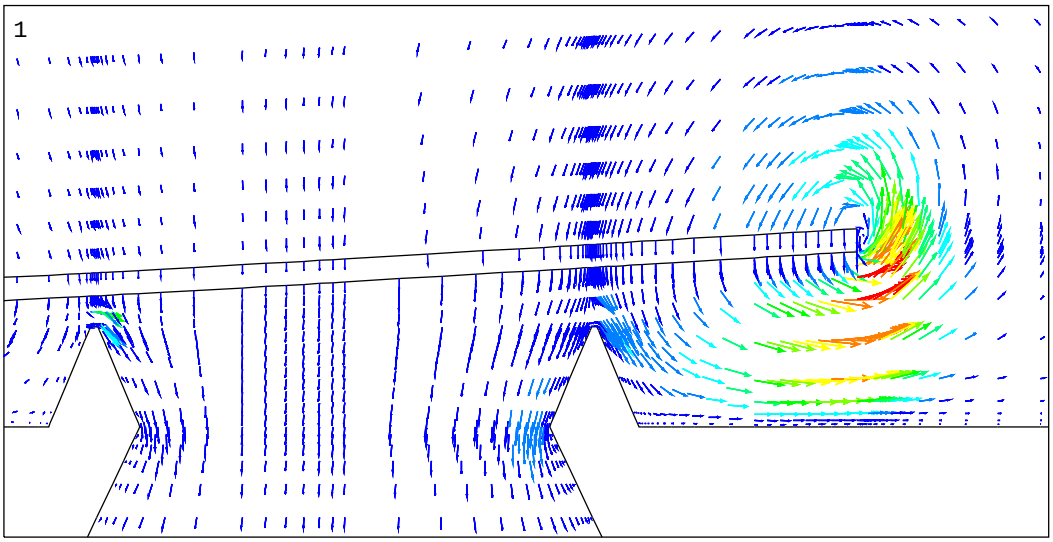

Fig. 5.15: Transient FEM simulation of the fluid velocity in a valve chamber due to a closing valve flap. The flap is initially displaced by $50\mu m$ and then released to close the valve. The fluid velocity caused by the moving flap ranges from 0 to 1m/s. The vertical dimensions of the valve are stretched by a factor of 2 for better visibility.

tribution around a moving flap as shown in Fig. 5.15 reveals that a significant amount of liquid is dragged by the moving flap, thus adding to the inertial mass and decreasing the resonance frequency. Additionally one finds that the moving flap causes a displacement flow through the valve, and that a swirl occurs at the tip (i.e. edges in a three-dimensional consideration) of the flap.

To incorporate all these observed phenomena in the CM, in a first step an inertial force was added to the force balance between applied pressure and mechanical restoring force of the bent flap. It is assumed to act on the same point of the membrane as the hydrostatic pressure load does, namely at the center of the area A. The inertial mass used in the CM is the mass of the flap plus a layer of liquid above and beneath the flap, which is dragged by the moving flap. Although there exist proposals how to analytically model the added mass over a moving plate [85], we decided to use the thickness of this layer as a fit-parameter in the compact model, which is determined by comparison to FEM simulated data (see section 4.3), such that the resonance frequency of 1.2kHz (in water) is matched. It shows that the thickness of this layer is approximately ten times the flap thickness, which looks reasonable when analyzing the FEM simulation results in Fig. 5.15, and appears more likely than values of 1020 - 2360 as given in [4].

Next, the displacement flow w_d due to the moving flap is calculated and, togehter with the quasi-static flow rate (eqn. 5.3), contributes to the total flow rate w through the flap:

$$w_d = A \cdot dy_{mid}/dt \tag{5.6}$$

$$w = w_{qs} + w_d \, . \tag{5.7}$$

The corresponding “fluidic capacitance”

$$C_f = dV/d(\Delta p) \tag{5.8}$$

with V being the volume displaced by the moving flap membrane is shown in Fig. 5.13. Please note the discontinuity at $\Delta p = 0$, when the flap touches the valve seat.

Finally, the damping was modeled by a force term proportional to the velocity of the flap and by a second term proportional to the square of the flap velocity. The latter is motivated because of the swirl at the flap’s edges. Both damping terms add to the force balance of the valve flap. The damping coefficients could be extracted from FEM simulated data (Fig. 5.16).

5.2.3 Simulation results

When the valve switches from reverse to forward flow under the action of a steplike pressure change, the flap starts oscillating in the fluid (Fig. 5.17, left). On the other hand, when a steplike pressure change forces the valve from forward to reverse direction, the valve flap hits the valve seat, bends down a only little bit due to the largely increased stiffness in reverse mode, and then gets bounced back, leading to a chatter motion. This type of a damped oscillation is highly inharmonic (Fig. 5.17, right), making it impossible to assign discrete resonance frequencies to it. A detailed analysis of this effect based on FEM appears to be very involved due to the numerical complexity and was beyond the scope of this work.

A small signal analysis of the valve behavior in case of a sinusoidal pressure stimulus shows the expected, typical picture of a damped second order system for the flap displacement (Fig. 5.18, top). The flow rate has two contributions. The displacement flow, caused by the moving flap, is in phase with the flap motion. It dominates above the resonance

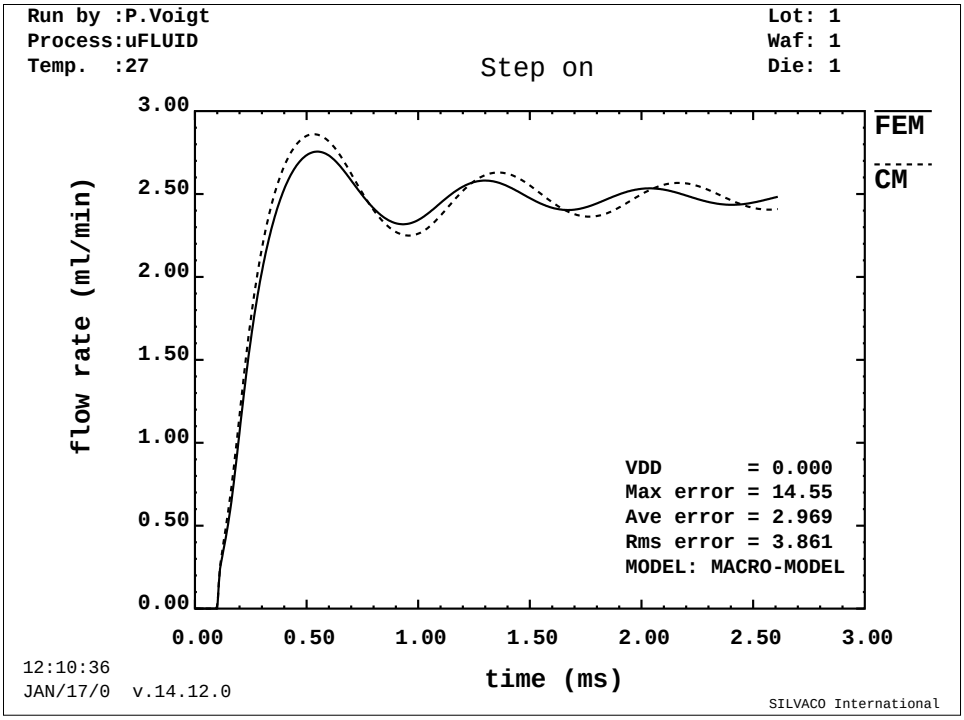

Fig. 5.16: Transient response of a flap valve to a steplike pressure stimulus. A parameter extraction for the compact model must be performed using FEM simulation results as target data, to determine parameters responsible for the resonance frequency and the damping.

frequency. The other contribution is driven by the pressure and depends on the pressure and on the flap displacement (eqn. 5.3). It dominates below the resonance frequency.

The compact model of the flap valve contributes to a macro-model of an electrostatically driven micropump (see chapter 5.4 for details). It shows that the dynamic behavior of the flap valve, namely the phase shift between pressure and flap displacement at drive frequencies above the resonance frequency is responsible for the peculiar effect of reverse pumping [62, 60]. A variation of the square damping parameter of the flap CM shows it's strong impact on the system behavior, especially in the regime of high driving frequencies (Fig. 5.19).

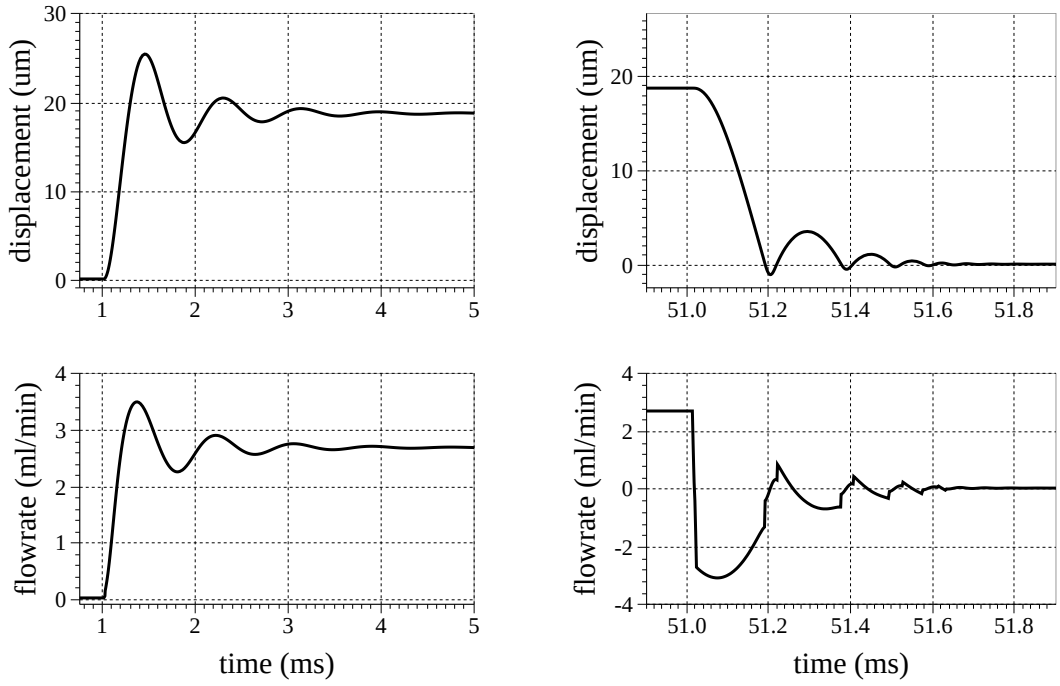

Fig. 5.17: Simulated flow rate and flap displacement of a valve as caused by a steplike pressure change from reverse to forward direction (left) and from forward to reverse direction (right). In the latter case the response of the flap consists in repeated bouncing against the valve seat (chatter effect).

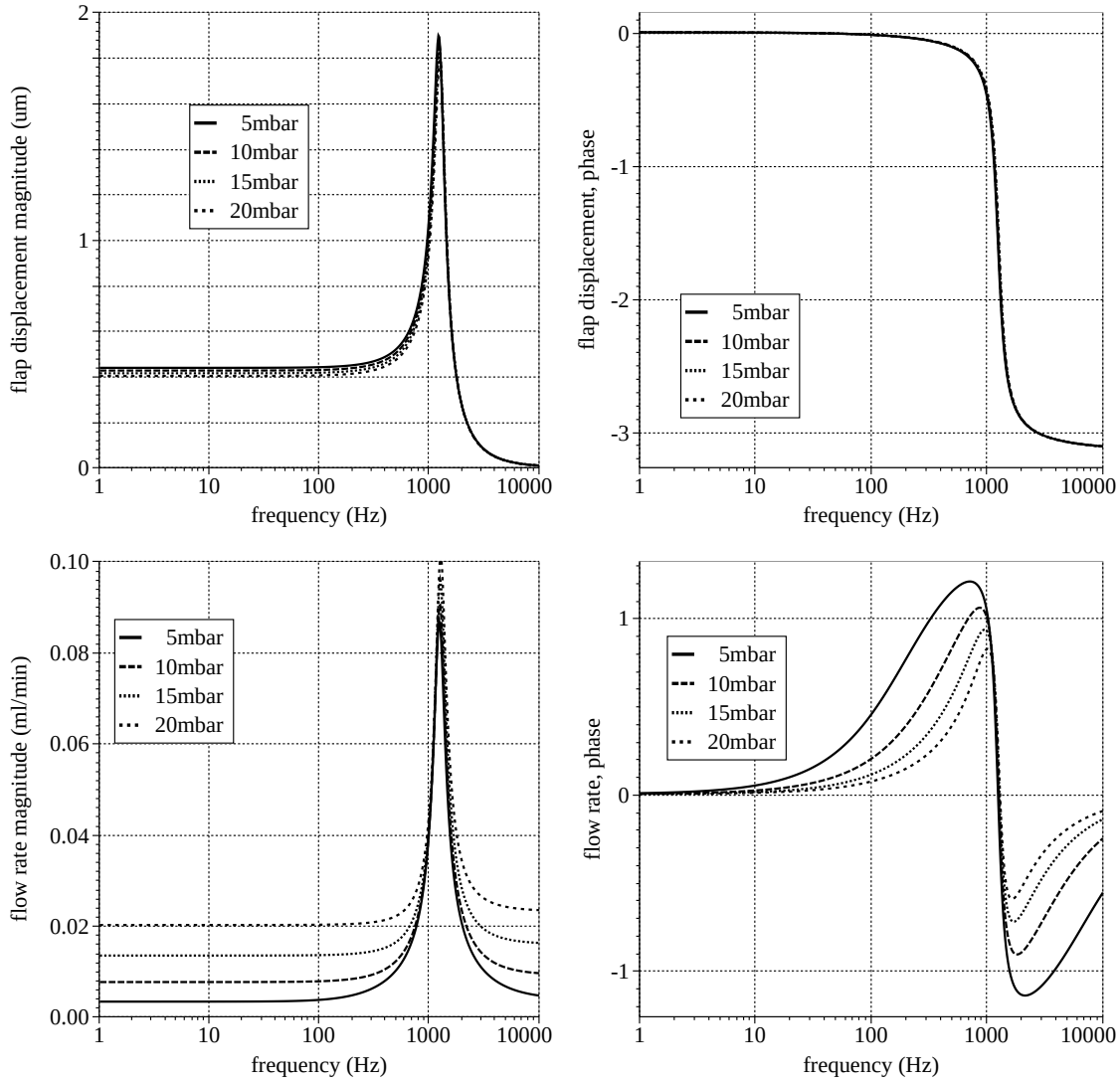

Fig. 5.18: Simulated small signal analysis of a flap valve. Shown are magnitude and phase of flap displacement and flow rate as a result of a sinusoidal pressure stimulus. Four different quasi-static pressure operating points are simulated, revealing weak nonlinearities in the displacement and strong ones in the flow rate.

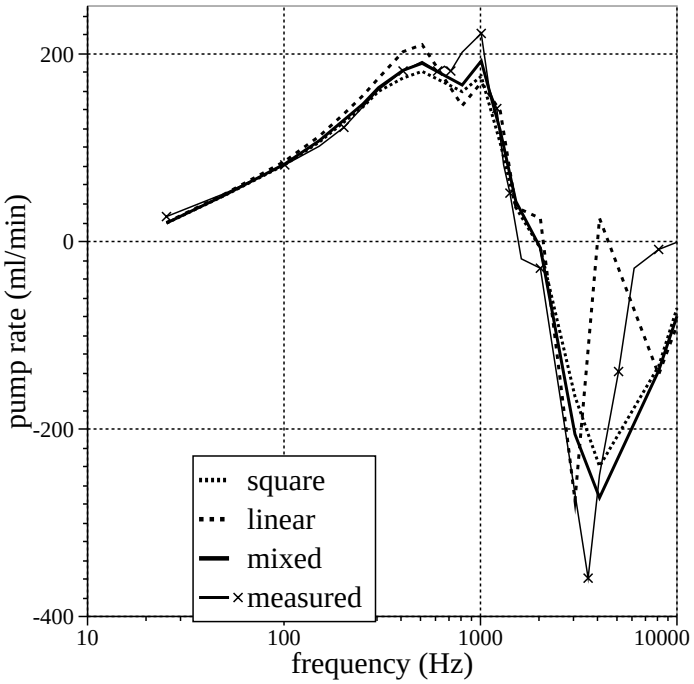

Fig. 5.19: Simulated pump rate for different damping properties of the valve flaps. As expected, the damping of the valve flap motion impacts mostly the pump operation at higher drive frequencies.

5.3 A micro-fluidic tube model

5.3.1 Introduction

Connecting tubes are an essential part of most fluidic systems. In various engineering disciplines and even in medicine, effort has been spent to investigate static and dynamic fluid flow phenomena in tubes [86, 87, 88, 89]. Of special interest are results from research for the medicine, because the fluid flow and pressure pulse propagation in tubes with compliant walls is investigated [90, 91, 72, 92, 93]. In mircrofluidic systems, the elasticity of the connecting tubes must also be considered.

In the recent years, investigations of fluidic flow through capillaries [94] and microchannels [95, 96, 97] have been published. They deal with static flow phenomena. Transient effects in tubes, however, can significantly impact the system performance. Accurate, yet simple tube models for system level simulation are therefore required.

5.3.2 The analytical model

The Navier-Stokes equation for incompressible fluids, using the notation in [98], reads as

$$\frac{\partial \vec{v}}{\partial t} + (\vec{v}\nabla)\vec{v} = -\frac{1}{\rho}\mathrm{grad}p + \nu\Delta\vec{v} \tag{5.9}$$

For systems exhibiting a cylindrical symmetry equation (5.9) can be rewritten as

$$\frac{\partial v_r}{\partial t} + v_r\frac{\partial v_r}{\partial r} + v_x\frac{\partial v_r}{\partial x} = -\frac{1}{\rho}\frac{\partial p}{\partial r} + \nu\Big(\frac{\partial^2 v_r}{\partial r^2} + \frac{\partial^2 v_r}{\partial x^2} + \frac{1}{r}\frac{\partial v_r}{\partial r} - \frac{v_r}{r^2}\Big) \tag{5.10}$$

$$\frac{\partial v_x}{\partial t} + v_r\frac{\partial v_x}{\partial r} + v_x\frac{\partial v_x}{\partial x} = -\frac{1}{\rho}\frac{\partial p}{\partial x} + \nu\Big(\frac{\partial^2 v_x}{\partial r^2} + \frac{\partial^2 v_x}{\partial x^2} + \frac{1}{r}\frac{\partial v_x}{\partial r}\Big) \tag{5.11}$$

Now we consider a tube with an inner diameter R_0. A cylindrical coordinate system is defined in such a way, that the x-axis is also the length axis of the tube, whereas r describes the distance from the x-axis (fig. 5.20). The tube is extensible, so that a pressure change $p = p_0 + \Delta p$ causes a change of the tube radius $R = R_0 + \xi$ and the lumen (inner cross sectional area) $S = S_0 + 2\pi R_0\xi$. For the latter the relation $\xi \ll R_0$ was used. A linear relation between pressure and radius change is assumed with a constant k describing the tube elasticity:

$$p(x, R_0) = p_0(x, R_0) + \Delta p(x, R_0) = p_0(x, R_0) + \xi(x)\rho \cdot k \tag{5.12}$$

We investigate the propagation of pressure waves inside the tube. The deviation is based on a few approximations and follows mainly the deviation of the equation for surface gravity waves in liquids [98]. Especially it was used that $\lambda \gg R_0$ and $\partial\vec{v}/\partial t \gg (\vec{v}\nabla)\vec{v}$. The latter means (as shown in [98]) that the wavelength λ of all pressure oscillations in the tube is large compared to the amplitude of the corresponding liquid motion. The

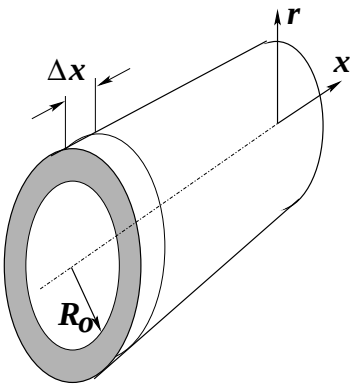

Fig. 5.20: Tube with inner diameter R_0 and a slice of the tube with the thickness Δx.

assumption that $\lambda \gg R_0$ implies that all radial derivatives $\partial/\partial r$ can be neglected. Then equation (5.10) can be dropped and equation (5.11) simplifies to

$$\frac{\partial v}{\partial t} = -\frac{1}{\rho}\frac{\partial p}{\partial x} + \nu\frac{\partial^2 v}{\partial x^2} \tag{5.13}$$

Using equation (5.12) to substitute p in equation (5.13) yields

$$\frac{\partial v}{\partial t} = -k\frac{\partial \xi}{\partial x} + \nu\frac{\partial^2 v}{\partial x^2} \tag{5.14}$$

The mass conservation law can be expressed as

$$\frac{\partial V}{\partial t} = -\oint_A \vec{v}\,\mathrm{d}^2\vec{r} \tag{5.15}$$

If the volume under consideration is a slice of the tube with the length Δx, then the volume is $S\Delta x$. The flow into the volume can only occur from the circular sides, but not from the periphery, and the surface integral can be written as $v(x)S(x) - v(x+\Delta x)S(x+\Delta x)$. Then equation (5.15) can be transformed in the following way, performing $\lim \Delta x \to 0$ in the second step and using $S = S_0 + 2\pi R_0 \xi$ in the third step.

$$\begin{aligned}
\frac{\partial(S\Delta x)}{\partial t} &= v(x)S(x) - v(x+\Delta x)S(x+\Delta x) \\
\iff \frac{\partial S}{\partial t} &= -\frac{\partial(Sv)}{\partial x} \\
\iff 2\pi R_0\frac{\partial \xi}{\partial t} &= -\frac{\partial}{\partial x}\Big(\pi {R_0}^2 v + 2\pi R_0\,\xi\,v\Big) \\
\iff \frac{\partial \xi}{\partial t} &= -\frac{\partial}{\partial x}\Big(\frac{R_0}{2}v + \xi v\Big)
\end{aligned} \tag{5.16}$$

Because $\xi \ll R_0$, equation (5.16) can be simplified to

$$\frac{\partial \xi}{\partial t} = -\frac{R_0}{2}\frac{\partial v}{\partial x} \tag{5.17}$$

A partial differentiation of equation (5.17) versus x and t results in the following equations:

$$-\frac{2}{R_0}\frac{\partial^2 \xi}{\partial t \partial x} = \frac{\partial^2 v}{\partial x^2} \tag{5.18}$$

$$-\frac{2}{R_0}\frac{\partial^2 \xi}{\partial t^2} = \frac{\partial^2 v}{\partial x \partial t} \tag{5.19}$$

Substituting equation (5.18) into equation (5.14) gives

$$\frac{\partial v}{\partial t} = -k\frac{\partial \xi}{\partial x} - \nu\frac{2}{R_0}\frac{\partial^2 \xi}{\partial x \partial t} \tag{5.20}$$

Partial differentiation of equation (5.20) versus x and sub-sequential usage of equation (5.19) to eliminate v in the resulting equation yields

$$\begin{aligned} \frac{\partial^2 \xi}{\partial t^2} &= \frac{R_0 k}{2}\frac{\partial^2 \xi}{\partial x^2} + \nu\frac{\partial^3 \xi}{\partial t \partial x^2} \\ \Longleftrightarrow \quad \frac{\partial^2 \xi}{\partial t^2} &= \frac{\partial^2}{\partial x^2}\Big(\frac{R_0 k}{2}\xi + \nu\frac{\partial \xi}{\partial t}\Big) \end{aligned} \tag{5.21}$$

By using equation (5.12), the following expression for the pressure propagation in a tube can be derived

$$\frac{\partial^2 p}{\partial t^2} = \frac{\partial^2}{\partial x^2}\Big(\frac{R_0 k}{2}p + \nu\frac{\partial p}{\partial t}\Big) \tag{5.22}$$

The equation describes the propagation of a damped pressure wave along the tube. The dispersion relation reads as

$$\frac{\omega}{\lambda} = -\frac{\lambda\nu}{2}i \pm \sqrt{\frac{R_0 k}{2} - \frac{\lambda^2\nu^2}{4}} \tag{5.23}$$

It is worthwhile to note that both the propagation velocity and the damping depend on the tube elasticity and that they are a function of the wavelength λ.

5.3.3 The numerical model

We will show now that the problem of the propagation of a voltage wave in the circuit given below is equivalent to the fluidic problem described in section 5.3.2 above. Each elementary cell is a representation of a slice of the tube with a thickness Δx. The resistor R_1 represents the static flow resistance of such a slice, L accounts for the inertia of the fluid, whereas C models the elasticity of the tube and possibly also the local compressibility of the fluid. R_2 models local damping effects due to the fluid viscosity and avoids non-physical local oscillations in the model. This resulting model of a tube actually is

Fig. 5.21: Equivalent circuit model (or finite network model) of a tube. Each R_1LCR_2 - element represents a slice of the tube with a certain thickness Δx.

a one-dimensional finite network model, comparable to other such models described in chapter 3.2.

According to [99], an equivaqlent numerical representation of the above model of a tube slice could be expressed as follows:

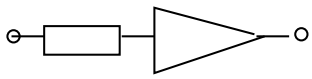

R1 **delay**

Whether or not this second realization is more efficient for numerical simulation, depends sensitively on the actual implementation in the used simulation tool.

The following equations for the voltage and current in an elementary cell of the presented circuit can be gathered from the Kirchhoffian network rules.

$$u(x) - u(x+\Delta x) = j(x)R_S + L\frac{\partial j(x)}{\partial t} \tag{5.24}$$

$$j(x) - j(x+\Delta x) = C\frac{\partial}{\partial t}\Big(u(x+\Delta x) - R\big(j(x) - j(x+\Delta x)\big)\Big) \tag{5.25}$$

The transformation $\Delta x \to 0$ allows to write

$$\lim_{\Delta x \to 0} \frac{u(x) - u(x+\Delta x)}{\Delta x} \to \frac{\partial u(x)}{\partial x}$$

$$\lim_{\Delta x \to 0} \frac{j(x) - j(x+\Delta x)}{\Delta x} \to \frac{\partial j(x)}{\partial x}$$

and equation (5.24) and (5.25) can be rewritten as

$$-\frac{\partial u(x)}{\partial x} = j(x)\mathcal{R}_S + \mathcal{L}\frac{\partial j(x)}{\partial t} \tag{5.28}$$

$$-\frac{\partial j(x)}{\partial x} = \mathcal{C}\frac{\partial u(x)}{\partial t} + \mathcal{R}\mathcal{C}\frac{\partial^2 j(x)}{\partial t \partial x} \tag{5.29}$$

The terms $R_S/\Delta x, R\Delta x, L/\Delta x$ and $C/\Delta x$ are replaced by the corresponding densities $\mathcal{R}_S$, $\mathcal{R}, \mathcal{L}$ and $\mathcal{C}$, respectively. If the frequency ω is high enough, then $R_S \ll L\omega$, and therefore the term in (5.28) which contains R_S, can be dropped. Partially differentiating (5.28) versus x and (5.29) versus t, and eliminating $j(x)$ in both equations yields

$$\frac{\partial^2 u}{\partial t^2} = \frac{\partial^2}{\partial x^2}\Big(\frac{1}{\mathcal{L}\mathcal{C}}u + \frac{\mathcal{R}}{\mathcal{L}}\frac{\partial u}{\partial t}\Big) \tag{5.30}$$

A comparison to equation (5.22) shows, that the two problems are equivalent and that the following correspondences hold true

$$\begin{aligned} u &\to p \\ j &\to w \\ \frac{1}{\mathcal{C}\mathcal{L}} &\to \frac{R_0 k}{2} \\ \frac{\mathcal{R}}{\mathcal{L}} &\to \nu \end{aligned}$$

Therefore the given electrical circuit can be used to model the fluidic problem. The approximation used above, that $R_S \ll L\omega$, is good for the micro-fluidic case of very small

tube radii, because R_S, representing the static laminar flow resistance, is proportional to the tube radius R_0, but $\mathcal{L} \propto 1/R_0^2$, and subsequently $R_S \ll L\omega$ for very low frequencies already. The parameters for the electrical analogon can be related to fluidic parameters in the following way

$$\begin{aligned} \mathcal{C} &\propto \frac{2R_0}{k} \\ \mathcal{R} &\propto \nu \\ \mathcal{L} &\propto \frac{1}{R_0^2} \end{aligned}$$

The presented circuit is very similar to an electrical transmission line model and can be implemented in an analog network simulator, using numerically efficient ways as presented in [99], e.g.

The numerical implementation of tube models into an analog network simulator can alternatively be performed using VHDL-AMS. This has, beside others, the advantage of describing the tube in terms of purely fluidic variables, thus avoiding the translation from fluidic into electrical variables and vice versa. All the other fluidic system components can be described in a similar way, as described in [100], thus yielding a consistent macro-model for the entire system.

5.3.4 Simulation results

If a step-like increase in pressure is applied to one side of a tube with compliant walls, the pressure wave travels through the tube with a velocity, which is much smaller than the speed of acoustic waves (Fig. 5.22). The same holds true for a pressure pulse. At the open end of the tube (constant pressure reservoir) the pulse is being reflected with a phase shift of 180^o (Fig. 5.22).

The performed AC analysis of the tube response to an harmonic pressure stimulus is shown in Fig. 5.23. The appearance of standing waves as well as the increased damping with higher frequencies is clearly visible.

The impact of transient effects in tubes on the behavior of a micropump as presented in [100] is shown in Fig. 5.25. Some fluctuations of the pump rate with increasing drive frequency can be explained by standing wave effects in the tubes. It should be noted here, that not only the total length of inlet and outlet tubes, but also the relation between both values is important. A possible explanation will be given in section 5.4.4.

5.3.5 Conclusions

A model for tubes with compliant walls could be derived, which is simple, intuitive and a natural extension of the familiar RLC-model. The structure of this model is quite similar to a model of lossy transmission lines, thus making advanced numerical algorithms employable, which have been developed for VLSI-interconnects [99]. It simulates very efficiently, thus allowing to model large fluidic systems.

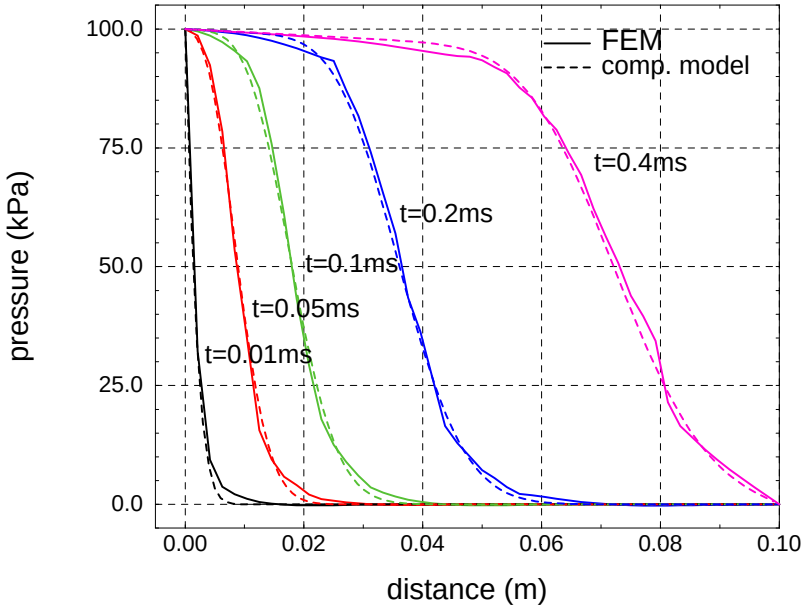

Fig. 5.22: A steplike pressure change from 0 to 1mbar is applied to the tube. The resulting pressure distribution along the tube is shown at different time points, thus illustrating the propagation of the pressure change.

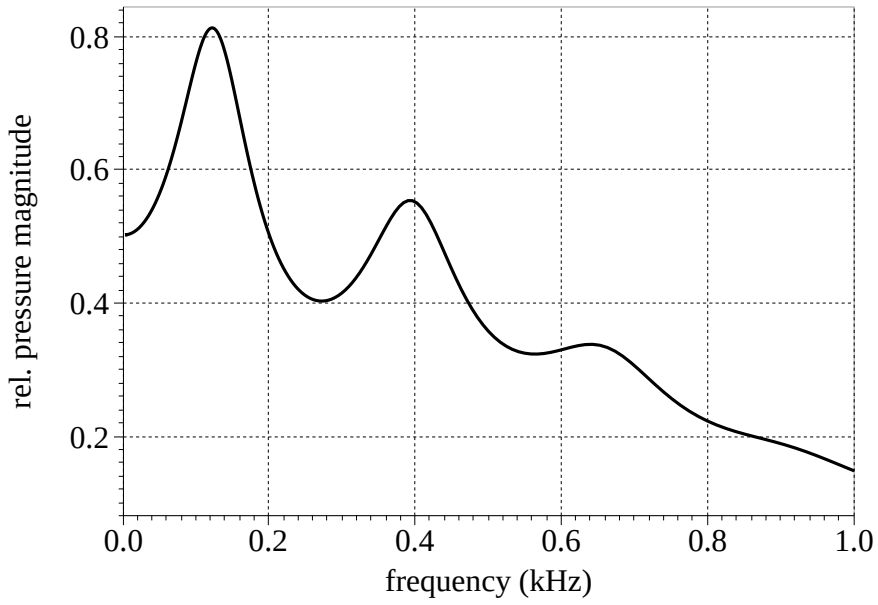

Fig. 5.23: Performing an AC analysis of the tube behavior shows a significant damping of the second resonance point at 390Hz.

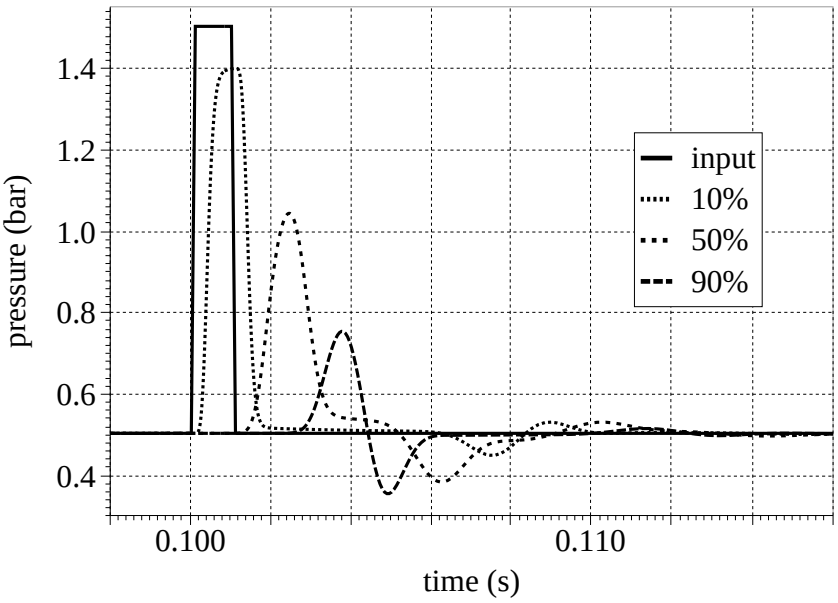

Fig. 5.24: A pressure pulse from 0.5 to 1.5bar is applied to the tube. The resulting pressure oscillations at a position of 10, 50 and 90% of the full tube length are shown.

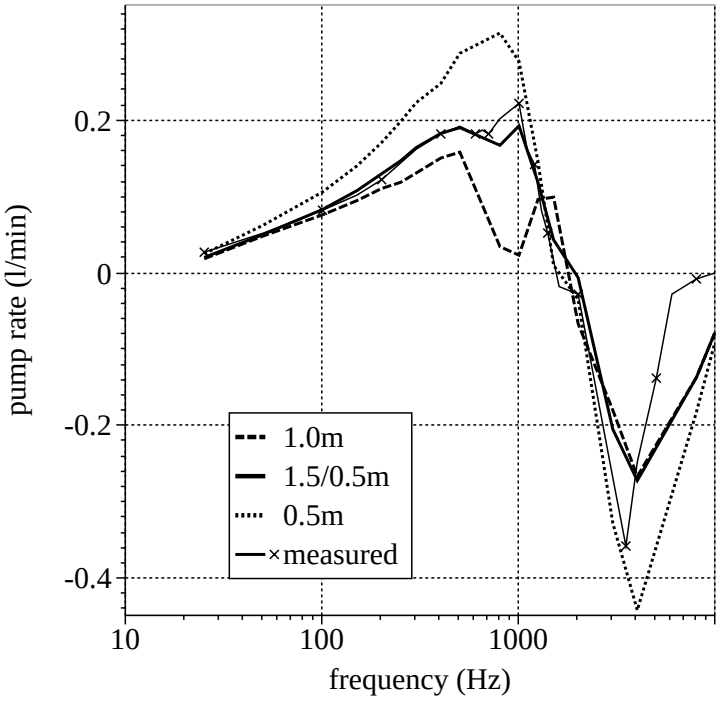

Fig. 5.25: Simulated pump rate vs. driving frequency for three different length of the connecting tubes.

5.4 A micro-fluidic system model

5.4.1 Introduction

Micro-fluidic systems have various applications, e.g. in medicine [101], in biology and chemistry as part of microanalysis systems etc. [102, 77, 103, 104, 105]. Various actuation prinziples are known: piezoelectric [106], thermo-pneumatic [107], electromagnetic and others. At the Fraunhofer Institute of Solid State Technology (IFT) there was developed an electrostatically actuated micropump [80]. For an analysis of the system operation and in order to perform design optimization, an dedicated software tool PUSI was developed at the IFT [108]. It will be shown here that the modeling of the micropump using compact models for its constituent parts yields the same results but is not restricted to the given micropump and does not require the effort of maintaining a special purpose simulator.

After explaining the operational principle of the micropump, the compact models of its parts will be described, and finally the results of the system simulation will be presented.

5.4.2 Construction and operational principle

The micropump described in [60] consists of a pump chamber with an electrostatically displaced membrane as driving element, an inlet and an outlet passive check valve, and externally attached connecting tubes (Fig. 5.26). The membrane is separated from a solid counter-electrode by an air-gap and an isolating oxide, which prevents electrical short circuiting when the membrane touches the counter-electrode. Construction, operating principle and compact model of an electrostatically actuated membrane have been described in section 3.4.2

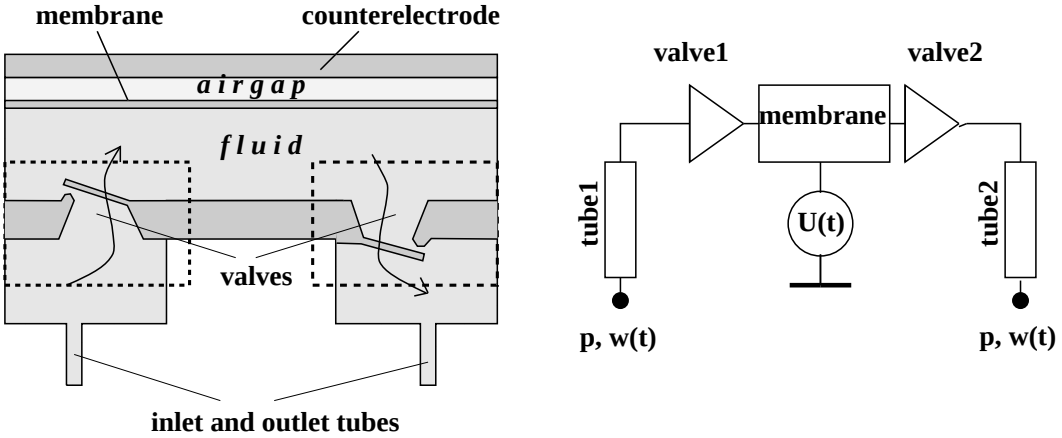

Fig. 5.26: Schematic view of the micropump (left) and its macro-model (right), consisting of an electrostatically actuated membrane and the voltage supply circuitry, the valves and the connecting tubes. The dotted line indicates the interfaces between the valve compact model region, pump chamber and connecting tubes, respectively.

During operation, a voltage is applied between membrane and counter-electrode. The resulting attractive force between the two electrodes causes under-pressure in the pump chamber, thus forcing the inlet valve to open. When the voltage is switched off again, the membrane gets released from the counter-electrode, causing a pressure increase in the chamber and forcing the outlet valve to open and the inlet valve to close. In order to obtain a large membrane deflection and, consequently, a large pumped volume, the applied voltage must be high enough to make the membrane touch the counter-electrode.

To drive the pump, a square wave voltage is applied between membrane and counter-electrode. The pump rate can be controlled by the frequency of the input voltage. An application of micro-pumps in micro-dosing systems requires a precise control of the pumped volume. Therefore, to design such systems, an accurate dynamic model of the pump operation is required.

5.4.3 Compact models of the micropump elements

For the analysis of the system operation, an appropriate set of dynamic variables has to be determined, and the entire system has to be decomposed into elementary parts, which then will be described by compact models. The natural set of conjugate variables for the merely fluidic system components consists of pressure and mass flow rate. For the application considered, the fluid can be assumed to be incompressible. Therefore we may use the volume flow rate instead of the mass flow rate. The system is partitioned into the following parts: tubes, valves, and pump chamber with membrane drive. The interfaces which separate the valves from the membrane are shown in Fig. 5.26. The assumptions underlying this selection of the interfaces are, corresponding to the considerations in section 2.3.1, as follows: The pressure distribution in the pump chamber is spatially uniform, and the flow rates through the interfaces (i.e. the surface integrals of the flow density along the interfaces) are adequate to describe the operation of the system parts. This implies that all local fluid redistributions inside the pump chamber occur ”instantaneously” on the time scale of interest (i.e., quasi-statically), so that the uniform pressure condition is maintained all the time. Fig. 5.26 displays the resulting equivalent generalized Kirchhoffian network.

5.4.4 Simulation of the micropump operation

The response of the pump to a single 200V voltage pulse is shown in the left part of Fig. 5.27. The results are in good agreement with the measured data given in [80]. In particular, we find evidence for pressure oscillations arising from the inertia of the fluid in the tubes. It is important to note that the system behavior is strongly influenced or even dominated by the ”parasitics”, i.e. the inertia of the fluid and the elasticity of the tube walls.

In the right part of Fig. 5.27, the flow rate and the pumped volume (time integral of flow rate) are shown, with the pump operated at 200V and 500Hz. It takes approximately 50ms for the pump to reach the full pump rate. The reason is as follows: During the first phase of a pump cycle, only a limited amount of liquid can be drawn into the pump

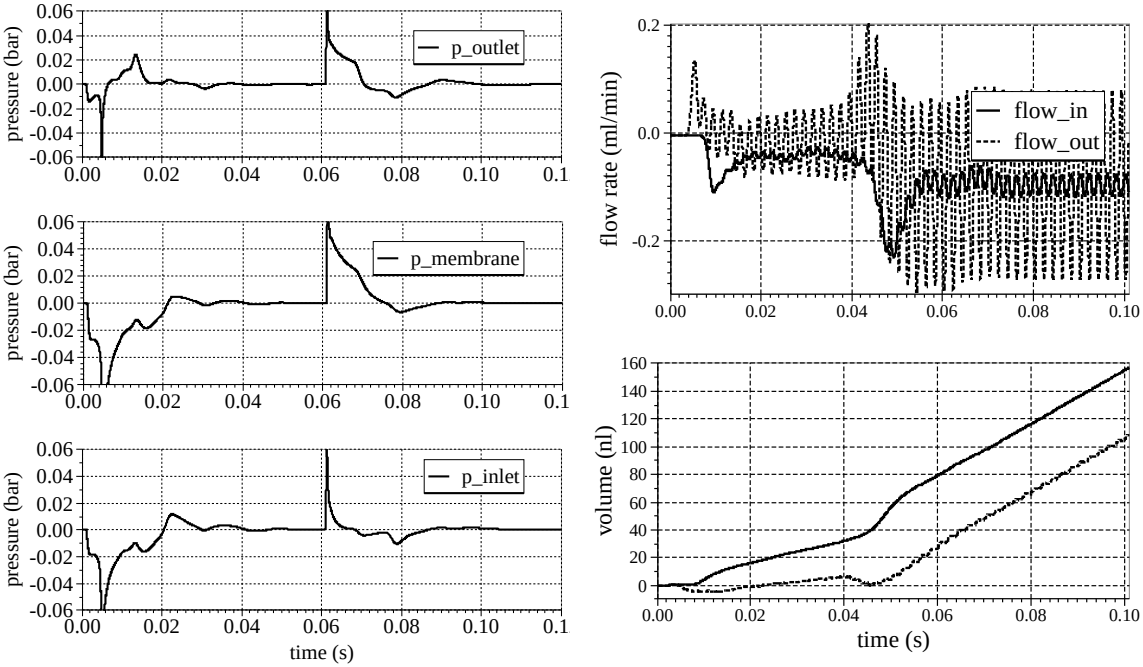

Fig. 5.27: Transient pulse response of the pump. The pressure at the inlet, at the outlet and in the pump chamber near the membrane is shown in the left figure, with a single pulse of 200V applied from 0 to 60ms. The flow rate and pumped volume are displayed at the right, with the pump pulsed at 200V and 500Hz.

chamber. The inlet valve and the inlet tube limit the flow rate. If the frequency is higher than a certain value (approx. 100Hz in the considered case), the liquid change in the pump chamber is too small to allow the membrane to touch the counter-electrode. In the second phase of a pump cycle, the limited flow through outlet valve and tube does not allow the membrane to reach its equilibrium position. What finally happens is an oscillation of the membrane around an median position. It takes a couple of pump cycles for the membrane to reach this median position. The value of this median position sensitively depends on the ratio of inlet to outlet flow resistance. Because the electrostatic force, and therefore the generated pressure in the pump chamber, strongly depends on the distance between membrane and counter-electrode, the pump rate itself is very sensitive to changes in the connecting tubes.

The pump rate was investigated as a function of the driving frequency. The increase of the pump rate with increasing frequency is much weaker than the theoretical linear dependence (Fig. 5.28). The main reason is the reduced pump stroke for higher frequencies, as described above.

The effect of reverse pumping, reported in [60], could be correctly reproduced (Fig. 5.28). It turned out to be caused by the phase shift between the pressure in the pump chamber due to the applied voltage and flap displacement. That is illustrated in Fig. 5.29. At a frequency below the resonance of the valve flap, pressure and flap displacement are in phase and, therefore, also the resulting flow is in phase to the pressure. At a frequency well above the resonance of the flap, the phase shift between pressure and flap displacement increases (see Fig. 5.18).

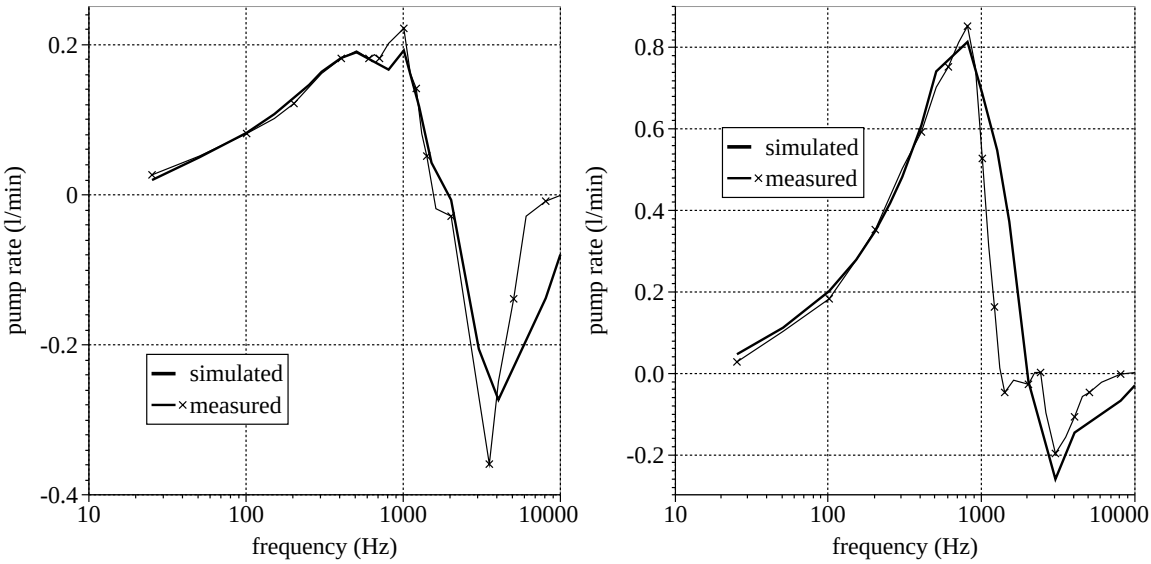

Fig. 5.28: Frequency-dependent pump rate of a micropump with a 3μm (left) resp. 5μm gap width (right) of the drive membrane. In both cases the same set of fitting parameters for the membrane model was used.

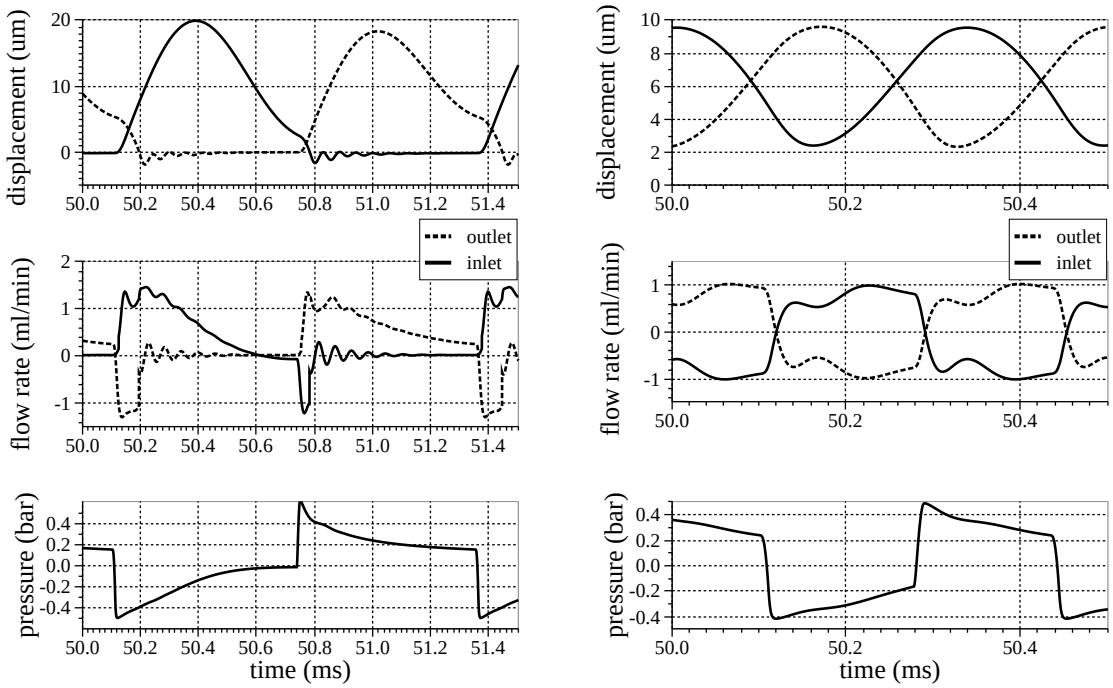

Fig. 5.29: Transient simulated flap displacement and flow rate at inlet and outlet valve and mean pressure in the pump chamber. The pump is operated near the fundamental resonance frequency of the valve flap (left) or above the resonance frequency (right). A single pump cycle is shown in both cases.

Also the flow rate exhibits a large phase shift compared to the applied pressure. The resulting net flow becomes negative, i.e. the pump works in reverse direction.

5.4.5 Conclusions

We have demonstrated that all constituent parts of a micropump can be modeled on the base of a description in VHDL-AMS. Therefore, the resulting macro-model of the entire microsystem can easily be passed to any conventional electronic circuit simulator, yielding quick and accurate calculations of the pump operation.

All the typical effects, which were found in measured characteristics and previously analyzed using a special tool exclusively dedicated to micro-pumps [80], could be obtained here as well in a much more general context and approach [109].

Following our methodology of describing and implementing models on the base of VHDL-AMS [100] makes it possible to simulate any micro-fluidic component by the use of any system simulator which is capable of understanding VHDL-AMS.

As a consequence and future perspective, the non-electrical parts as well as the electronic circuitry in a microsystem may be simultaneously simulated using a uniform and consistent description language and CAD environment, thus allowing us the easy design and optimization of even complex microsystems [110].

5.5 Electro-mechanical system model of a gyroscope

5.5.1 Introduction

Micromachined gyroscopes are very attractive: due to their small dimensions and low weight, due to the possible close integration with control electronics, forming a complete system on a chip, and due to their potential of cheap mass production. The draw-backs are the dimensional inaccuracy due to production tolerances and the small noise margin due to the small seismic mass [111]. Especially the close integration with the control electronics creates a strong need to simulate mechanical and electronical parts simultaneously on system-level [112], including process fluctuations and noise.

Now, the macro-model of a gyroscope will be presented. The gyroscope was developed at Infineon Technologies AG and at the University Paderborn [113]. It serves as a test case to demonstrate a consequently physically based, analytical modeling approach.

The derived compact models, which establish the gyroscope macro-model, have physical, geometrical and technological input parameters. Very few fit parameters are introduced to improve the model accuracy, where too crude approximations in the analytical description had to be made. Still, these fit parameters are closely related to the physical effect, which approximation they have to improve. That made it straight-forward to extract them from data based on FEM-simulations.

It will be shown that the resulting macro-model can be used to analyze the impact of technological variations on system properties, making it possible to use this modeling approach for yield/failure analysis, statistical modeling etc.

The compact models were coded in VHDL-AMS and simulated in Spectre and in TITAN. It will be shown, how the gyroscope macro-model works together with a real electric circuitry, namely the control circuit for the electrostatic comb drive.

5.5.2 Construction and operational principle

When a rigid body is moving in a rotating (non-inertial) system, it experiences inertial forces, also known as Coriolis-force:

$$\vec{F}_c = m \cdot \vec{v} \times \vec{\omega} \tag{5.31}$$

This effect can be used to detect and measure rotational motions.

In the presented case of a surface-micro-machined realization of a gyroscope, a polysilicon layer is deposited, structured and then released. It is attached to the silicon bulk due to two springs (Fig. 5.35) in such a way, that it can be tilted around the x and z axes. Rotation around the y-axis, as well as any translatory motion is unwanted and should be suppressed by choosing a corresponding aspect ratio of the suspension springs. It turns out that this is not possible, but during normal operation of the gyroscope only the two motions mentioned first are stimulated. Therefore, only those are considered in the compact model.

The movable parts are covered by a polysilicon cap. Inside this encapsulation the air

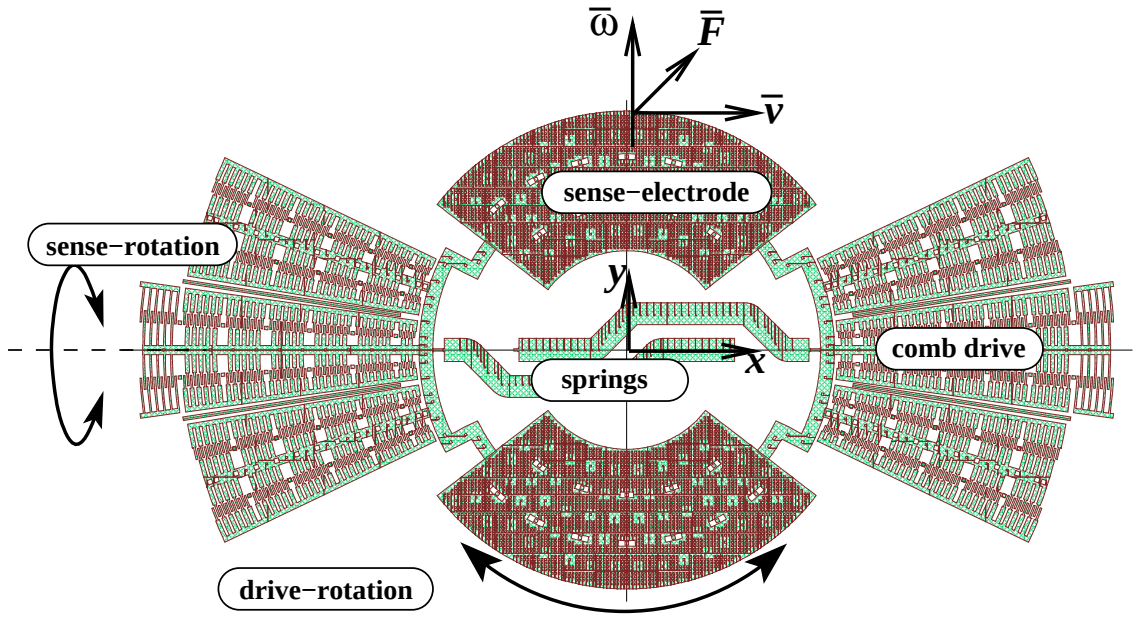

Fig. 5.30: Layout of a gyroscope with an electrostatic comb drive and capacitive signal readout.

pressure is reduced to minimize air damping effects. A high Q-factor is needed to achieve sufficient sensitivity of the gyroscope. The polysilicon cap as well as the bulk silicon underneath the sense electrodes are structured in such a way, that they form a set of electrical plate capacitors with the sense electrodes.

The polysilicon structure, acting as proof mass, is driven into a rotational oscillation around the x-axis by the forces created in electrostatic comb drives. If the system is rotating around the y-axis, the resulting inertial forces cause a torsion around the x-axis, which then is detected capacitively. Fig. 5.30 shows the layout and a sketch of the operational principle.

To achieve a large sensitivity while still maintaining CMOS-compatible drive voltages, the increase in the oscillation amplitude due to mechanical resonance effects is exploited. Therefore, the frequencies of drive and sense oscillations need to be controlled during the device operation. This leads to manifold interactions between control electronics and sensing element, thus creating a strong need for coupled simulations on system level.

5.5.3 The compact models

The development of physically based compact models is strongly motivated, because the resulting macro-model of the gyroscope must reflect all relevant physical effects, including the dependence from some important process variations as polysilicon layer thickness, e.g.

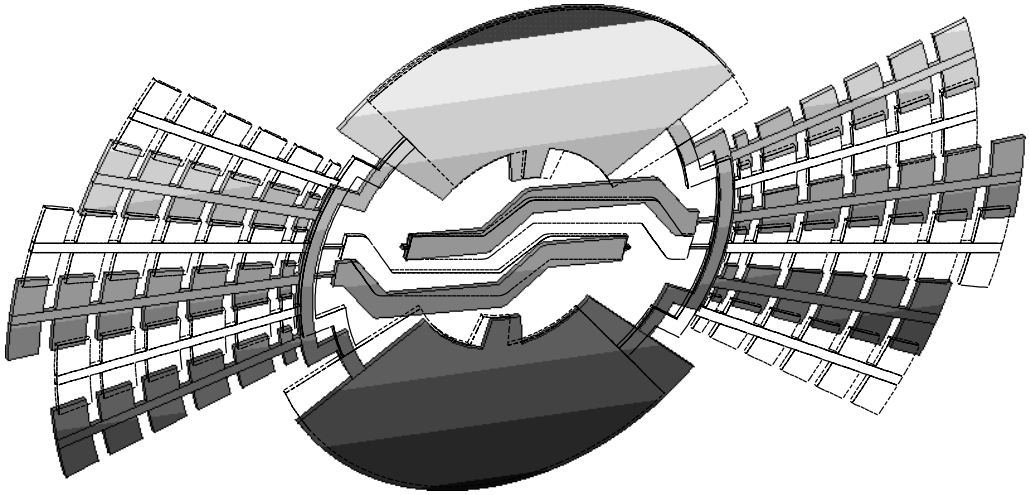

Fig. 5.31: Modal analysis of the gyroscope: The first eigenmode is an in-plane rotation around the z-axis and is used as drive mode.

a) Springs and seismic masses

The mechanical properties of the springs are modeled using the well known formulae for the bending and torsion of beams. Special care needs to be taken because the pivotal point for the drive motion is different from the clamping point. All the other parts of the gyroscope are assumed to be rigid. So they act as seismic mass only. A modal FEM-based analysis justifies this approximation: the five lowest natural frequencies stem from bending and torsion of the springs, with neglectable deformations of the other parts of the gyroscope. Since during normal operation of the gyroscope only the lowest two eigenmodes are excited, which are a in-plane rotational oscillation (drive mode, Fig. 5.31) and a rotational oscillation along the x-axis (sense mode, Fig. 5.32), only those two modes are considered in the compact model. The higher modes are not modeled, because for ideally shaped suspension beams and fully symmetrical seismic masses no mechanical mode coupling occurs.

The input parameters for the resulting compact model are only geometrical data from the layout, material parameters and technological data (layer thickness, e.g.). The simulated device behavior corresponds very well to results from FEM-simulations, as shown in a table of resonance frequencies (tab. 5.1). In the FEM-simulations, a modal analysis was

	FEM 2D	FEM 3D	CM
drive	7.3kHz	7.0kHz	7.2kHz
sense	8.9kHz	9.2kHz	9.4kHz

Tab. 5.1: Mechanical resonance frequency of the gyroscope in drive and sense directions. 2D-FEM simulations (shell elements), 3D-FEM simulations and the CM results are compared to each other.

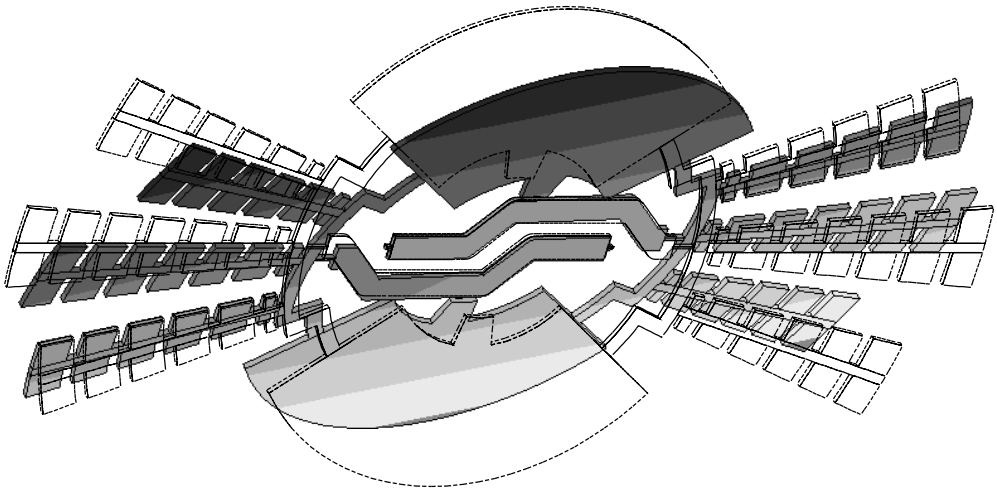

Fig. 5.32: Modal analysis of the gyroscope: The second eigenmode is an out-of-plane rotation around the x-axis and is used as sense mode.

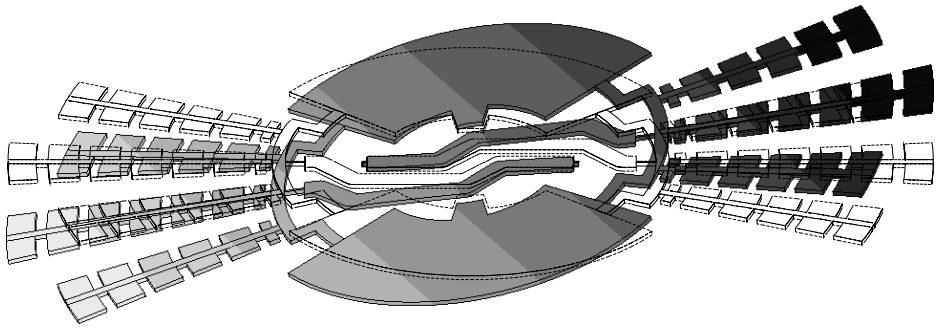

Fig. 5.33: Modal analysis of the gyroscope: The third eigenmode is an out-of-plane rotation around the y-axis.

performed, using either 2D-shell-elements or 3D-elements. For the compact model, a small signal analysis was performed. The correspondence between FEM and CM is very good, making the introduction of any fit-parameters superfluous.

b) Electrostatic comb drive

Since the photolithographic tolerances are much smaller than the minimum line spacing, the comb fingers can be designed to have steps (see Fig. 5.36). The reduced gap between the comb fingers increases the electrostatic attracting force. The resulting nonlinearities in the driving force of the gyroscope are of no importance, because it is operated in resonance and is only weakly damped.

Two effects of the comb drive are modeled:

1. the torque $M(\phi, V)$ due to the electrostatic forces as a function of the applied voltage and the angular position.

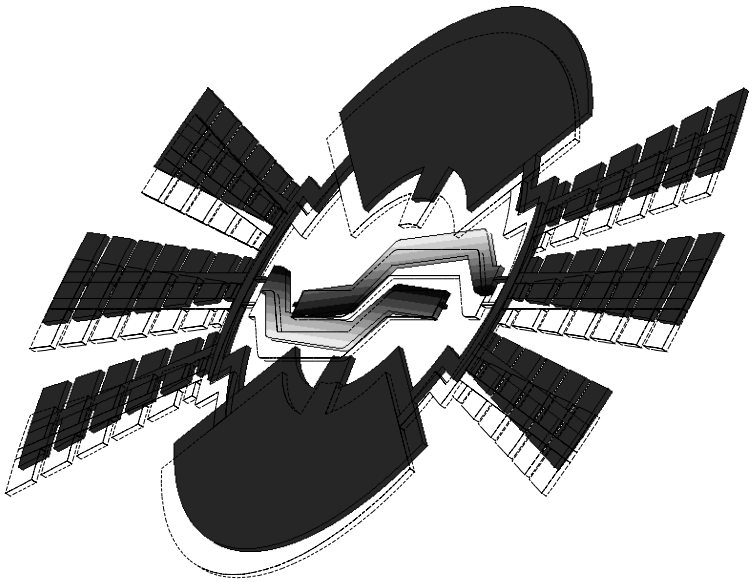

Fig. 5.34: Modal analysis of the gyroscope: The fourth eigenmode is an in-plane translation in the y-direction.

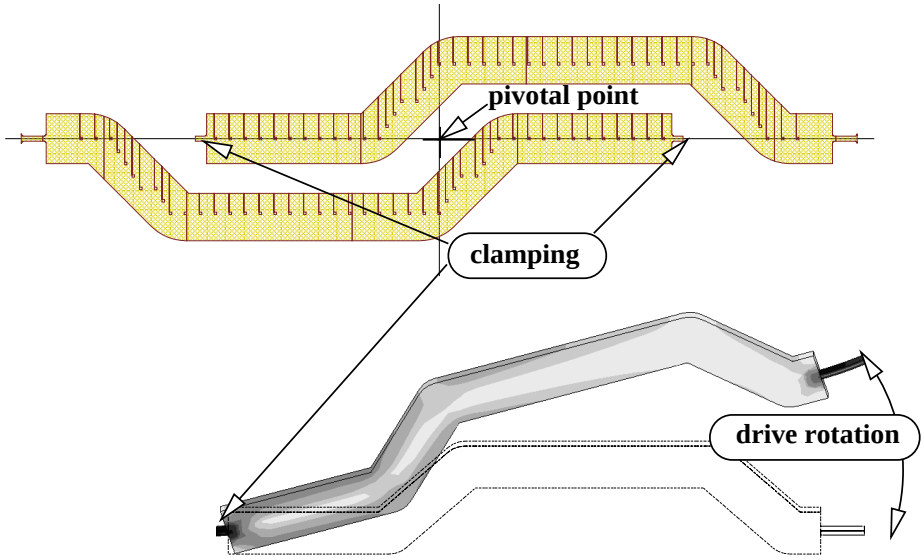

Fig. 5.35: Layout of the springs and FEM–model.

2. the electric capacitance $C(\phi)$ between the fingers as a function of the angular position.

Two regions of operation are considered: the comb fingers are in such a position that either the large or the small gap is effective. In either case a homogeneous electric field between the fingers is assumed. Stray fields at the edges are neglected as well as field inhomogeneities in the transition region between large and small gaps.

The abrupt change in the model for torque and capacitance at the angle ϕ_t, when the comb drive is moving from a large gap position into a small gap position, is finally smoothed

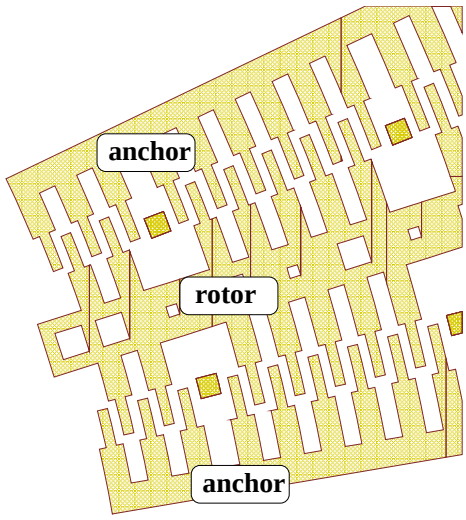

Fig. 5.36: Layout of an electrostatic comb drive.

out by an *tanh*–function:

$$M(\phi) = M_0 + M_1 \cdot tanh(p_{fit}(\phi - \phi_t)) \quad (5.32)$$

$$C(\phi) = C_0 + C_1 \cdot tanh(p_{fit}(\phi - \phi_t)) \; . \quad (5.33)$$

Here, a fit-parameter p_{fit} is introduced into the model. It models how smooth the transition is. This fit-parameter effects only a limited operation region, is physically transparent and can, therefore, easily be extracted from a comparison to measured or FEM–simulated data. Fig. 5.37 shows the result of a parameter extraction performed in the parameter extraction tool UTMOST [69]. The electric capacitance as a function of the angular position is presented in Fig. 5.38. The compact model code is shown in appendix C.

The damping effects of the drive motion are mostly related to slip flow [114, 115] and require large modeling efforts. Because in the early design phase no measurements for model calibration have been available yet, a fairly simple model is used to describe the damping, adopted from [98].

c) Sense electrodes

Structured polysilicon electrodes underneath the sense electrodes, the sense electrodes themselves and structured top electrodes, additionally serving as sealing cap, form a pair of differential capacitors.

Because of the large aspect ratio between the lateral dimensions and the gap distance between the sense electrode and top and bottom electrodes, it is well justified to use a homogeneous field approximation to model the electrostatic forces as well as the electric capacitances.

When a voltage is applied between the sense electrode and the top and bottom electrodes, the resulting electrostatic forces cancel each other out. If however the sense electrode is tilted by an angle ϕ (see Fig. 5.39), then, because of the $1/d^2$ dependence of the electrostatic force, the forces from top and bottom electrodes become different and the sense

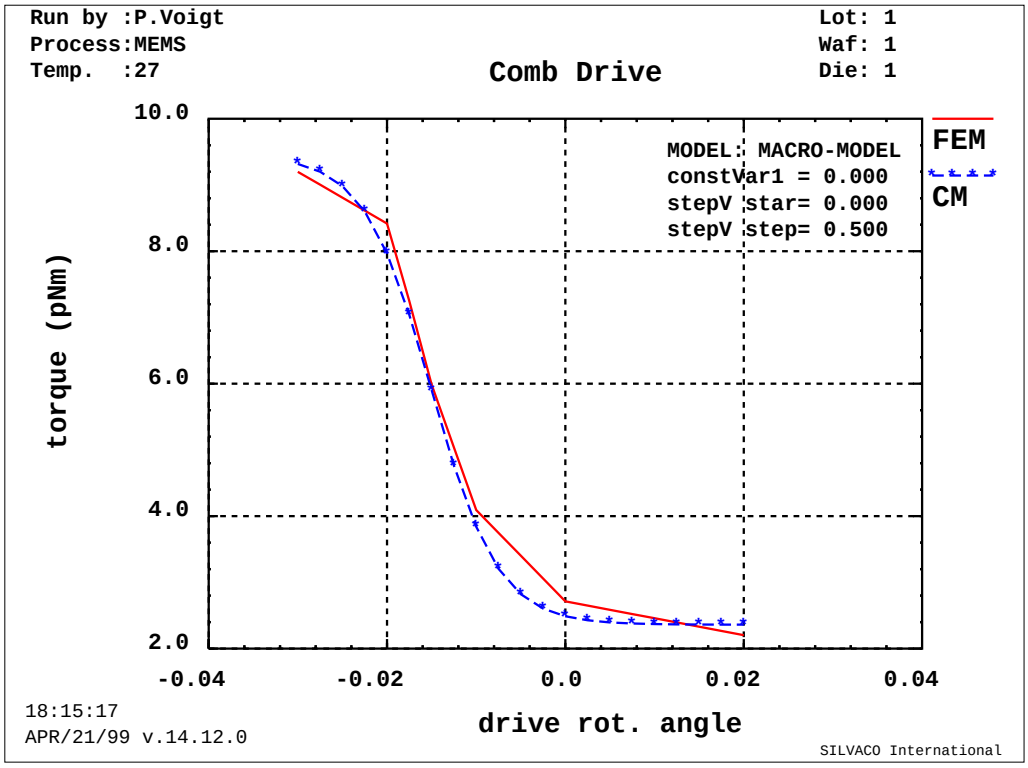

Fig. 5.37: Static characteristics of an electrostatic comb drive: torque vs. angular position. A parameter extraction in UTMOST was performed to fit the compact model simulated curve (dashed line) to the FEM–simulated curve (solid line).

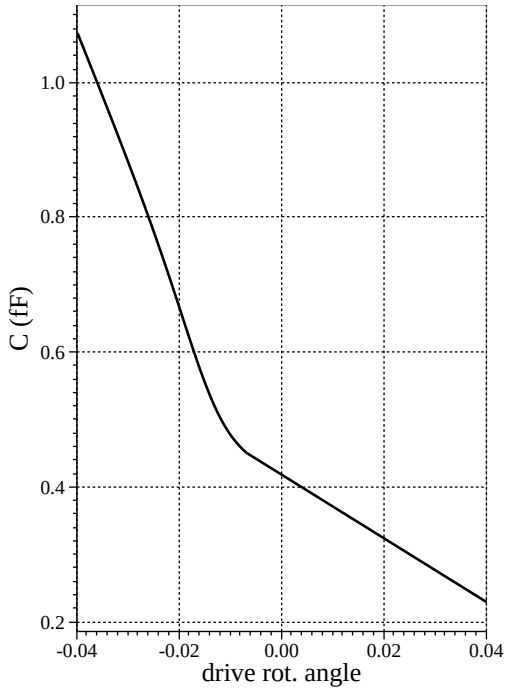

Fig. 5.38: Simulated static characteristics of an electrostatic comb drive: capacitance vs. angular position.

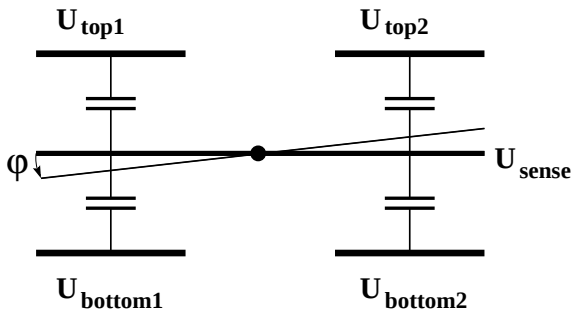

Fig. 5.39: Schematic view of the differential capacitors formed by the movable sense electrode and the bottom and top electrodes.

electrode experiences a torque which has the opposite direction than the restoring torque of the mechanical springs. This way the effective spring constant and thereby the resonance frequency of the sense motion can be reduced by applying a voltage.

The damping effects of the sense motion are mainly caused by squeeze film damping. Because the sense electrode is perforated densely, and the oscillation amplitude is low, an additional 'air spring' due to compression [49, 45, 116] can be neglected. A very simple damping term is used. To improve the modeling of damping effects, the incorporation of advanced damping models [51], which include the effects of etch holes in membranes, is possible.

5.5.4 The modeled system behavior

In this section it is demonstrated, that physical effects which are relevant to the operation of the gyroscope, are reproduced by the developed model.

When the gyroscope experiences a steplike change in torque in sense direction, it is moving into a new equilibrium position, performing a few damped oscillations (Fig. 5.40). An voltage applied to top and bottom electrodes reduces the effective spring constant, thus leading to an increased deflection due to the same torque and to a lower frequency of the oscillations. Both effects can be found in Fig. 5.40.

Those effects can be analyzed more in detail by performing an AC small signal analysis, as shown in figures 5.41 and 5.42. The quadratic dependency of the resonance frequency on the applied voltage can clearly be seen, as well as the typical resonance curves for the magnitude and phase angle.

In order to maximize the sensitivity of the gyroscope, while maintaining the CMOS compatibility of the drive voltage for the comb drive, the drive frequency is tuned to the mechanical resonance frequency, thus maximizing the oscillation amplitude. Due to the tolerances of the manufacturing process the resonance frequency cannot be predetermined, but has to be measured by the control electronics. Either phase and amplitude information are available for this purpose.

The resonance effect is used for the sense motion also. Since the torque in sense direction due to a Coriolis force depends on the drive motion (see equation (5.31)), the sense resonance frequency needs to be shifted to the drive frequency. Because of technological

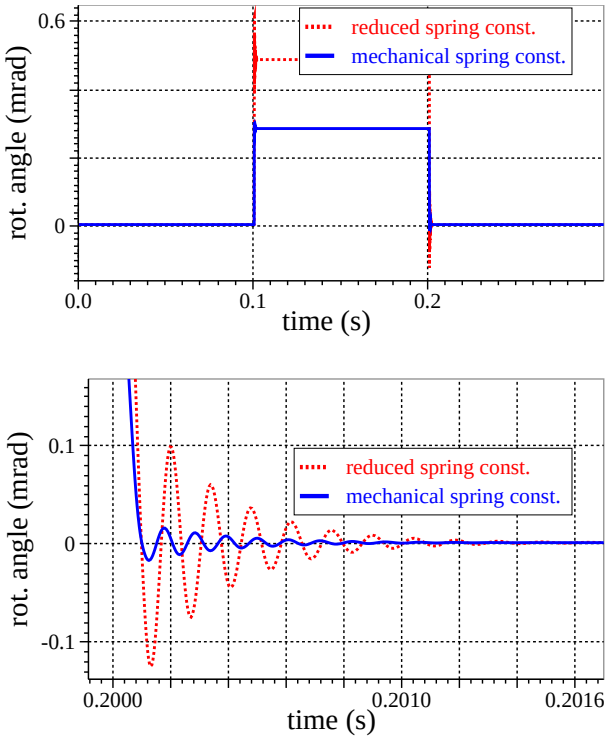

Fig. 5.40: Simulated step response of the rotor in sense direction. Shown is the purely mechanical spring and the electrostatically tuned spring. A detailed view is given in the lower part.

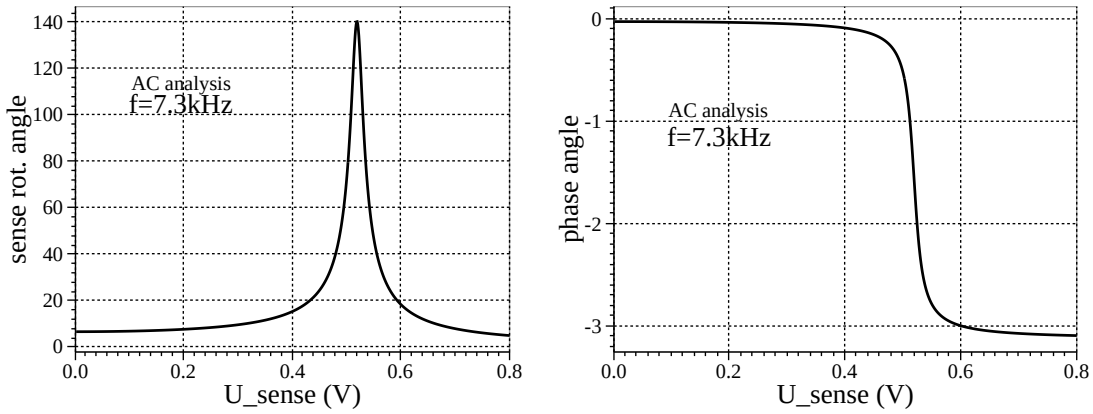

Fig. 5.41: AC small signal analysis of the sense motion of the gyroscope for a given frequency. The voltage on top and bottom electrodes is varied from 0 to 0.8V, thus modifying the resonance frequency of the sense motion.

tolerances this has to be done adaptively by the control electronics, exploiting the aforementioned effect of the electrostatic spring softening. Fig. 5.43 illustrates the increase in amplitude of the sense motion if resonance effects are used.

An important question during a system design is about the manufacturability. One issue here is how the system performance depends on technological tolerances. Because in the described compact models relevant technological and geometrical data is explicitly used as input, this question can be answered directly, without rebuilding the compact

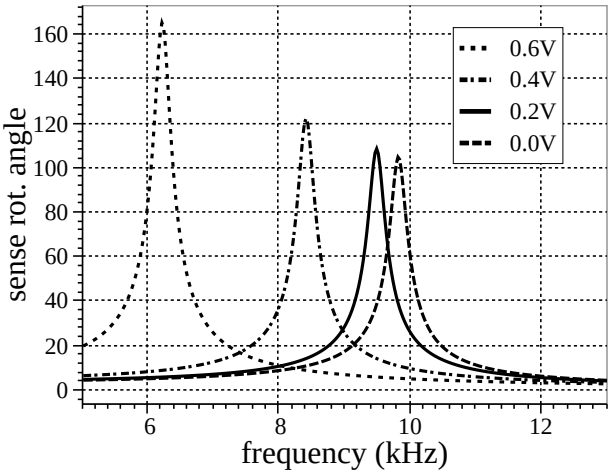

Fig. 5.42: AC small signal analysis of the sense motion of the gyroscope for four different voltages applied to top and bottom electrodes. The frequency is swept from 5 to 15kHz. A quadratic dependency of the resonance frequency on the applied voltage can be seen.

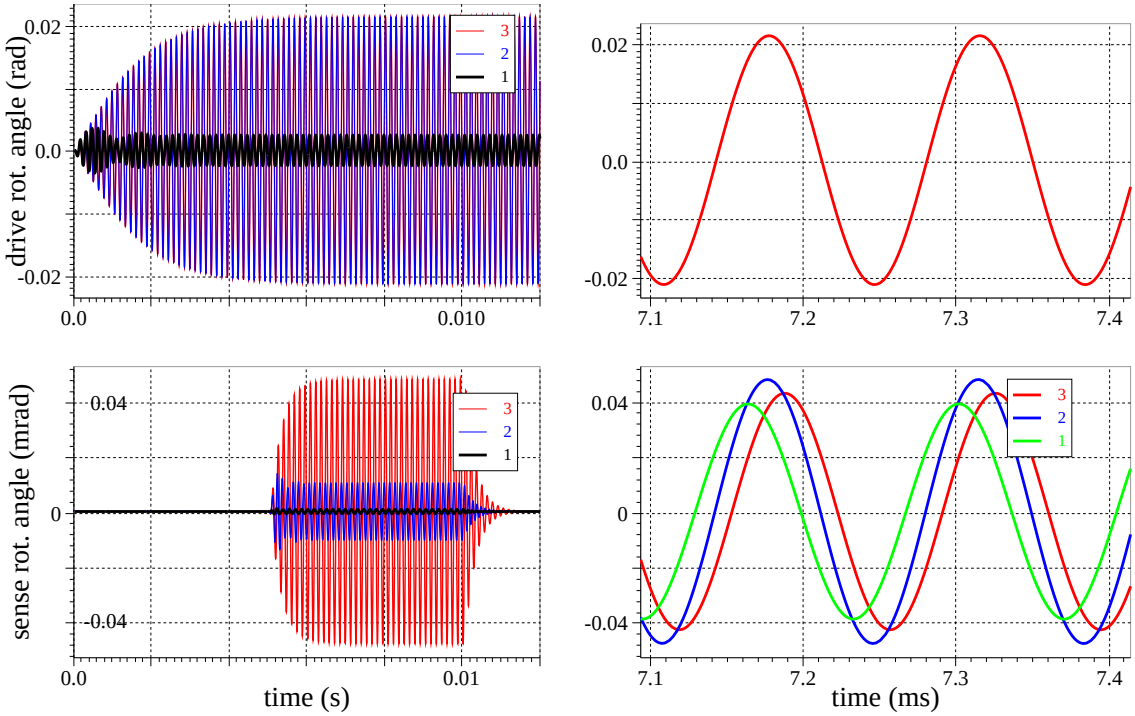

Fig. 5.43: Simulated response of the gyroscope to an input signal (rotation). Left hand side: no resonance effect used (1), only drive resonance (2), drive and sense resonance effect used (3). Right hand side: phase shift between drive and sense oscillation. The sense oscillation frequency is just below or above ((1) and (3)) and exactly at the drive frequency (2).

models from newly measured or FEM-simulated data. Figures 5.44 and 5.45 show the dependence of drive and sense resonance frequencies on a variation of the thickness of the polysilicon and on a variation of the line width of polysilicon (poly CD). The results of

FEM-based simulations are given for comparison, demonstrating the good extrapolation capabilities of the compact models.

The understanding of the simulated results can be supported by the following qualitative considerations:

In drive mode, the stiffness of the springs (spring constant k) can be approximated using a formula for beam bending

$$k \sim w_{poly}^3 \cdot t_{poly} \,.$$

The resonance frequency can be estimated to be

$$\omega_{drive} \sim \sqrt{\frac{k}{m}} \,,$$

where the effective mass is $m \sim t_{poly}$. This yields a constant drive resonance frequency ω_{drive} when the polysilicon thickness t_{poly} is varied. When the polysilicon linewidth w_{poly} is varied, the resulting change in the effective mass can be neglected, giving the relation

$$\omega_{drive} \sim t_{poly}^{3/2} \,.$$

The same considerations as for the drive mode hold true for the fourth mode, which is an in-plane translatory oscillation in y-direction (Fig. 5.34).

In sense mode however, the spring stiffness can be approximated by a formula for beam torsion

$$k \sim b^3 \cdot h \,,$$

where b is the shorter and h the longer edge of the beam cross section. For the thin beams on both sides of the spring this yields

$$k \sim w_{poly}^3 \cdot t_{poly} \,,$$

but for the central, wide part of the spring one gets

$$k \sim t_{poly}^3 \cdot w_{poly} \,.$$

Since the stiffness of the central, wide part is much larger than that of the thinner beams, one finally observes an only weak dependency of ω_{sense} on the polysilicon thickness, but an approximate relation

$$\omega_{sense} \sim w_{poly}^{3/2} \,.$$

for it's dependency on the polysilicon width.

The third mode is a rotation around the y-axis (Fig. 5.33). The spring stiffness can be approximated by the formula for beam bending

$$k \sim t_{poly}^3 \cdot w_{poly} \,.$$

This leads to $\omega_{mode3} \sim t_{poly}$. Due to its length the middle, wide part of the spring determines the total spring stiffness. This results in a weak dependency $\omega_{mode3} \sim \sqrt{w_{poly}}$ of the resonance frequency on the polysilicon width.

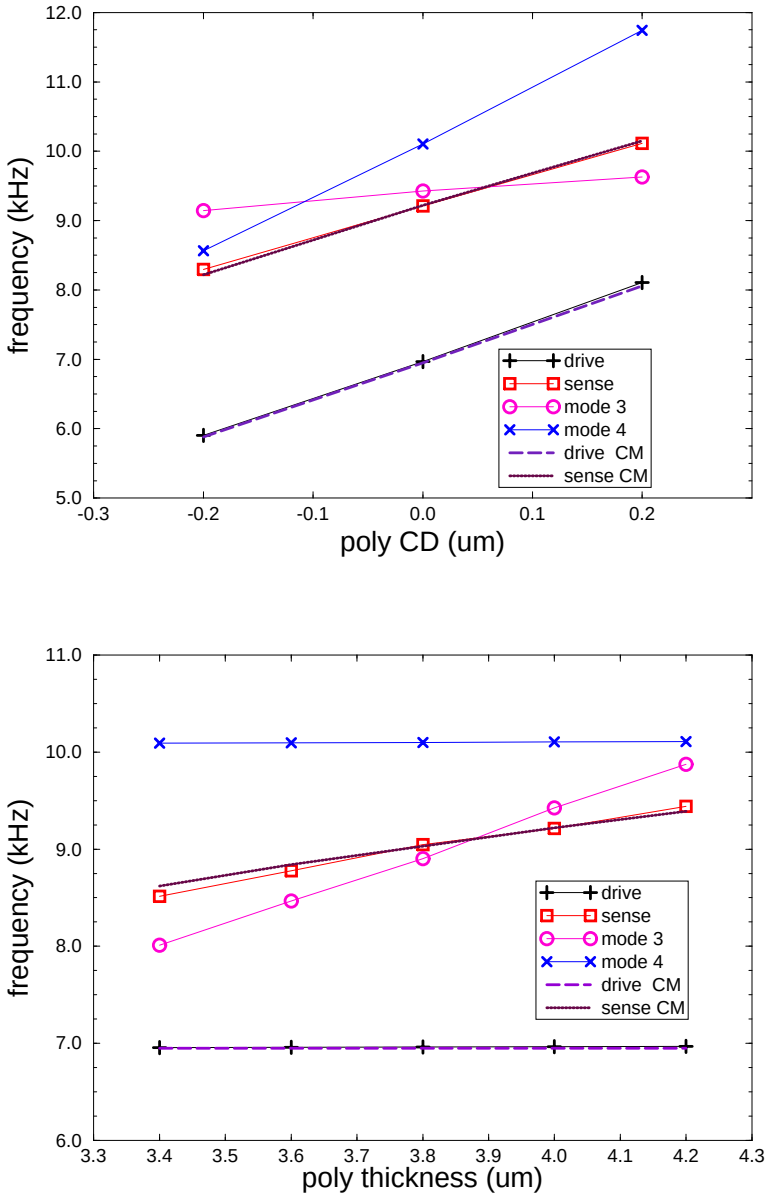

Fig. 5.44: The impact of a variation of the polysilicon linewidth and layer thickness on the gyroscope's oscillatory behavior: The lowest four natural frequencies of the gyroscope as a result of a FEM-based modal analysis, and the two oscillatory modes of the compact model.

Finally, the macro-model of the gyroscope is used to verify the functionality of the electrical control circuitry of the electrostatic comb drive. This circuit was designed at the University of Paderborn [113] and is shown in fig. 5.46. To generate a sufficiently large force in the comb drive, a voltage of 12V is required, which means that a charge pump is needed, because the complete system is supposed to operate with a bias voltage of 5V. The shown circuit uses a square-wave input signal (V11) to generate two alternating square-wave signals (in circuit block *an3lod0*) to drive both stators of the comb drive.

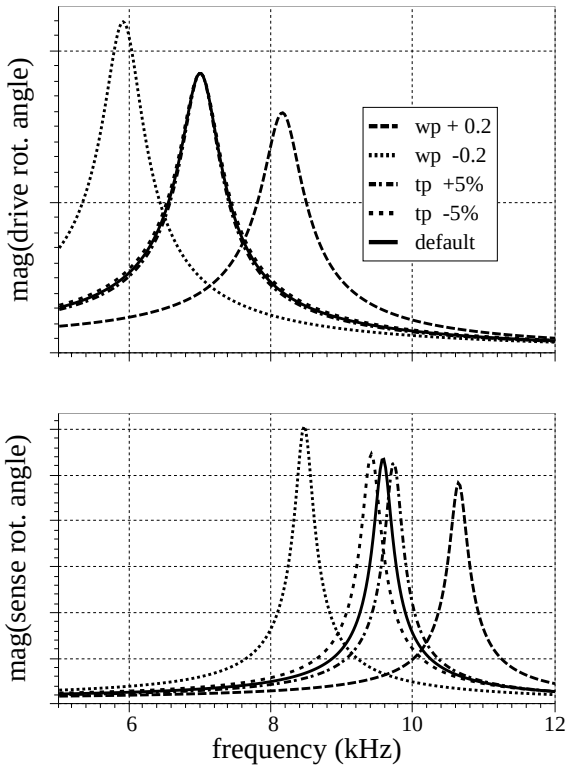

Fig. 5.45: The impact of a variation of the polysilicon linewidth and layer thickness on the gyroscope's frequency response: The AC small signal analysis of the compact model for drive and sense motion. The polysilicon thickness is varied by $\pm 5\%$ and the polysilicon linewidth by $\pm 0.2 \mu m$.

The required signal level of 12V is generated in the driver stage *an3lobi1*.

As mentioned above, the comb drive control circuit generates two alternating square-wave voltages, which are applied to the two stators of the comb drives, thus driving the rotor into oscillation. The voltages at the two stators are shown in Fig. 5.47, as well as the deflection angle in drive direction of the gyroscope rotor. The increasing oscillation amplitude is a typical resonance effect. Additionally, one notices a significant deviation of the voltage waveform from a square shape. The reason is, that the moving comb drive rotor causes a large change in the electrical capacitance of the comb drive, thus causing large displacement currents to flow. This, in turn, lets the drive voltages drop down. Possible causes of an excessive voltage drop can be identified by the simulation: high access resistance, low output conductance of the driver stage, too small capacity of the charge pump. This is a valuable input to a circuit designer, helping him to improve the circuit design.

5.5.5 Conclusions

Starting from a FEM-description of a gyroscope, fully parameterized, physically based analytical compact models of its constituent parts have been developed. Only very few fit-parameters were necessary to achieve very accurate simulation results, compared to FEM data. Due to their close relation to certain physical effects, those fit-parameters

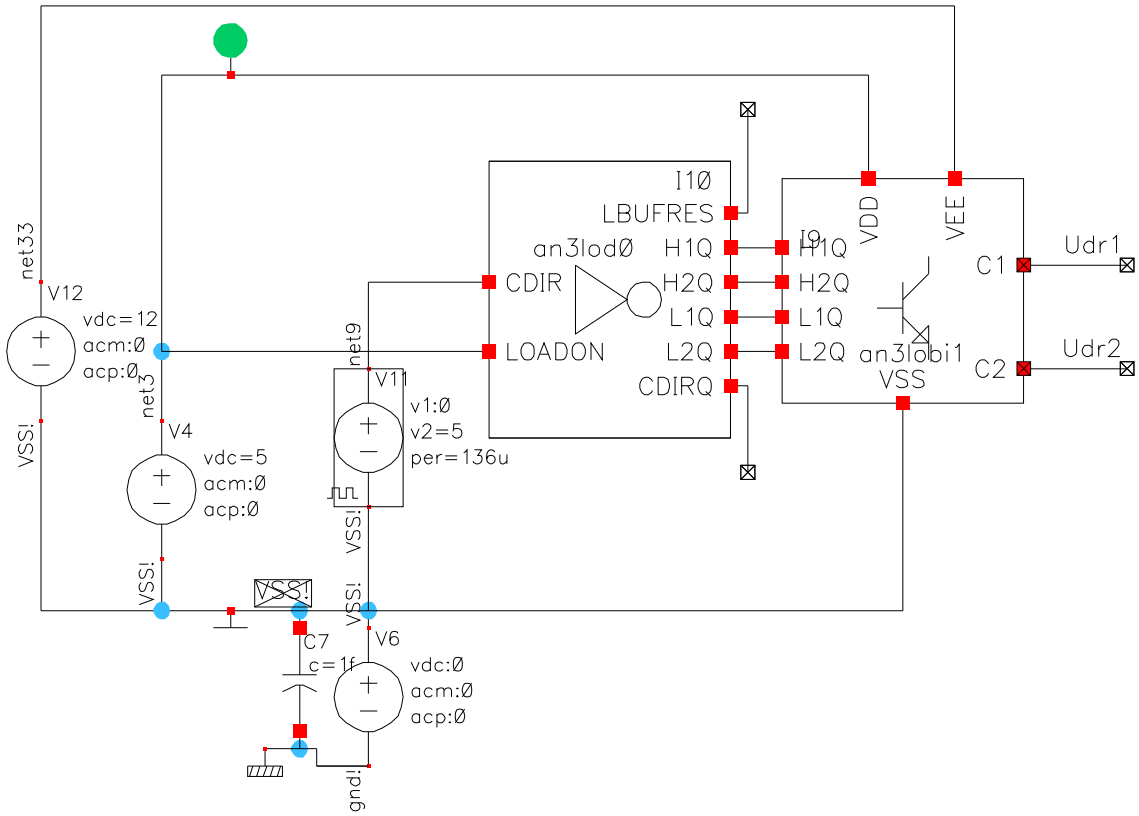

Fig. 5.46: Schematic view of the driver circuit for the electrostatic comb drive of the gyroscope. The compact model of the gyroscope is connected to the nodes Udr1 and Udr2.

could be easily extracted from FEM-simulated device characteristics.

It could be shown, that the developed macro-model is best suited to analyze the impact of process modifications and technological variations on the system behavior.

The mechanical part and electrical parts of the system were simulated and useful feedback to the circuit design could be derived.

Physically based, analytically derived compact models proved to be very useful, powerful and efficient, though elaborative during model development. The building blocks of the gyroscope (comb drives, seismic mass, suspension beams, plate capacitors) are common to various other systems [117, 118, 119, 120]. The developed compact models can therefore easily be adopted to model those sytems.

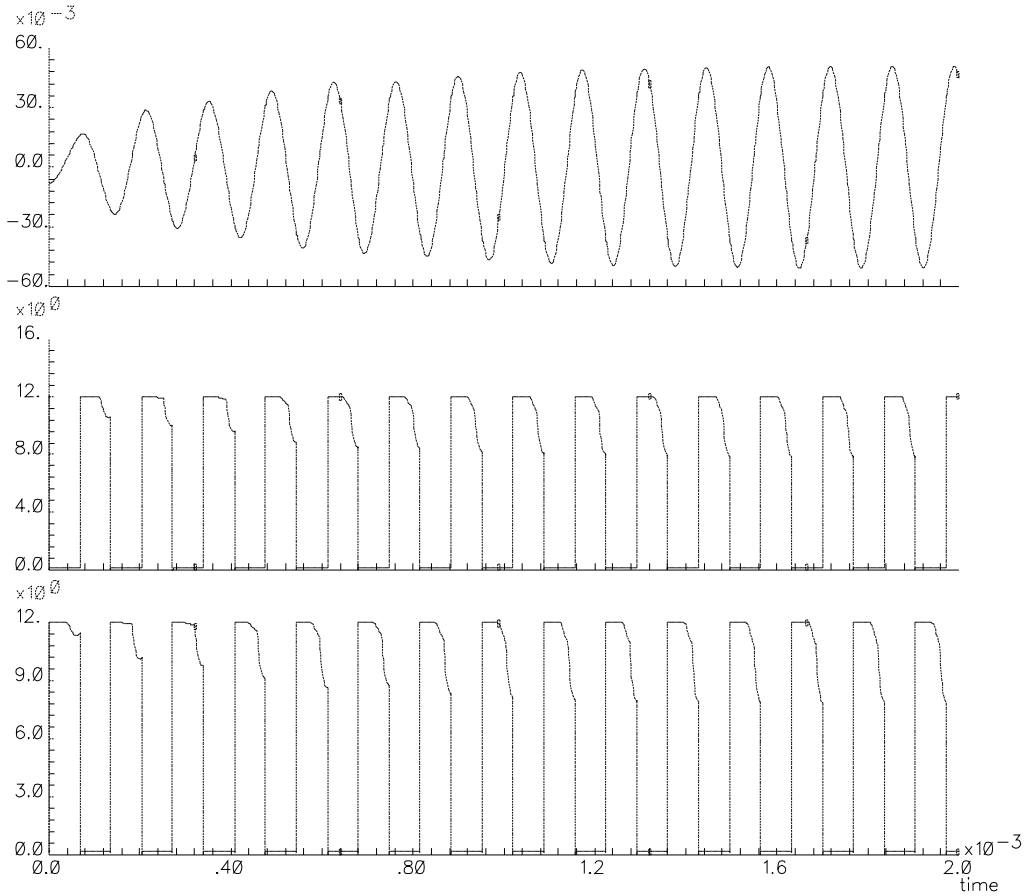

Fig. 5.47: Transient simulation of the driver circuit and the gyroscope. Top: The gyroscope starts oscillating in resonance. Middle/bottom: The drive voltage at the comb drive stators decreases during a drive pulse, because the changing interdigital capacitance of the comb drive causes a current flow, which in return causes a voltage drop due to the output resistance and connecting line resistance of the driver.

6. Summary

Thermodynamics provides a unifying phenomenological description to physical effects and processes in systems and is, therefore, well suited to model microsystems. Some fundamentals of thermodynamics, which appeared to be important in this context, have been recalled. Also the generalization of the well known concept of Kirchhoffian network modeling to non-electrical physical domains was brought to the focus. This provided the basis for the following development of guidelines for the partitioning of complex systems into devices. A list of assumptions which must be fulfilled for a successful system partitioning was established.

These devices are the subject of compact modeling. Starting from a thermodynamic description, a generic structure of a compact model could be found. Two simple examples (electric resistor with self-heating effect and electric capacitor) demonstrated, that the application of this generic model finally leads to well known compact models, but additionally some rules for the determination of the model parameters could be derived.

Next, three different modeling approaches have been compared, namely finite network modeling, basis function modeling and analytical, physically based modeling. Some of their advantages and disadvantages have been identified, leading to the conclusion, that no general preference could be found, but the best choice depends on the requests which must be fulfilled. This list of request should not be limited to technical problems, but commercial aspects (engineering time) have to be considered as well. The most powerful, but also the most elaborative approach during model setup has been found to be the analytical modeling. The most important aspects are the ability to support design studies, process control tasks and statistical modeling. Examples for each approach have been given for illustration. For the finite network modeling, a software tool for the transformation of a CAD model into a finite network model had to be developed, whereas for the basis function modeling an interface to a commercial PCA-tool had to be created.

Parameter extraction has been identified as an essential part of compact model development, especially for analytical, physically based models. It could be shown, that well established methods of electronic device modeling like direct extraction and local optimization can be successfully applied to microsystem devices, despite such particularities of microsystem devices as discontinuities and hysteresis effects, e.g.. An software interface made a commercial parameter extraction tool for electronic devices available for the parameterization of compact models of microsystem devices.

A suite of examples finally illustrated the aforementioned methods of compact modeling of mircosystems. It could be demonstrated that important questions during system design, product development and production of microsystem development can be addressed by means of analytical, physically based compact modeling.

Although (or maybe even - because) there remain many open questions, it is worthwhile

to spend more effort in this field in order to fully integrate microsystem device modeling in the design flow of electronic systems. A little step towards this aim has been done in this work. A long way has to be gone yet.

Appendix

A. Compact model code of the flap valve

A.1 VHDL-AMS model code

```
-- valve Model incl. inertia (for reverse pumping effects)
library ieee;
use ieee.math_real.all;
library TEMP;
use TEMP.pvo.all;

ENTITY valve IS
GENERIC(a1      : REAL :=   1.7e-3;   -- flap length
a2      : REAL :=   1.0e-3;   -- flap width
  dm      : REAL :=  15.0e-6;   -- flap thickness
  a4      : REAL :=   0.4e-3;   -- valve diameter
  a5      : REAL :=   5.0e-6;   -- valve seat length
    rhoSi    : REAL := 2400.0;
    emodul   : REAL :=   1.6e11;
    krl      : REAL :=  10.0;
    krs      : REAL :=   5.0e6;
    fit_stif : REAL :=   0.13;
    fit_pdr  : REAL :=   2.0;
    fit_adh  : REAL :=  13.0;
    pf       : REAL := 15000.1;
    ws       : REAL :=   0.9e5
);
PORT(TERMINAL p_in, p_out : fluidic);
END valve;

ARCHITECTURE basic OF valve IS
   CONSTANT mm      : REAL := fit_adh *  a1*a2*dm*rhoSi;
                                        -- mass of flap + adhes. fluid
   CONSTANT federk : REAL := emodul * dm*dm*dm * a2 * fit_stif;
   CONSTANT fk_rev : REAL := emodul * dm*dm*dm * 66.0 * fit_stif / (a4*a4);
   CONSTANT l_vent : REAL := a1 - 0.5*(a2-a4-a5) - 0.5*a4;

   QUANTITY pp, vv, yy, Ao, lsp, ys : REAL;   -- yy in m, vv in 1e-4*m/s
   QUANTITY p  ACROSS w  THROUGH  p_in TO p_out;
```

```
BEGIN
pp == 1.0e+5 * p;          -- pp in N/m^2

vv == 1.0e-4*yy'dot;       -- factor 1e-4 due to abstol-scaling

IF (yy > 0.0) USE

        Ao  == a4*(a4 - fit_pdr*yy);
         lsp == sqrt(a5*a5 + fit_pdr*yy*fit_pdr*yy);
         ys  == abs(yy + 2.1e-6);

   pp*Ao == federk * yy
            / ((l_vent-yy*fit_pdr)*(l_vent-yy*fit_pdr)*(l_vent-yy*fit_pdr))

          + mm * 1.0e4*vv'dot    -- inertia

          + krl * vv             -- friction prop. to velocity
          + krs * vv*abs(vv);    -- friction prop. to velocity^2

   w == sqrt(abs(pp)) * ys * a4/(lsp+1.0e-12) * ws * pp/(abs(pp)+pf)
              * ys/(ys+4.0e-5)
         + 1.0e6*60.0*0.3*Ao*1.0e4*vv  -- bending of flap causes flow
         + 1.0e6*60.0*0.6*Ao*1.0e4*vv; -- moving flap causes flow
```

```
ELSE
            Ao  == a4*a4;
    lsp == a5;
    ys  == 2.1e-6;

    pp*Ao == federk * yy
               / ((l_vent-yy*fit_pdr)*(l_vent-yy*fit_pdr)*(l_vent-yy*fit_pdr))

           + mm * 1.0e4*vv'dot   -- inertia

           + krl * vv            -- friction prop. to velocity
           + krs * vv*abs(vv)   -- friction prop. to velocity^2

           + 0.01*fk_rev * yy      -- increased force in reverse dir.
           + 10.0 * krl * vv  -- friction proportional to velocity
           + 50.0 * krs * vv*abs(vv); -- friction prop. to velocity^2

    w == sqrt(abs(pp)) * ys * a4/(a5+1.0e-12) * ws * pp/(abs(pp)+pf)
                 * ys/(ys+4.0e-5)
         + 1.0e6*60.0*0.3*Ao*1.0e4*vv; -- bending of flap causes flow
END USE;

END basic;
```

A.2 SpectreHDL model code

```
// valve Model incl. inertia (for reverse pumping effects)

module valve (p_in, p_out) (a1, a2, dm, a4, a5)
node[P,W] p_in, p_out;          // unit: bar,  ml/min
parameter real a1 = 1.7e-3;   // flap length, unit: m
parameter real a2 = 1.0e-3;   // flap width
parameter real dm = 15.0e-6; // flap thickness
parameter real a4 = 0.4e-3;   // valve diameter
parameter real a5 = 5.0e-6;   // valve seat length
{
    real pp, ppa, mm, springk, fk_rev, Ao, l_vent, leff, lgap, ys;

//  Model parameters, to be set in a model file (or during instantiation)
    parameter real rhoSi  = 2400;          // density of silicon, unit: kg/m^3
    parameter real emodul = 1.6e11;        // E-module of silicon, unit: Pa
    parameter real viscos = 1.0e-3;        // viscosity of water, unit: Pa*s
    parameter real krl = 10.0;             // linear damping coeff. (fit)
    parameter real krs = 5e6;              // quadratic damping coeff. (fit)
    parameter real fit_stif = 0.13;        // fits flap stiffness, includes
                                           //  moment of inertia for beam
    parameter real fit_pdr   = 2.0;        // fits the range wherein most of the
                                           //  pressure drop occurs (around the valve seat)
    parameter real fit_adh   = 13;         // fits the amount of liquid that is moved
                                           //  together with the flap to obtain the correct
                                           //  resonance frequency
    parameter real pf = 15000.1;           // change from quadratic to lin. flow rate
    parameter real ws = 0.9e2;             // fits the flow rate

    node[Pos,F] yy, vv;                    // flap displacement and velocity
                                           // units: yy in m, vv in 1e-4*m/s
```

```
    initial {
mm      = fit_adh * a1*a2*dm*rhoSi;   // mass of flap and adhes. fluid
        springk = emodul * dm*dm*dm * a2 * fit_stif; // mech. spring const. according to beam formula
        fk_rev  = emodul * dm*dm*dm * 66.0 * fit_stif / (a4*a4); // increased stiffness in rev. dir.
        l_vent  = a1 - 0.5*(a2-a4-a5) - 0.5*a4;
    }
    analog {
pp  = P(p_in,p_out)*1.0e+5;           // unit: N/m^2
ppa = abs(pp);

Pos(vv) <- 1.0e-4*dot(Pos(yy));    // factor 1e-4 due to abstol-scaling

if (Pos(yy) > 0.0) { // forward direction
            Ao  = a4*(a4 - fit_pdr*Pos(yy));  // effective area that pressure acts on
            ys  = abs(Pos(yy)) + 1e-6;        // opening of the flap, i.e. the height of the rectang.
                                              // channel, which width is the valve seat perimeter
} else {             // reverse direction
            Ao  = a4*a4;
    ys  = 1e-6;

    F(yy) <- fk_rev * Pos(yy);      // increased force in reverse dir.
    F(yy) <- 10.0 * krl * Pos(vv);  // friction proportional to velocity
    F(yy) <- 50.0 * krs * Pos(vv)*abs(Pos(vv)); // friction prop. to velocity^2
}
```

```
    lgap = a5 + fit_pdr*ys;              // length of the flow "channel"

  W(p_in,p_out) <- ppa/(ppa+pf) * ys * a4/lgap * ws/viscos * pp/(ppa+pf)
                   * ys/(ys+4.0e-5); // some "inspiration" taken from formula for flow
                                     // through rectangular channel
      leff = l_vent - ys*fit_pdr;    // effective flap "beam" length

  F(yy) <- springk * Pos(yy) / (leff*leff*leff); // mechanical force due to flap bending

  F(yy) <- -pp*Ao;                   // force due to hydrostat. pressure drop across the valve

  F(yy) <- mm * 1.0e4*dot(Pos(vv));  // inertia

  F(yy) <- krl * Pos(vv);            // friction prop. to velocity
  F(yy) <- krs * Pos(vv)*abs(Pos(vv)); // friction prop. to velocity^2

  W(p_in,p_out) <- 1.0e6*60.0*0.6*Ao*1.0e4*Pos(vv);  // moving flap causes flow
    }
}
```

B. Compact model code of the membrane

```
// Membrane Model
// P.Voigt
// accounts for: - deflection due to pressure
//               - deflection due to applied voltage
//               - nonlinear deflection (large displacement effect)
//               - shape snapping during touch down (crude fitting only!)

module membran (v_in, v_gnd, p_in, p_gnd) (d0, dox, dmembran, lmembran)
node[V,I] v_in, v_gnd;
node[P,W] p_in, p_gnd;          // unit: bar,  ml/min
parameter real d0       = 5.0e-6;  // membrane thickness, unit: m
parameter real dox      = 2.0e-6;  // isolation oxide thickness
parameter real dmembran = 40.0e-6; // membrane thickness
parameter real lmembran = 5.0e-3;  // quadratic membrane edge length
{
    real eps0 = 8.85419e-12;
    real  ddx, dd0, i_mbr, lmbr, emdl, p, peff, pwr, u, c, ffe, ff2, pp;
    node [Y,U] y_max, ll;    // membrane center deflection, effective edge length
                             // unit: micrometer
    node [M,U] vol;          // displaced volume, unit: nl
//  Model parameters, to be set in a model file (or during instantiation)
    parameter real emodul   = 1.4e+11;
    parameter real epsox    = 3.9;
    parameter real fit_stif = 100.0;   // fits membr. stiffness (small defl.)
    parameter real fit_pnl  = 0.32;    // nonlinearity at large deflections
    parameter real f2       = 0.33333; // fits volume (corners)
    parameter real f3       = 1.0;     // fits volume (edges, when touched down)
    parameter real fit_fef  = 0.29;    // fits snap voltage forward
    parameter real fit_fer  = 0.8;     // fits snap voltage reverse
    parameter real fit_uu   = 4.4e-5;  // fits shape snap point and volume
```

```
    initial {
dd0    = 1.0e6*d0;
ddx    = dd0 + 1.0e6*dox/epsox;
i_mbr = dmembran*dmembran*dmembran*fit_stif;
lmbr   = 1000.0*lmembran;
emdl   = 1.0e-5*emodul;

pwr    = lmembran*lmembran*lmembran*lmembran/(1.0e-6*emdl*i_mbr);
         ffe    = fit_fef;
         peff   = 0.0;
       }
       analog {
u = V(v_in, v_gnd);
p = P(p_in, p_gnd);

if (Y(y_max) > 0.0) {
            ffe = fit_fer * (1.0 - 0.7*pow(Y(ll)/lmbr,2) * pow(Y(y_max)/dd0,8) )
                + fit_fef; // fits the electrostatic force (for shape snap)
            ff2 = f2 - fit_uu*u*u * (Y(y_max)/dd0) * pow(Y(ll)/lmbr,4);
            // fits the displaced volume (to model shape snap)
            pp  = p;
} else {    ffe = fit_fef + fit_fer;
            ff2 = f2;
   pp = fit_pnl*asinh(p/fit_pnl); // nonlinearity for large defl.
}
```

```
        peff = ffe * 1.0e-5*eps0*u*u*0.5/(ddx*ddx*1.0e-12) * ddx/(ddx-Y(y_max));
// pressure due to electrostatic force

        Y(y_max) <- min((pp+peff)*pwr,dd0);

c =   eps0           *Y(ll)*Y(ll)       /sqrt(ddx*abs(ddx-Y(y_max)))
    + eps0*2.0*(lmbr-Y(ll))*Y(ll)       /sqrt(ddx*abs(ddx-Y(y_max)))
    + eps0    *(lmbr-Y(ll))*(lmbr-Y(ll))/         abs(ddx-Y(y_max));
    // corners + edges + touch down area

if (Y(y_max) > 0.0) {
            Y(ll) <-
 min(1000.0*pow((emdl*i_mbr*d0/abs(1e-3+fit_pnl*asinh((pp+peff)/fit_pnl))),0.25),lmbr);
   // membrane touched down, so effective edge length reduces
} else {
            Y(ll) <- lmbr;
}

M(vol) <- Y(y_max)*
( (lmbr-Y(ll))*(lmbr-Y(ll)) + f3*Y(ll)*(lmbr-Y(ll)) + ff2*Y(ll)*Y(ll) );
// touch down area          + edge areas            + corner areas

W(p_in, p_gnd) <- 1.0e-6*60.0*dot(M(vol));  // unit: ml/min

I(v_in, v_gnd) <- dot(c*u);
    }
}
```

C. Compact model code of the combdrive

```
-- comb drive
--  Purpose: an applied el. voltage creates an attracting force (torque)
--           in the drive direction and in the sense direction
NATURE electrical IS
    ACROSS V;
    THROUGH I;
END electrical;
NATURE rotational IS
ACROSS Phi;
THROUGH M;
END rotational;
ENTITY combdrive is
GENERIC(d_poly   : REAL :=   4.0e-6;
d_gap1    : REAL :=   1.5e-6;
d_gap2    : REAL :=   0.5e-6;
d_angl    : REAL :=   1.5e-6;
r_drive   : REAL := 300.0e-6;
n_finger  : REAL :=   5.0;
l_finger  : REAL :=  8.0e-6;
fit_torq  : REAL :=  1.0;     -- fits the torque magnitude
fit_step  : REAL :=  1.8;     -- fits how abrupt the force changes
   -- large value means abrupt change
fit_angl  : REAL := -0.1e-6  -- offset to the transition angle
);
PORT(v_st1, v_st2, vcomb : electrical; p_drive : rotational);
END combdrive;
ARCHITECTURE basic_combdrive OF combdrive IS
    CONSTANT eps0 : REAL := 8.85419e-12;
    CONSTANT c_gap1  : REAL := 2.0*n_finger * eps0 * d_poly / d_gap1;
    CONSTANT c_gap2  : REAL := 2.0*n_finger * eps0 * d_poly / d_gap2;
    CONSTANT c0      : REAL := c_gap1 * 0.1*l_finger;
    CONSTANT phi_crt : REAL := (fit_angl + d_angl) / r_drive;
    VARIABLE u1, u2, Pdrv, c1, c2, h1, h2 : REAL := 0.0;
```

```
BEGIN
RELATION BEGIN
u1   := [v_st1, vcomb].V;
u2   := [v_st2, vcomb].V;
Pdrv := p_drive.Phi;

        h1 := 0.5 * (1.0 + tanh(fit_step*(-Pdrv/phi_crt - 1.0)) );
        h2 := 0.5 * (1.0 + tanh(fit_step*( Pdrv/phi_crt - 1.0)) );

c1 := c0 + c_gap1
* 0.5*((l_finger - Pdrv*r_drive)+abs(l_finger - Pdrv*r_drive))
      + c_gap2
* 0.5*r_drive*((-Pdrv - 0.5*phi_crt)+abs(-Pdrv - 0.5*phi_crt)) * h1;

c2 := c0 + c_gap1
* 0.5*((l_finger + Pdrv*r_drive)+abs(l_finger + Pdrv*r_drive))
      + c_gap2
* 0.5*r_drive*(( Pdrv - 0.5*phi_crt)+abs( Pdrv - 0.5*phi_crt)) * h2;

        p_drive.M <= 2.0 * fit_torq * n_finger * (eps0 / 2.0)
* r_drive * (u2*u2 - u1*u1) * d_poly / d_gap1
             - h1 * 2.0 * fit_torq * n_finger * (eps0 / 2.0)
* r_drive *          u1*u1  * d_poly / d_gap2
             + h2 * 2.0 * fit_torq * n_finger * (eps0 / 2.0)
* r_drive *  u2*u2           * d_poly / d_gap2;

[v_st1, vcomb].I <= ddt(u1 * c1);
[v_st2, vcomb].I <= ddt(u2 * c2);
END RELATION;
END basic_combdrive;
```

D. List of symbols

For better orientation, the list of symbols is grouped by chapters. Symbols are listed corresponding to the chapter wherein they appear first.

Chapter 2.2

symbol	description
$\vec{a}$	area
α_{ij}	elements of state matrix
$\vec{B}$	magnetic field
C'	specific heat capacity
E_i	extensive state variable (per control volume dV)
$\vec{f}_i$	affinity
I_i	intensive state variable
$\vec{J}_i$	flux quantity
L_{ij}	Onsager phenomenological coefficients
p	pressure
Q	heat energy
$\vec{r}$	space vector
S	entropy per control volume dV
σ	entropy production rate
T	temperature
t	time
τ	relaxation time constant
U	internal energy per control volume dV
V	volume

Chapter 2.3

symbol	description
A	interface area
$\mathbf{C}$	generalized capacity matrix
$\mathcal{E}_i$	averaged interface affinity
Φ_i	averaged interface potential
Γ	interface between adjacent sub-systems
K_i^M	coupling coefficient
Π_i	production rate of quantity $\mathcal{E}_i$
π_i	production rate density of quantity $\mathcal{E}_i$
Q_i	extensive quantity $\mathcal{E}_i$ contained in system volume V
R_{ij}	coefficients of inverse Onsager matrix
$\mathcal{W}_i$	averaged interface flow rate

Chapter 2.3.4

symbol	description
A	area
C	electric capacity
C_{th}	heat capacity
$\vec{E}$	electric field
I	electric current
$\vec{j}$	electric current density
L_{el}	electric conductivity
l	length
λ	thermal conductivity
P	power
Q_{th}	heat energy
Q	electric charge
σ	specific electric conductivity
U	voltage

Chapter 5.3

symbol	description
C	electric capacity
$\mathcal{C}$	electric capacity per unit length
j	electric current
k	tube elasticity
L	electric inductivity
$\mathcal{L}$	electric inductivity per unit length
λ	wavelength
ν	cinematic viscosity
p	pressure
R	electric resistance
$\mathcal{R}$	electric resistance per unit length
R_0	inner tube radius
r, x, ϕ	cylinder coordinates
ρ	fluid density
S_0	fluidic cross section
ξ	change of tube radius
u	voltage
V	volume
$\vec{v}$	velocity
w	flow rate
ω	circular frequency

Bibliography

[1] K. Böhringer, B. Donald, N. MacDonald, G. T. A. Kovacs, and J. W. Suh, "Computational methods for design and control of MEMS micromanipulator arrays," *IEEE CSE*, pp. 17–29, 1997.

[2] S. Senturia, N. Aluru, and J. White, "Simulating the behavior of MEMS devices: Computational methods and needs," *IEEE CSE*, pp. 30–43, 1997.

[3] S. Senturia, "CAD Challenges for Microsensors, Microactuators and Microsystems," *Proc. of the IEEE*, vol. 86, pp. 1611–1626, 1998.

[4] J. Ulrich and R. Zengerle, "Static and dynamic flow simulation of a KOH-etched microvalve using the finite-element method," *Sensors and Actuators*, vol. A53, pp. 379–385, 1996.

[5] G. Wachutka, "Tailored modeling: a way to the 'virtual microtransducer fab'?," *Sensors and Actuators*, vol. A46–47, pp. 603–612, 1995.

[6] IEEE, New York, *Standard VHDL Analog and Mixed-Signal Extensions*, 1999.

[7] J. Parrott, "Thermodynamic theory of transport processes in semiconductors," *IEEE Trans. Electron Devices*, vol. 43, pp. 809–826, 1996.

[8] G. Wachutka, "Tailored modeling of miniaturized electrothermomechanical systems using thermodynamic methods," in *Micromechanical Systems, DSC-Vol. 40* (D. Cho, J. Peterson, A. Pisano, and C. Friedrich, eds.), pp. 183–198, The American Society of Mechanical Engineers, New York, 1992.

[9] G. Wachutka, "Problem-oriented modeling of microtransducers: State of the art and future challenges," *Sensors and Actuators*, vol. A41, pp. 279–283, 1994.

[10] D. van Duyn and S. Middelhoek, "Information transduction in solid-state transducers: A general thermodynamic systems approach," *Sensors and Actuators*, vol. A21-A23, pp. 25–32, 1990.

[11] K. Aflatooni, R. Hornsey, and A. Nathan, "Thermodynamic treatment of mechanical stress gradients in coupled electro-thermo-mechanical systems," *Sensors and Materials*, vol. 9, pp. 449–456, 1997.

[12] H. Callen, *Thermodynamics and an Introduction to Thermostatistics*. New York: John Wiley & Sons, 1985.

[13] S. de Groot and P. Mazur, *Non-Equilibrium Thermodynamics*. Amsterdam: North-Holland, 1969.

[14] R. Boite and J. Neirynck, *Theorie des Reseaux de Kirchhoff*. CH-1813 St-Saphorin: Editions Georgi, 1976.

[15] J. Conelly and P. Choi, *Macromodeling with Spice*. Englewood Cliffs, NY: Prentice-Hall, 1992.

[16] M. Zaman, S. Bart, V. Rabinovich, C. Ghaddar, I. Tchertkov, and J. Gilbert, "A Technique for Extraction of Macro-Models in System Level Simulation of Inertial Electro-Mechanical Micro-Systems," in *Proc. of MSM'99*, (San Juan, Puerto Rico), pp. 163–167, Apr. 19–21 , 1999.

[17] H. Pham and A. Nathan, "Circuit modeling and SPICE simulation of mixed-signal microsystems," *Sensors and Materials*, vol. 10, pp. 435–460, 1998.

[18] G. Fedder and R. Howe, "Multimode digital control of a suspended polysilicon microstructure," *J. of Microelectromechanical Systems*, vol. 5, pp. 283–297, 1996.

[19] E. Cretu, M. Bartek, and R. Wolffenbuttel, "Spectral analysis through electromechanical coupling," *Sensors and Actuators*, vol. 85, pp. 23–32, 2000.

[20] J.-S. Shie, Y.-M. Chen, M. Ou-Yang, and B. Chou, "Characterization and modeling of metal–film microbolometer," *J. of Microelectromechanical Systems*, vol. 5, pp. 298–305, 1996.

[21] M. Latif and P. Bryant, "Multiple equilibrium points and their significance in the secondary breakdown of bipolar transistors," *IEEE J. Solid-State Circuits*, vol. SC-16, pp. 8–15, 1981.

[22] IEEE, New York, *IEEE Standard VHDL Language Reference Manual*, 1993.

[23] M. Carmona, S. Marco, J. Sieriro, O. Ruiz, J. Gómez-Cama, and J. Samitier, "Modelling of microsystems with ananlog hardware description languages," *Sensors and Actuators*, vol. 76, pp. 32–42, 1999.

[24] Cadence, San Jose, CA, *SpectreHDL Reference Manual*, 1995.

[25] Analogy Inc., Beaverton, OR, *MAST Reference Manual*, 1995.

[26] Anacad, Ulm, *HDL-A User's Manual*, 1995.

[27] ITWM, Kaiserslautern, Germany, *Analog Insydes Tutorial*, 1998.

[28] D. Rhodes, "A design language for analog circuits," *IEEE Spectrum*, vol. Oct., pp. 43–48, 1996.

[29] E. Boskin, C. Spanos, and G. Korsh, "A method for modeling the manufacturability of ic designs," in *Proc. IEEE Intl. Conf. Microelectr. Test Structures*, (Barcelona, Spain), pp. 241–246, Mar. 1993.

[30] J. Power et al., "An approach for relating model parameter variabilities to process fluctuations," in *Proc. of ICTMS*, p. 63, 1993.

[31] J. Power, B. Donnellan, A. Mathewson, and W. Lane, "Relating statistical MOSFET model parameter variabilities to IC manufacturing process fluctuations enabling realistic worst case design," *IEEE Trans. Semicond. Manufact.*, vol. 7, pp. 306–318, 1994.

[32] C. Spanos and S. Director, "Parameter extraction for statistical IC process characterization," *IEEE Trans. Computer-Aided Design*, vol. 5, pp. 66–78, 1986.

[33] T. Koskinen and P. Cheung, "Statistical and behavioral modeling of analogue integrated circuits," *Proc. Inst. Electr. Eng.*, vol. 140, pt. G, pp. 171–176, 1993.

[34] A. Schroth, T. Blochwitz, and G. Gerlach, "Simulation of a complex sensor system using coupled simulation programs," in *Dig. of Tech. Papers of Transducers'95*, (Stockholm), pp. 33–35, 1995.

[35] R.-C. Eccardt and M. Knoth, "Berecnung von geregelten Sensoren durch Kopplung von ANSYS mit einem Schaltkreis-Simulator," in *CAD-FEM User's Meeting*, (Bad Aibling), 09.-11.Oct.1996.

[36] G. Schrag, P. Voigt, E.-R. Sieber, U. Wiest, R. Hoppe, and G. Wachutka, "Device- and system-level models for micropump simulation," in *Micro Mat'97* (B. Michel and T. Winkler, eds.), (Berlin), pp. 941–944, April 16–18, 1997.

[37] K. Park, "Partitioned transient analysis procedures for coupled-field problems: stability analysis," *Transactions of the ASME*, vol. 47, pp. 370–376, 1980.

[38] E. Ngoya, J. Rousset, and J. Obregon, "Newton-Raphson iteration speed-up algorithm for the solution of nonlinear circuit equations in general-purpose CAD programs," *IEEE Trans. Computer-Aided Design*, vol. 16, pp. 638–644, 1997.

[39] M. Jakovljevic, P. Fotiu, Z. Mrcarica, and H. Detter, "A system-level simulation of complex multi-domain microsystems by using ananlogue hardware description languages," *Sensors and Actuators*, vol. 82, pp. 30–39, 2000.

[40] S. Wünsche, P. Schwarz, U. Becker, and R. Neul, "Ein Modellierungsansatz zur Einbeziehung mechanischer Mikrosystemkomponenten in die Systemsimulation," in *I. MIMOSYS–Statusseminar*, (Paderborn), pp. 23–29, 05.-06.Dec.1996.

[41] R. MacNeal, "The solution of elastic plate problems by electrical analogies," *J. Appl. Mechanics*, pp. 59–67, 1951.

[42] A. Klein, *Modellierung und Simulation von Mikromembranpumpen*. PhD thesis, TU Dresden, Inst. für Festkörperelektronik, Dresden, 1999.

[43] A. Klein, A. Schroth, G. Gerlach, and S. Kurth, "Anwendung der Methode der Finiten Netzwerke zur Modellierung mechanischer Biegeplatten in Mikrosystemen," pp. 156–162.

[44] J. Bielefeld, G. Pelz, and G. Zimmer, *Electrical network formulations of mechanical finite-element models*, pp. 239–247. Southampton, UK, Boston, USA: Computational Mechanics Publications, 1997.

[45] T. Veijola, "Finite-difference large-displacement gas-film model," in *Proc. of Transducers'99*, (Sendai, Japan), pp. 1152–1155, 1999.

[46] B. Krabbenborg, A. Bosma, H. de Graaff, and A. Mouthaan, "Layout to circuit extraction for three-dimensional thermal-electrical circuit simulation of device structures," *IEEE Trans. Computer-Aided Design*, vol. 15, pp. 765–774, 1996.

[47] P. Voigt and G. Wachutka, "Simulation des thermischen Selbsttests an Beschleunigungssensoren mittels VHDL-AMS," in *Bericht zum Abschlußseminar des ASIS-2S Verbundprojekts, Fraunhofer-Institut für Festkörpertechnologie*, (München), 23. Okt. 1998.

[48] S. Timoshenko, *Theory of Plates and Shells*. New York: McGraw-Hill, 1959.

[49] T. Veijola, H. Kuisma, J. Ladenperä, and T. Ryhänen, "Equivalent-circuit model of the squeezed gas film in a silicon accelerometer," *Sensors and Actuators*, vol. A48, pp. 239–248, 1995.

[50] H. Reuther, M. Weimann, M. Fischer, W. von Münch, and F. Assmus, "Modeling electrostatically deflectable microstructures and air damping effects," *Sensors and Materials*, vol. 8, pp. 251–269, 1996.

[51] G. Schrag, P. Voigt, and G. Wachutka, "Squeeze film damping in arbitrary shaped microdevices modelled by an accurate mixed level scheme," in *Proc. of MSM'2001*, (Hilton Head Island, SC), p. accepted for presentation, March 19–21, 2001.

[52] L. D. Gabbay, J. E. Mehner, and S. Senturia, "Computer-aided generation of nonlinear reduced-order dynamic macromodels – I: Non-stress-stiffened case," *J. of Microelectromechanical Systems*, vol. 9, pp. 262–269, 2000.

[53] J. E. Mehner, L. D. Gabbay, and S. Senturia, "Computer-aided generation of nonlinear reduced-order dynamic macromodels – II: Stress-stiffened case," *J. of Microelectromechanical Systems*, vol. 9, pp. 262–269, 2000.

[54] N. Aluru and J. White, "A multi-level Newton method for static and fundamental frequency analysis of electromechanical systems," in *Proceedings of SISPAD*, (Cambridge, MA), pp. 125–128, Sept. 1997.

[55] N. Swart, S. Bart, M. Zaman, M. Mariappan, J. Gilbert, and D. Murphy, "AutoMM: Automatic generation of dynamic macromodels for MEMS devices," in *Proc. of MEMS'98*, (Heidelberg), pp. 178–183, 1998.

[56] M. Varghese, V. Rabinovich, and S. Senturia, "Reduced-order modeling of Lorentz force actuation with modal basis functions," in *Proc. of MSM'99*, (San Juan, Puerto Rico), pp. 155–158, Apr. 19–21 , 1999.

[57] E. Hung, Y.-J. Yang, and S. Senturia, "Low-order models for fast dynamical simulation of MEMS microstructures," in *Dig. of Tech. Papers of Transducers'97*, (Chicago), pp. 1101–1104, June 16–19, 1997.

[58] E. Hung and S. Senturia, "Generating efficient dynamical models for microelectromechanical systems from a few Finite-Element simulation runs," *J. of Microelectromechanical Systems*, vol. 8, pp. 280–289, 1999.

[59] Silvaco International, Santa Clara, *Spayn User's Manual*, 1994.

[60] R. Zengerle, J. Ulrich, S. Kluge, M. Richter, and A. Richter, "A bidirectional silicon micropump," *Sensors and Actuators*, vol. A50, pp. 81–86, 1995.

[61] E. Yang, S. Yang, S. Han, and S. Kim, "Fabrication and dynamic testing of electrostatic actuators with p^+ silicon diaphragms," *Sensors and Actuators*, vol. A50, pp. 151–156, 1995.

[62] P. Voigt, G. Schrag, and G. Wachutka, "Microfluidic system modeling using VHDL-AMS and circuit simulation," *Microelectronics J.*, vol. 29, pp. 791–797, 1998.

[63] Silvaco International, Santa Clara, *TCAD Examples Manual*, 1997.

[64] D. Maier-Schneider, J. Maibach, and E. Obermeier, "A new analytical solution for the load-deflection of square membranes," *J. of Microelectromechanical Systems*, vol. 5, pp. 238–241, 1995.

[65] H. Elgamel, "Closed-form expressions for the relationships between stress, diaphragm deflection, and resistance change with pressure in silicon piezoresistive pressure sensors," *Sensors and Actuators*, vol. A50, pp. 17–22, 1995.

[66] D. Peters, S. Bechtold, and R. Laur, "Optimized behavioral model of a pressure sensor including the touch-down effect," in *Proc. of MSM'99*, (San Juan, Puerto Rico), pp. 237–240, Apr. 19–21 , 1999.

[67] P. Karlsson and K. Jeppson, "Direct extraction of MOS transistor model parameters," *Analog Integr. Circuits Signal Process.*, vol. 5, pp. 199–212, 1994.

[68] M. Qu and M. Styblinski, "Parameter extraction for statistical ic modeling based on recursive inverse approximation," *IEEE Trans. Computer-Aided Design*, vol. 16, pp. 1250–1259, 1997.

[69] Silvaco International, Santa Clara, *Utmost User's Manual*, 1996.

[70] A. Gutierrez, S. Aceto, M. Simkulet, D. Patti, M. Liendhard, T. Krawczyk, and A. Lundgren, "MEMS/MST model verification and materials parameter extraction using MEMSPEC-2000," in *Proc. of MSM'99*, (San Juan, Puerto Rico), pp. 1–4, Apr. 19–21 , 1999.

[71] P. Osterberg and S. Senturia, "M-TEST: A test chip for MEMS material property measurement using electrostatically actuated test structures," *J. of Microelectromechanical Systems*, vol. 6, pp. 107–118, 1997.

[72] D. Wang and J. Tarbell, "Nonlinear analysis of flow in an elastic tube (artery): steady streaming effects," *J. Fluid Mech.*, vol. 239, pp. 341–358, 1992.

[73] P. Voigt, G. Schrag, and G. Wachutka, *Design and Numerical Analysis of an Electro-Mechanical Microsystem for Material Parameter Extraction*, pp. 209–218. Southampton, UK, Boston, USA: Computational Mechanics Publications, 1997.

[74] M. Biebl et al., "Micromechanics compatible with an 0.8 μm CMOS process," *Sensors and Actuators*, vol. A46–47, pp. 593–597, 1995.

[75] N. Vandelli, D. Wroblewski, M. Velonis, and T. Bifano, "Development of a MEMS microvalve array for fluid flow control," *J. Microelectromechanical Systems*, vol. 7, pp. 395–403, 1998.

[76] M. Stehr, S. Messner, H. Sandmaier, and R. Zengerle, "The VAMP – a new device for handling liquids or gases," *Sensors and Actuators*, vol. A57, pp. 153–157, 1996.

[77] A. Meckes, J. Behrens, O. Kayser, W. Benecke, T. Becker, and G. Müller, "Microfluidic system for the integration and cyclic operation of gas sensors," *Sensors and Actuators*, vol. 76, pp. 478–483, 1999.

[78] T. Gerlach and H. Wurmus, "Working principle and performance of the dynamic micropump," *Sensors and Actuators*, vol. A50, pp. 135–140, 1995.

[79] M. Heschel, M. Müllenborn, and S. Bouwstra, "Fabrication and characterization of truly 3-D diffuser/nozzle microstructures in silicon," *J. Microelectromechanical Systems*, vol. 6, pp. 41–46, 1997.

[80] R. Zengerle, *Mikro-Membranpumpen als Komponenten für Mikro-Fluidsysteme*. PhD thesis, Univ. der Bundeswehr, Verlag Shaker, Aachen, 1994.

[81] Swanson Analysis Systems, Houston, PA, *ANSYS User's Manual, Rev. 5.0*, 1992.

[82] P. Voigt, G. Schrag, and G. Wachutka, "Electrofluidic full-system modeling of a flap valve micropump based on Kirchhoffian network theory," *Sensors and Actuators*, vol. A66, pp. 9–14, 1998.

[83] G. Wachutka, H. Pavlicek, A. Horn, G. Schrag, P. Voigt, G. Schrag, F. Wittmann, T. Feudel, and N. Strecker, *CAD tools for MEMS*. Neuchatel: FSRM, 1998.

[84] W. Bohl, *Technische Ströhmungslehre*. Würzburg: Vogel-Buchverlag, 1967.

[85] E. Kälvesten, L. Löfdahl, and G. Stemme, "Analytical characterization of piezoresistive square-diaphragm silicon microphone," *Sensors and Materials*, vol. 8, pp. 113–136, 1996.

[86] J. Womersley, "An elastic tube theory of pulse transmission and oscillatory flow in mammalian arteries," Tech. Rep. 56-614, Wright Air Development Centre, 1957.

[87] D. Ludewig, "Beitrag zur mathematischen Modellierung der Druckstosserscheinungen in Rohrleitungen und Rohrsystemen," *WWT*, vol. 20.11, pp. 376–381, 1970.

[88] D. Voigt, "Die Niederschlagsintensität bei der Impulsberegnung," *Grundl. Landtechnik*, vol. 38.3, pp. 97–100, 1988.

[89] J. Womersley, "Oscillatory flow in arteries: the constrained elastic tube as a model of arterial flow and pulse transmission," *Phys. Med. Biol.*, vol. 2, pp. 178–187, 1957.

[90] M. Taylor, "The input impedance of an assembly of randomly branching elastic tubes," *Biophysical J.*, vol. 6, pp. 29–51, 1966.

[91] P. Larose and J. Grotberg, "Flutter and long-wave instabilities in compliant channels conveying developing flows," *J. Fluid Mech.*, vol. 331, pp. 37–58, 1997.

[92] H. Atabek and H. Lew, "Wave propagation through a viscous incompressible fluid contained in an initially stressed elastic tube," *Biophysical J.*, vol. 6, pp. 481–503, 1966.

[93] R. Prud'homme, T. Chapman, and J. Bowen, "Laminar compressible flow in a tube," *Appl. Sci. Res.*, vol. 43, pp. 67–74, 1986.

[94] H. van den Berg, C. Seldam, and P. Gulik, "Compressible laminar flow in a capillary," *J. Fluid Mech.*, vol. 246, pp. 1–20, 1993.

[95] E. Arkilic, M. Schmidt, and K. Breuer, "Gaseous slip flow in long microchannels," *J. Microelectromechanical Systems*, vol. 6, pp. 167–178, 1997.

[96] J. Harley, Y. Huang, H. Bau, and J. Zemel, "Gas flow in micro-channels," *J. Fluid Mech.*, vol. 284, pp. 257–274, 1995.

[97] I. Papautsky, J. razzle, T. Ameel, and A. Frazier, "Microchannel fluid behavior using micropolar fluid theory," in *Proc. of MEMS'98*, (Heidelberg), pp. 544–549, 1998.

[98] L. Landau and E. Lifschitz, *Lehrbuch der Theroetischen Physik*, vol. VI (Hydrodynamik). Berlin: Akademie-Verlag, 1971.

[99] R. Gupta, S. Kim, and L. Pileggi, "Domain characterization of transmission line models and analyses," *IEEE Trans. Computer-Aided Design*, vol. 15, pp. 184–193, 1996.

[100] P. Voigt and G. Wachutka, "Electro-fluidic microsystem modeling based on Kirchhoffian Network theory," in *Dig. of Tech. Papers of Transducers'97*, (Chicago), pp. 1019–1022, June 16–19, 1997.

[101] K. Fluri, E. Verpoorte, and N. de Rooij, "Micro-fluidic chips for heterogeneous assays in clinical diagnostics," in *Proc. of Transucers'99*, (Sendai, Japan), pp. 1338–1339, 1999.

[102] B. van de Schoot, S. Jeanneret, A. van den Berg, and N. de Rooij, "A silicon integrated miniature chemical analysis system," *Sensors and Actuators*, vol. B 6, pp. 57–60, 1992.

[103] D. Binz, S. Keeping, and A. Vogel, " 'Lab on a chip' for multi parameter water analysis," in *Proc. of Transucers'99*, (Sendai, Japan), pp. 684–687, 1999.

[104] S. Shoji, S. Nakagawa, and M. Esashi, "Micropump and sample-injector for integrated chemical analyzing systems," *Sensors and Actuators*, vol. A21-A23, pp. 189–192, 1990.

[105] T. Lammerink, M. Elwenspoek, and J. Fluitman, "Integrated micro-liquid dosing systems," in *IEEE Microelectromech. Systems Workshop*, (Fort Lauerdale, FL), pp. 254–259, Feb. 7-10, 1993.

[106] H. van Lintel, F. van de Pol, and S. Bowstra, "A piezoelectric micropump based on micromachining of silicon," *Sensors and Actuators*, vol. 15, pp. 153–167, 1988.

[107] F. van de Pol, H. van Lintel, M. Elwenspoek, and J. Fluitman, "A thermopneumatic micropump based on micro-engineering techniques," *Sensors and Actuators*, vol. A21-A23, pp. 198–202, 1990.

[108] M. Richter, *Benutzerhandbuch zu PUSI*. Fraunhofer-Institut für Festkörpertechnologie, München, 1994.

[109] P. Voigt, G. Schrag, and G. Wachutka, "Micropump macromodel for standard circuit simulators using HDL-A," in *Proc. of the 10th European Conf. on Solid-State Transducers (EuroSensors X)* (R. Puers, ed.), (Leuven), pp. 1361–1364, Timshel BVBA, Leuven, 1996.

[110] P. Voigt, G. Schrag, and G. Wachutka, "Methods for model generation and parameter extraction for MEMS," in *Simulation of Semiconductor Processes and Devices 1998*, (Leuven), pp. 149–152, Sept. 02–04, 1998.

[111] O. Degani, D. Seter, E. Socher, S. Kaldor, and Y. Nemirovsky, "Optimal design and noise consideration of micromachined vibrating rate gyroscope with modulated integrative differential optical sensing," *J. of Microelectromechanical Systems*, vol. 7, pp. 329–338, 1998.

[112] M.-S. Kang, S.-K. Youn, Y.-H. Cho, and K. Lee, "Dynamic modeling of a tunable microgyroscope," *Sensors and Materials*, vol. 10, pp. 413–424, 1998.

[113] P. Voigt, R. Sattler, P. Sasse, S. Hoffmann, R. Noé, and G. Wachutka, "Parameterextraktion für Mikrosysteme am Beispiel eines Gyroskopes," in *Mikrosystemtechnik'99*, (Chemnitz), pp. 156–159, Oct. 12–13, 1999.

[114] X. Zhang and W. Tang, "Viscous air damping in laterally driven microresonators," *Sensors and Materials*, vol. 7, pp. 4–15, 1995.

[115] A. Beskok and G. Kardianakis, "Simulation of slip-flows in complex microgeometries," *ASME, DSC*, vol. 40, pp. 355–370, 1999.

[116] D. Greywall, P. Busch, and J. Walker, "Phenomenological model for gas-damping of micromechanical structures," *Sensors and Actuators*, vol. 72, pp. 49–70, 1992.

[117] L. Lin, R. Howe, and A. Pisano, "Microelectromechanical filters for signal processing," *J. of Microelectromechanical Systems*, vol. 7, pp. 286–294, 1998.

[118] R. Howe, W. Yun, and P. Gray, "Surface micromachined, digitally force-balanced accelerometer with integrated CMOS detection circuitry," in *Dig. IEEE Solid-State Sensor and Actuator Workshop*, pp. 126–131, 1992.

[119] K. Ikeda, H. Kuwayama, T. Kobayashi, T. Watanabe, T. Nishikawa, T. Yoshida, and K. Harada, "Silicon pressure sensor integrates resonant strain gauge on diaphragm," *Sensors & Actuators*, vol. A21-A23, pp. 146–150, 1990.

[120] T. Veijola, H. Kuisma, and J. Ladenperä, "Dynamic modeling and simulation of microelectromechanical devices with a circuit simulation program," in *Book of Abstracts of MSM'98*, (Santa Clara, CA), pp. 245–250, April 06–08, 1998.